DISSERTATION

SUBMITTED TO THE
COMBINED FACULTIES OF THE NATURAL SCIENCES AND MATHEMATICS
OF THE RUPERTO-CAROLA-UNIVERSITY OF HEIDELBERG, GERMANY
FOR THE DEGREE OF

DOCTOR OF NATURAL SCIENCES

PUT FORWARD BY

MARC-ANDRÉ BESEL, M.SC.
BORN IN: DARMSTADT, GERMANY

ORAL EXAMINATION: JULY 23rd, 2012

SUPERNOVA LIGHT ECHOES AS A PROBE TO SUPERNOVA PHYSICS AND THE INTERSTELLAR MEDIUM

REFEREES: PROF. DR. THOMAS HENNING
PROF. DR. JOACHIM KRAUTTER

”We shall not cease from exploration
…

Zusammenfassung

Lichtechos von Supernova Explosionen sind ein spektakuläres und nützliches Phänomen in der Astronomie. Das reflektierte Licht enthält die spektrale Signatur der Explosion und erlaubt eine präzise Charakterisierung der Supernova, auch mehrere hundert Jahre nach dem eigentlichen Ereignis. Weiterhin enthalten Lichtechos Informationen über die Eigenschaften des reflektierenden und emittierenden Staubes. Dies erlaubt detaillierte Studien über das ungestörte interstellare Medium. Diese Arbeit konzentriert sich auf drei Teilaspekte von Supernova Explosionen, ihrer Echos und des interstellaren Mediums.

Im ersten Teil dieser Arbeit gehe ich auf Studien im optischen und infraroten Frequenzbereich ein. Während die Suche nach optischen Lichtechos von Kepler's Supernova bislang keine eindeutigen Ergebnisse brachte, wurde in dieser Arbeit eine neue Methode zur systematischen Suche nach Infrarot-Echos anhand von *WISE* Daten entwickelt. Mit diesem Verfahren konnten Lichtecho Kandidaten mehrerer historischer Supernovaüberreste gefunden werden.

Zudem konnten die Gebiete in denen ein Echo hervorgerufen wird, mit den Orten größter Dichte des kalten neutralen Mediums assoziiert werden. Vergleiche der Beobachtungen mit theoretischen Studien enthüllen die fraktale Struktur des interstellaren Mediums und seiner zugrundeliegenden turbulenten Flüsse.

Weiterhin konzentriere ich mich auf eine Untersuchung des Staubgehaltes von Cassiopeia A. Mit Hilfe von Ferninfrarot Daten kann eine ungestörte Staubkomponente innerhalb der rückwärtig gerichteten Schockwelle der Supernova ausgemacht werden. Diese Beobachtungen zeigen, dass Typ IIb Supernovae zwar anfangs Staub produzieren, aber auch einen effektiven Mechanismus zur anschließenden Staubzerstörung besitzen.

Abstract

Echoes of supernova explosions are a spectacular and valuable phenomenon in astronomy. The reflected light contains spectral information from the explosion and allows precise characterization of the supernova, even if it already happened several hundred years ago. The echo also contains information about the reflecting and emitting dust, enabling detailed studies on the physics of pristine interstellar material. This work focuses on three topics within this framework of supernova explosions, their light echoes and the interstellar medium.

First, I use optical and infrared surveys to identify echoes from supernovae. While the search for scattered light echoes from Kepler's supernova proved unsuccessful until now, I developed a new approach to systematically search for infrared echoes using *WISE* data. This new technique allows the identification of light echo candidates from several historical supernova remnants.

The echoing material could be associated with the densest parts of the cold neutral medium. A comparisons with theoretical studies reveals the fractal structure of the interstellar medium and its underlying turbulent flows.

Finally, I concentrate on the dust content of Cassiopeia A. With the aid of new far infrared data, an unshocked dust component is identified within the reverse shock region of the remnant. These observations confirm that Type IIb supernovae initially produce dust, but directly show their mechanism and efficiency of dust destruction.

Contents

1 Introduction

1.1 The Interstellar Medium

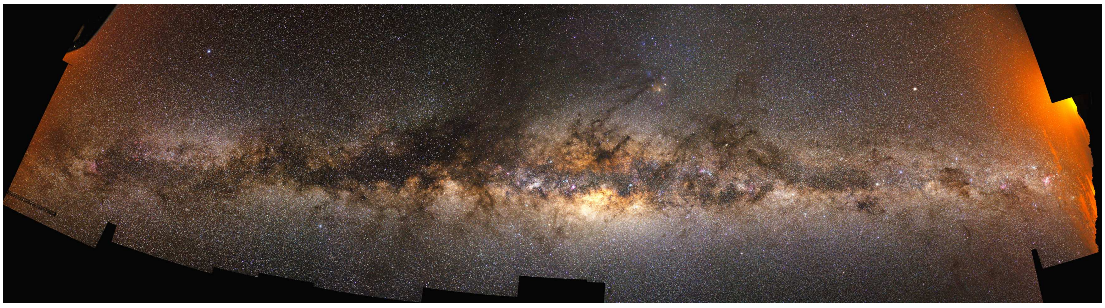

Figure 1.1: Dark clouds and emission nebulae across the Galactic plane towards the center of the Milky Way.

Before the 18th century the Universe was thought to consist of stars and vacuum. Then, Charles Messier, Sir F. William Herschel and others recognized numerous nebulous objects and dark clouds across the sky. It has not been clear whether these constituents are patches of gas, fluids or unresolved stars, but they were generally seen as isolated objects in otherwise empty space. In 1847, Struve noted that the apparent density of stars declined with distance and proposed a uniform absorbing medium in between. He derived an extinction coefficient of 1 mag/kpc, which is remarkably close to the modern estimate of 0.7-1 mag/kpc (depending on the line of sight).

With the advent of spectroscopy Huggins and Miller (1864) were able to identify emission from gaseous lines in these nebulae across the sky and Hartmann (1904) and Plaskett and Pearce (1933) noted narrow Ca II absorption lines towards spectroscopic binary stars, which increased in strength with larger distance to the stars. From these observations they inferred an interstellar origin of the absorbing medium, as well as the Galactic rotation from the sine-wave-patterned Doppler shift of the lines with respect to the Galactic longitude.

In 1930 Trumpler found further evidence for extinction of starlight from studies of star clusters and also noted a systematic reddening of stars near the Galactic plane. He implied a general homogeneous layer of dust particles of various sizes in the Milky Way and the presence of free atoms with a space density of about one hydrogen atom per cubic centimeter.

By the late 1930's the presence of a uniform and widely distributed layer of gas and dust was broadly accepted as a true **interstellar medium (ISM)**.

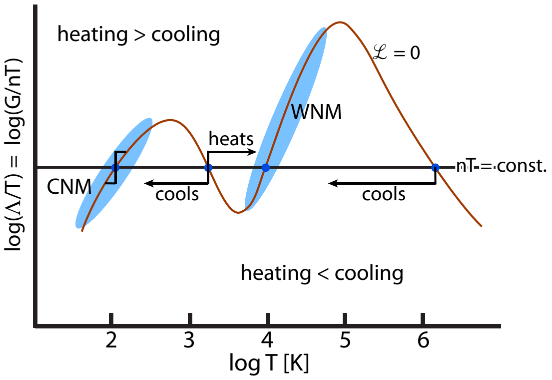

Figure 1.2: The cold neutral medium (CNM) and the warm neutral medium (WNM) are the stable equilibria in the two-phase model by Field, Goldsmith, and Habing (1969).

The idea of a uniform ISM had to be abandoned upon high-resolution spectroscopic observations in the 1940's. Absorption lines split up into many narrow line components at slightly different Doppler shifts due to different distances of the absorbing clouds, implying a clumpy ISM with a radial gradient in the galactic disk, which is organized into clouds (Stebbins et al. 1940).

A major constituent of bright emission nebulae is ionized hydrogen (H^+), which is for example traced by observations of the Hα-recombination line. Strong localizations of H^+ include the diffuse nebulae already described by Herschel, which include star-forming regions, planetary nebulae and supernova remnants. In these regions the gas is photoionized by UV photons ($h\nu \geq 13.6\,\mathrm{eV}$). Over 90% of H^+, however, is located outside of these confined regions. It is found at low-surface brightnesses throughout the ISM.

In contrast to H^+, atomic hydrogen was not directly observed until 1951, when the extremely rare hyperfine transition in the atomic ground state at 21 cm was first detected by Ewen and Purcell. Emission from cold neutral hydrogen was found to pervade the entire Milky Way disk. Due to the long wavelength, this line is practically not subject to extinction and a mapping of the entire Galactic disk was possible for the first time. By mass, this component makes up a large fraction of the entire ISM.

In an attempt to physically describe the observed properties of the ISM, Field, Goldsmith, and Habing (1969) (FGH) developed their famous two-phase model. In a state of local thermal pressure equilibrium, two gaseous phases could coexist in the general ISM:

- a cold ($\mathrm{T} \leq 300\,\mathrm{K}$) and dense ($\mathrm{n} \geq 10^2\,\mathrm{cm}^{-3}$) phase, consisting of neutral and molecular gas (Cold Neutral Medium, CNM) and
- a warm ($\mathrm{T} \sim 10^4\,\mathrm{K}$) and sparse ($\mathrm{n} \leq 10^1\,\mathrm{cm}^{-3}$) phase, consisting of neutral and ionized gas (Warm Neutral Medium, WNM).

In thermal equilibrium, the cooling rate $n^2\Lambda(T)$ and heating rate nG should balance each other

$$\mathcal{L} = n^2\Lambda(T) - nG = 0, \tag{1.1}$$

and for perturbations $\partial\mathcal{L}/\partial T$ at constant pressure or density, the medium would segregate naturally into the two stable phases.

As the equilibria depend on the heating and cooling mechanisms, they are of special interest in ISM studies. The most important cooling mechanisms are various recombination emission lines, thermal Bremsstrahlung, molecular cooling and emission from dust grains (thermal and non-thermal). Interstellar heating processes include cosmic-ray heating, photoionization and photo-electrons from dust grains.

The original FGH-model was later extended by McKee and Ostriker (1977) to include a third, hot phase produced by supernova explosions (Hot Intercloud Medium, HIM), which has been inferred by observations of very low density ($n \leq 10^{-2}\,\mathrm{cm}^{-3}$) and hot ($T \sim 10^{6}\,\mathrm{K}$) shells and bubbles from H^{+} observations.

Today, the phase models still provide a good explanation of the general ISM understanding (for a summary of phases in current models see Table 1.1), but much stronger underlying dynamic effects governs active research.

The most tantalizing views of the ISM came along, when the Infrared Astronomical Satellite (IRAS) observed ”interstellar cirrus at high galactic latitudes” in 1983. They did not look like what was expect in a mostly static medium, but revealed a very complex, filamentary, criss-crossed and interwoven structure. These observations called for new and refined models including turbulence to stabilize gas in the classically ”unstable” regime.

Active research fields in ISM studies today cover:

- How does turbulence effect the morphology of the ISM?
- What drives interstellar turbulence?
- Formation and evolution of molecular clouds
- Onset of star formation within molecular clouds
- Influence of magnetic fields
- Dust and molecule formation and evolution in the ISM

Generally, the ISM is understood as a violent place of taking and giving from stars throughout their evolution. Stars form out of the densest parts of molecular clouds and replenish the ISM with various metals and dust throughout their evolution. The explosions of high mass stars eventually cycles back kinetic energy into the ISM by large scale shocks. These shocks stir and mix the ISM and sweep up significant amounts of gas, which again can collapse and form a new generation of stars.

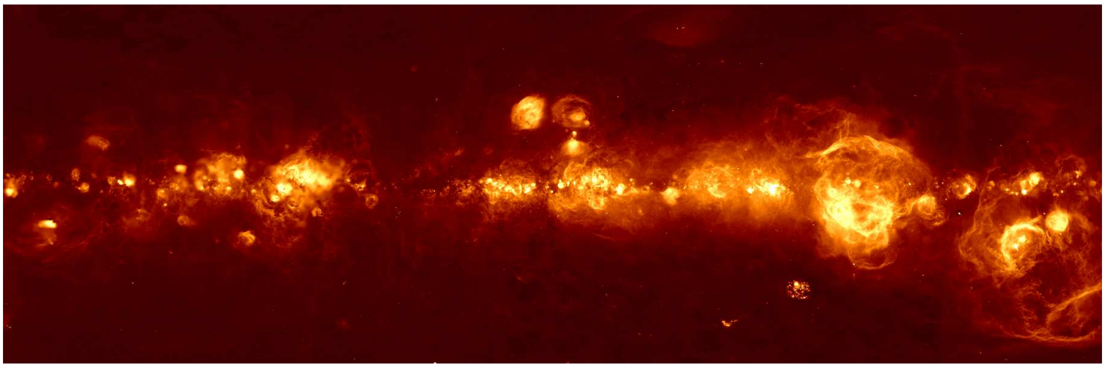

Figure 1.3: Bubbles and shells in the ionized ISM. Image by the Wisconsin H-Alpha Mapper (Reynolds et al. 1998)

Table 1.1: Overview of the ISM phases

Component	density	Temperature	Filling Factor		tracers
	[cm^{-3}]	[K]	Volume [%]	Mass [%]	
Cold Medium					
Neutral (CNM)	50	80 – 100	1 – 4	35	absorption lines
Molecular Clouds	> 1000	10 – 20	< 1	22	molecular lines
Warm Medium					
Neutral (WNM)	0.5	8000	20 – 30	30	21 cm emission
Ionized (WIM)	0.1	10^4	20 – 50	11	Hα
H II Regions	$10^2 - 10^5$	10^4	< 1	0.5	Hα
Hot Medium					
Ionized (HIM)	0.003	10^6	30 – 70	2.3	X-ray and O IV absorption

1.2 Dust in the Universe

Although not really appreciated by many inhabitants on Earth, dust – or very small solid particles – plays an important role throughout the Universe. Dust makes out about 1% of the total mass of the ISM, but is responsible for nearly half of the entire bolometric luminosity of the Galaxy, as it absorbs and reradiates about 30–50% of the starlight.

Next to being an important heating and cooling agent due to its interaction with starlight, dust plays a fundamental role in the chemistry of the Universe, the formation of planetary systems and ultimately the genesis of life. Dust grains provide a surface where atoms can accrete, meet and react to molecules. Such catalytic processes are the only viable mechanisms to form H_2 (Gould and Salpeter 1963), as the simplest interstellar molecule.

Extinction

In visible light, dust is most prominent from the dimming and reddening of starlight and was already noted by Trumpler in 1930. He noted a wavelength dependent extinction (absorption and scattering) towards stars, and implied that dust particles of a variety of sizes are responsible for it. The average interstellar extinction curve is shown in Figure 1.4. Still today it remains the main source of information about dust. Apart from the general trend that radiation at longer wavelength is less absorbed than at shorter ones, its most prominent feature is a bump peaking in the UV-wavelength regime. Its origin is not well understood, but is believed to be attributed to some high-abundance elements, as C, Mg, Si or Fe (Draine 1989). Newer studies imply this feature to be produced by polycyclic aromatic hydrocarbons (PAH), which are ubiquitous in the ISM (e.g. Draine and Li 2007). PAHs are large carbon based molecules, which have strong emission features in the near- and mid-infrared regime. Other characteristics of the extinction curve include an absorption feature from silicates near 10 µm and more

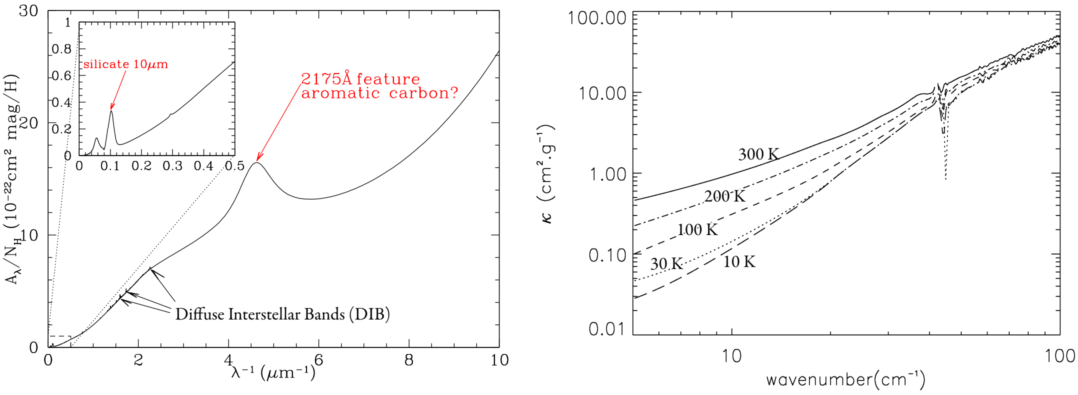

Figure 1.4: *left*: Average interstellar extinction curve for diffuse interstellar clouds from Draine (2009). *right*: Opacity for $MgSiO_3$ dust, experimentally synthesized at different temperatures by Jäger et al. (2009a).

than 400 diffuse interstellar bands (DIB, Hobbs et al. 2009). Despite their ubiquity, non of these features has been exactly identified today, although it is suggested that they originate from electronic transitions of PAH's (Draine and Li 2007).

Dust Models

Dust composition models should be able to reproduce the interstellar extinction curve, and some of the very early theoretical models (e.g. Draine and Lee 1984; Li and Draine 2001; Mathis et al. 1977) are still in use today. They imply a huge range of spherical grain sizes from a = 0.005 µm (small UV absorbing grains) to a = 1 µm (large "thermal" grains), with a distribution of $n(a) \propto a^{-3.5}$ to explain the observed extinction curve. Silicates and carbonaceous materials seem to dominate the grain mix, but the models must also attribute the observed fraction of elements *not* in the gas phase (depletion).

While exact laboratory measurements of emission lines from gases are very advanced today, the experimental characterization of emission from dust is ambiguous. One always has to keep in mind that abundances and physical conditions of the dust environments can change by observing direction and that these abundances can not be determined with high accuracy. Laboratory conditions and materials are also not able to exactly reproduce astrophysical conditions for the presence of dust grains or their formation processes (the best laboratory vacua, $\sim 10^{-12}$ mbar, just reach the highest densities in interstellar clouds $\sim 10^4\,\mathrm{cm}^{-3}$). With these limitations in mind, one should always treat the physical implications of a dust model based calculation as an approximation to a factor of a few.

Recent dust properties derived from laboratory measurements contain a number of different astrophysical environments, with an emphasis on conditions for star and planet formation (e.g. Ossenkopf and Henning 1994), and the general ISM (e.g. Dorschner et al. 1995a). The most noted theoretical models include the work of Draine and Li (2007) or Zubko et al. (2004).

Emission from Dust

As dust absorbs photons at visible wavelength (and herewith heats itself), it radiates in the infrared as a result of the increase of its thermal energy.

In the state of thermal equilibrium, dust grains would re-radiate the incoming emission (modified by some absorption cross section) like a black-body at the equilibrium temperature. The grain absorption cross-section (also called dust opacity) is determined by the underlying dust composition and must be derived from theoretical considerations or the above mentioned laboratory measurements.

Generally the thermal emission from grains in the far infrared / sub-mm is proportional to the total dust mass and thus, it is possible to derive physical dust masses M_{dust} of interstellar clouds

$$M_{\text{dust}} = F_\nu D^2 / \kappa_\nu B_\nu(T_{\text{dust}}), \tag{1.2}$$

where F_ν is the received infrared radiation, D the distance to the grains, T_{dust} the dust temperature, B the Planck-function and κ the dust opacity (Hildebrand 1983). Under the assumption of a constant abundance ratio between dust and gas (commonly in the range 1:120 as inferred by Li and Draine 2001), it is also possible to constrain mass properties of the gas phase.

Formation, Evolution and Destruction

Observations of late type stars and planetary nebulae suggest that dust is formed efficiently in the cool outflows of these evolved stars. At certain threshold temperatures, the solid grains can condense out from the gaseous phase and build seeds for consecutive grain growth. In fact, nearly all heavy elements ejected by these stars deplete on grains.

The dust production efficiency of supernovae is very controversial, and will be discussed in chapter 4. While some authors (Dunne et al. 2003; Sugerman et al. 2006) claim to detect massive "dust factories", others contradict these views (Barlow et al. 2010; Krause et al. 2004). At least in todays Universe, the role of supernovae in dust evolution is rather bounded to dust destruction than formation. When strong supernova shocks plow through the ISM and overrun dust grains they are subject to sputtering and can loose much of their material. On a global perspective dust grains only survive about 4×10^8 yr until they are altered or destroyed by shocks throughout the ISM (Draine 2009). In contrast to their destruction time, their depletion time, or the time for grain growth on existing seeds is only 10^5 yr within the cold neutral medium. Thus, the fraction of pristine stellar grains should be low (10–20%) in the ISM. This is supported by the fact that presolar grains, extracted from meteroids, only show small fractions of stellar grains (e.g. Hoppe and Zinner 2000).

Many more details on the interstellar medium and dust in the Universe are presented in the textbooks by Tielens (2005) and Whittet (2003) as well as the reviews by Draine (2009) and Draine (2003), which were used as a source of information here.

1.3 Stellar Evolution in a Nutshell

As the beginning and the final state of stellar evolution are of some relevance to this work, I will very briefly give a description here. I refer the more interested reader to the books by Kippenhahn and Weigert (1994) and Carroll and Ostlie (2006).

Star Formation

In current understanding, star formation takes place in a mode called ”gravoturbulent fragmentation” (Klessen et al. 2000). In this scenario, dense molecular clouds form from converging turbulent flows and can build local density enhancements. When a critical Jeans mass is reached in such a core (density $n_H = 10^4 - 10^5\,\mathrm{cm}^{-3}$, size-scale $d = 0.03 - 0.2\,\mathrm{pc}$) it is subject to self-gravitation and will collapse to build a protostar. If the center of the protostar gets hot enough, nuclear fusion can start and a star is born.

Stars are build in a distribution of masses, which will effect their later evolution as low-and intermediate mass stars (0.8–8 $\mathrm{M}_\odot$) or high-mass stars ($> 8\,\mathrm{M}_\odot$). The distribution seems to follow a universal initial mass function (IMF) (Kroupa 2002) and it is one of the important benchmarks of star-formation theories to produce this trend.

Fate of Low- and Intermediate Mass Stars

Stars with masses $< 8\,\mathrm{M}_\odot$ make up the largest fraction of stars by number (about 97%) and have a long dynamical lifetime of $> 10^9$ years. Their main evolution ends as they can not start fusion of carbon and will loose their stellar envelopes by cool winds and the final ejection of a planetary nebula to leave a degenerated white dwarf.

If the white dwarf is part of a binary star system, it may accrete material from its companion, and reach a certain mass limit (Chandrasekhar, 1.38 $\mathrm{M}_\odot$) at which it instantly starts an explosive fusion of carbon and disrupts the entire star in just a few seconds. Such an event is called a supernova of Type Ia. As the explosion always happens at a defined mass, its energy output defines a ”standard candle” and has been used to determine the distances to Galaxies. Subtypes of Type Ia explosions with slightly different scenarios are known, but shall not be subject to this introduction.

Fate of High Mass Stars

High mass stars have much shorter life-times ($\sim 10^6$ years) and intrinsically have enough material to support the fusion of carbon and higher mass elements until the inner core of the star consists of non-fusing nickel-and-iron and reaches the Chandrasekhar mass limit. At this point the core will collapse, while protons and electrons recombine and produce a neutron star and neutrino outburst. The core-collapse takes place at significant speeds (up to $^1/_3$ speed of light) and produces a shock wave, which eventually disrupts the star and expels its outer envelopes to build a supernova remnant. Upon the collision of the blast wave with surrounding circumstellar and interstellar medium, a reverse shock falls back into the ejecta and heats them up.

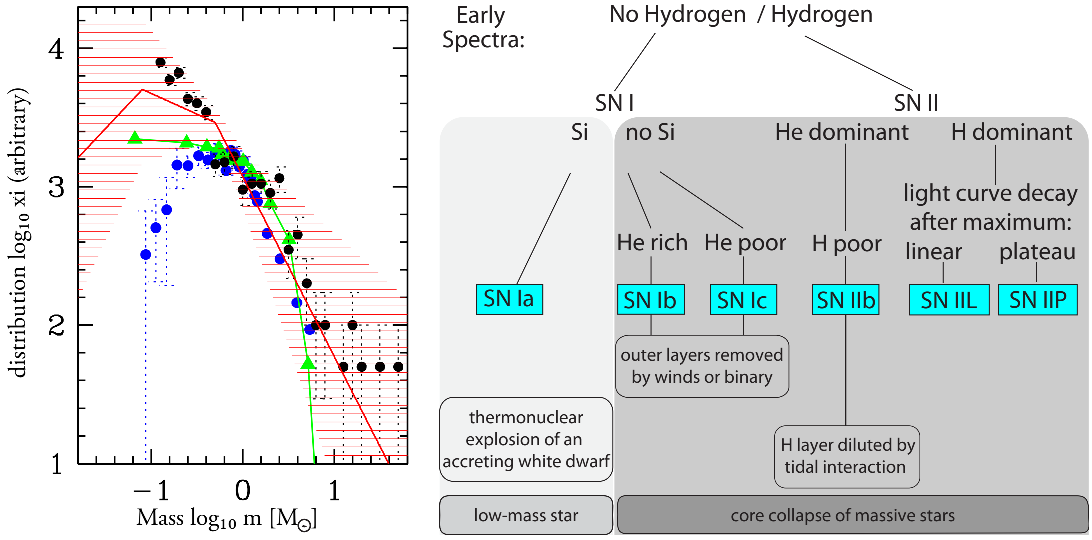

Figure 1.5: *Left*: Distribution of stellar masses produced in a star formation event within a certain volume of space - initial mass function (IMF). This distribution is similar for a variety of regions, e.g. Orion (*black*), Plejades (*green*) and M35 (*blue*). Figure from Kroupa (2002). *Right*: Supernovae classification scheme based on the early spectral properties of the explosion. The supernova types are framed in cyan. Figure based on M. Montes.

Core-collapse explosions differ by their progenitor mass and metallicity and are often classified by the abundance of their spectral lines and light curves. A schematic of the different explosion types is shown in Figure 1.5. Depending on their initial mass and the explosion type, the remnants can harbor a neutron star or even a black hole.

With the propagation of the shock-wave into space, supernovae enrich the surrounding medium with heavy elements and provide kinetic energy as a source for turbulent flows. As suggested by the above mentioned gravoturbulent fragmentation theory, such flows trigger new phases of star formations, and therefore supernovae have an important dynamic role in the Galactic environment.

1.4 Light Echoes of Radiation Events

When the expanding sphere of light from an intense radiation outburst, like a supernova, propagates into space and illuminates the intervening structures of the circum- or interstellar medium, it can give rise to a phenomenon called light echo: The flash of light is scattered by dust grains, producing a reflection nebula, which appears to move across the sky. Since absorption of light takes place in addition to scattering, the scattered-light echo is accompanied by an infrared echo of thermal re-emission from the heated dust grains (Dwek 1985). As the light path of the echo is longer than the direct connection between the radiation origin and an observer on Earth, the echo can be seen with a significant time delay, with respect to the initial light burst by the observer. Such a phenomenon enables studies of both the emitting event and the reflecting material.

Light Echo Geometry

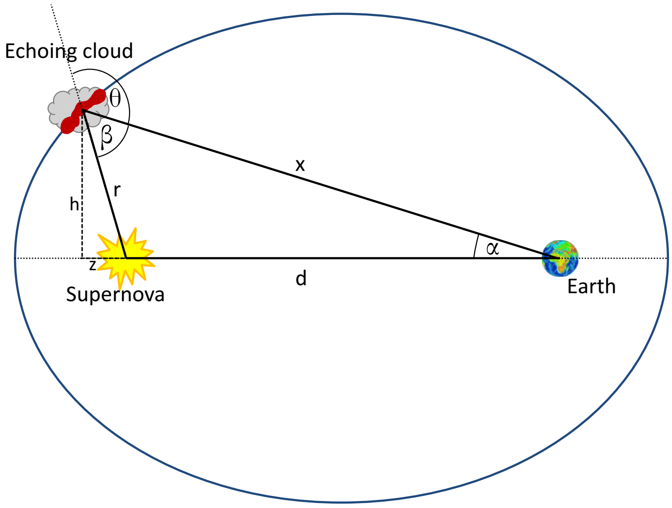

Figure 1.6: Geometrical sketch of the light echo geometry. The radiation burst origin and an observer on Earth are located in the foci of an ellipsoid. All points on this ellipsoid describe locations with equal delay time t, which corresponds to the time difference between the original SN outburst observation and the current observing epoch. Material situated on any point of the ellipsoid can be seen simultaneously as an echoing structure.

The position of visible echoing dust clouds is confined by the light echo geometry as sketched in Figure 1.6. At any given time, these clouds are located on an ellipsoid with the supernova and Earth in its two foci. As light from the echoing cloud has to travel a longer distance ct compared to the direct light path d from the supernova explosion, an observer on Earth will see the induced light echo with a certain delay time t after the initial light sphere passed Earth.

The traveled distances equal

$$r + x = d + ct \tag{1.3}$$

Using the law of cosines $r^2 = x^2 + d^2 - 2xd\cos\alpha$, with the angle α under which an echo appears on the sky with respect to the outburst origin, the distances x, r and the scattering angle θ can be expressed as

$$x = \frac{(ct)^2 + 2ctd}{2(c\Delta t + d(1-\cos\alpha))} \tag{1.4}$$

$$r = ct + d - \frac{(ct)^2 + 2ctd}{2(ct + d(1-\cos\alpha))} \tag{1.5}$$

$$\theta = 180^\circ - \arccos\left(\frac{x^2 + r^2 - d^2}{2rx}\right). \tag{1.6}$$

Similarly the line of sight distances z and h can be computed as

$$z = d - x \cos \alpha \tag{1.7}$$

$$h = x \sin \alpha . \tag{1.8}$$

Hence their 3-dimensional location on the sky can be unambiguously determined if the distance to the illuminating source and the epoch of its outburst is known, making light echoes a powerful tomographic probe.

Historical Remarks

Light echoes of intense radiation events have long been proposed since Jan Oort (Zwicky 1940) and later on theoretically described (Chevalier 1986; Sugerman 2007; van den Bergh 1965).

The first galactic observations of light echoes can probably be dated back to 1901 when Wolf noted morphologically variable and fast (near to the speed of light) expanding knots around Nova Persei. The first extragalactic echoes were perceived by the IR excess of supernovae (for example SN1979c; see Bode and Evans 1980 and Dwek 1983). Later on, scattered light echoes around SN1993J have been directly imaged by the Hubble Space Telescope in the galaxy M81 (Liu et al. 2003).

But only recently, after the discovery of infrared light echoes around Cas A in 2005 by Krause et al., and the discovery of scattered light echoes from the SNR Cas A and Tycho by Rest et al. (2008), the full potential for Galactic astronomy has been recognized.

Light Echoes as a Probe to Supernova Explosions

Using the positional information from *Spitzer* mid-infrared images of infrared echoes, Krause et al. (2008a) found the scattered light counterpart from an echo and were able to extract an optical spectrum of the supernova event. With this spectrum they were able to directly classify the supernova more than 330 years after the initial light flash swept past Earth. The spectrum showed typical features of a core-collapse Type IIb supernova (see Figure 1.7). Using the same technique, Krause et al. (2008b) classified Tycho Brahe's supernova as of Type Ia.

Thus, light echoes enable a postum spectral classification of nearby supernovae and provide an important link between the observed light curves of distant supernovae and the properties of late-type evolutionary phases as a supernova remnant.

More recently Rest et al. (2011) discovered differences in the light echo spectra of Cas A under different scattering positions, which probe different regions of the SN photosphere. Specifically, they inferred higher velocities in one of their observing sightlines. This observation reveals that the explosion mechanism is not isotropic, but rather asymmetric.

Light Echoes as a Probe to the Interstellar Medium

As the light echo geometry unambiguously determines the three dimensional positions of the echoing cloud structures, continued imaging of light echoes provides a unique

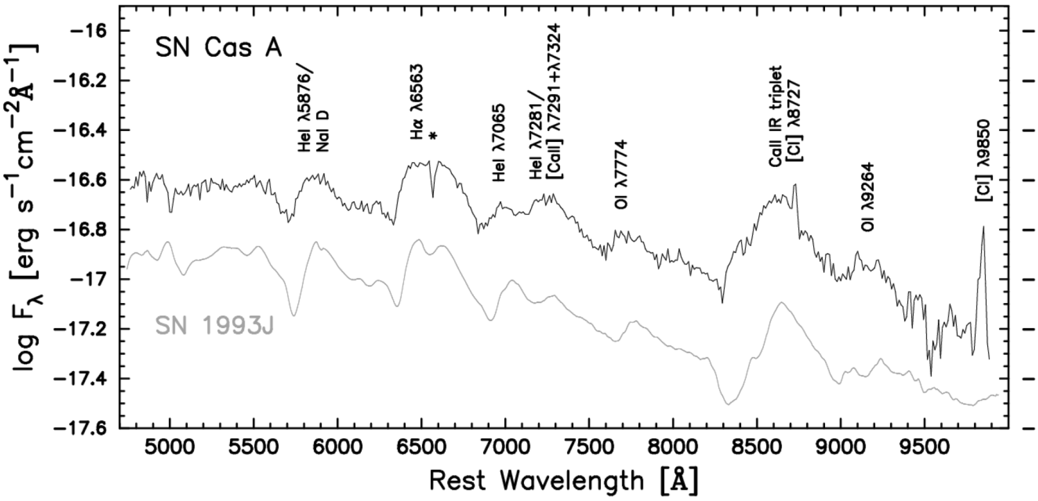

Figure 1.7: Recorded light echo spectrum from Cas A compared to the spectrum of the Type IIb supernova SN1993J. Figure from Krause et al. (2008a)

opportunity to map the true three-dimensional distribution of the circumstellar (if the echo is observed shortly after an outburst) or the interstellar medium (if the echo is observed long thereafter).

Observations of scattered light echoes in the circumstellar medium around SN1987A over more than 15 years revealed the bipolar outflow and equatorial density enhancement produced by the progenitor star (Sugerman et al. 2005).

Infrared echoes have been discovered across a 3° × 3° area on the sky by Hines et al. (2004) and Krause et al. (2005). Continued imaging over three years enabled the construction of tomographic maps of the surrounding interstellar medium, revealing its fractal three-dimensional structure (Kim et al. 2008).

In the second part of this thesis, I use infrared monitoring observations and the results of our detailed echo-emission simulation (Vogt et al. 2012) to further investigate the small and large scale morphologies of ISM structures responsible for infrared echoes.

Compared to the accuracy of kinematic distance estimates from radio observations, light echoes are the only method in astronomy which can provide direct high-resolution three-dimensional imaging over a large size span of circumstellar and interstellar structures.

1.5 Structure of this Thesis

This thesis concentrates on three topics within the framework of supernova explosions, their light echoes and the interstellar medium, which will be discussed in three parts.

The first part (Chapter 2) focuses on the search for light echoes around several historical supernova remnants in both optical and infrared surveys. The chapter is subdivided into three parts:

1. An optical survey around Kepler's supernova remnant.
2. An analysis of infrared echoes using *WISE* data and a new technique to identify these echoes.
3. Lists of identified light echoes candidates from the Crab nebula, Kepler, Tycho and SN1181.

In Chapter 3, I use observations of light echoes to probe the structure of the interstellar medium. A comparison of these observations with a numerical simulation of the ISM shows striking similarities on all scales revealing its underlying turbulent flows.

The last part (Chapter 4) presents a study of the dust content of the Cassiopeia A supernova remnant, which has been subject to serious debate for several years. Using high resolution far infrared observations with *Herschel*, several superposed dust components are disentangled to probe the dust production and destruction efficiency of this Type IIb supernova.

2 Search for Light Echoes around Historical Supernovae

The first part of my thesis focuses on the search for light echoes around several historical supernova remnants. Their spectroscopic classification still remains uncertain, as no direct spectra of their explosions could be taken at the time of their explosion. The reflection of the supernova light on clumps of interstellar material however, gives a second chance to secure its spectral signatures to gain further insides to its progenitor star and their explosion mechanisms, as well as to the physics of the interstellar medium. Identifying such echoes is the fundamental first step.

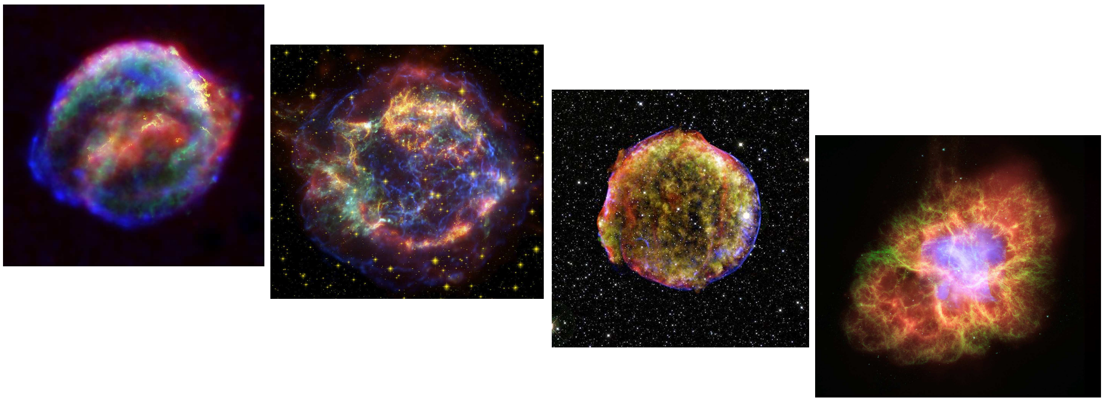

Figure 2.1: Historical supernova remnants Kepler, Cassiopeia A, Tycho and Crab (from left to right). Image copyrights: R. Sankrit and W. Blair, O. Krause, O. Krause, J. Hester

In the first section of this chapter I concentrate on the search for light echoes around ”Kepler’s” supernova, as the nature of its progenitor is still under serious debate while its initial observations marked the beginning of modern astronomy. The explosion was first sighted on October 9th 1604, when several astronomers awaited the close-by conjunction of Mars and Jupiter just 2° away from this ”new star” in the constellation Ophiuchus. Johannes Kepler dedicated his book *”De stella nova in pede Serpentarii”* to a detailed study of this object, including brightness and position comparisons to other stars. Although not aware that he actually witnessed a stellar death, the lack of an observable parallax and its ”sparkling” appearance led him to the conclusion that this "new" object was part of the sphere of fixed stars – a fact which conflicted with their view of the world with unchanging heavens.

The detailed reports by Kepler led modern day astronomer Baade (1943) to the conclusion of a supernova origin and inferred it as of Type Ia by its light curve. This view however, is questioned by observations of a nitrogen rich circumstellar environment by Bandiera (1987), who suggest a massive progenitor, like a Wolf-Rayet star with a consequent core-collapse supernova for Kepler. XMM-Newton abundance measurements of Si and Fe on the other hand are indicative of a Type Ia explosion of an intermediate mass star (Cassam-Chenaï et al. 2004).

Only with the help of light echoes it is possible to postum obtain spectra of such ancient supernovae and accurately determine their type. With the supernova type, the properties of the progenitor star are constraint and it is possible to associate the late type properties of supernova remnants with the exact explosion mechanisms, as a test and valuable input for theoretical supernova models.

During my studies I concentrated the search of light echoes towards several historic supernovae. For reference I list some basic properties of these objects in Table 2.1.

Table 2.1: Historical Supernova Remnants

Supernova	Explosion Date	RA	DEC	Dist. [kpc]	peak mag	Type	Ref
Cassiopeia A	16.Aug 168±19	$23^h23^m24^s$	$+58°48'54''$	$3.4^{+0.3}_{-0.1}$	6 (?)	IIb	a
Tycho	6.Nov 1572	$00^h25^m08^s$	$+64°09'56''$	$3.8^{+0.9}_{-0.3}$	-4	Ia	b
Kepler	9.Oct 1604	$17^h30^m36^s$	$-21°28'56''$	4 / 6	-2.25	? (Ia/II)	c
Crab	4.Jul 1054	$05^h34^m32^s$	$+22°00'52''$	2±0.5	-6 (?)	? (II?)	d
SN 1181	6.Aug 1181	$02^h05^m38^s$	$+64°49'42''$	?	-1	?	e
SNR G1.9+0.3	1870±30	$17^h48^m47^s$	$-27°10'16''$	7±0.5	not seen	? (Ia)	f

Notes – Entries denoted with an "?" show that this is not known or very controversial. The column "peak mag" lists the apparent visual peak magnitudes as observed by astronomers at the time of explosion. Column "Type" lists the suggested SN type. References for introduction and key results (including references therein): (a) Fesen et al. (2006); Krause et al. (2008a); Reed et al. (1995), see also chapter 4 (b) Krause et al. (2008b); Lu et al. (2011), (c) Baade (1943); Bandiera (1987); Cassam-Chenaï et al. (2004), (d) Hester (2008) and references therein, (e) Panagia and Weiler (1980), (f) Reynolds et al. (2008).

2.1 Search for Light Echoes around Keplers SNR

Using the Wide-Field-Imager at the 2.2 m ESO/MPG telescope on La Silla, Chile, a ~ 12.5 square-degree area around Kepler's supernova remnant was observed during two epochs. The variable emission from light echoes can be identified in the difference image between the two epochs. Although the method is very sensitive, as demonstrated on known light echoes around Tycho's supernova and on many detected asteroids, it was not possible to find any optical light echoes around Kepler's SNR. Further analysis of AKARI mid-infrared data also revealed no echoes.

2.1.1 Observational Strategy

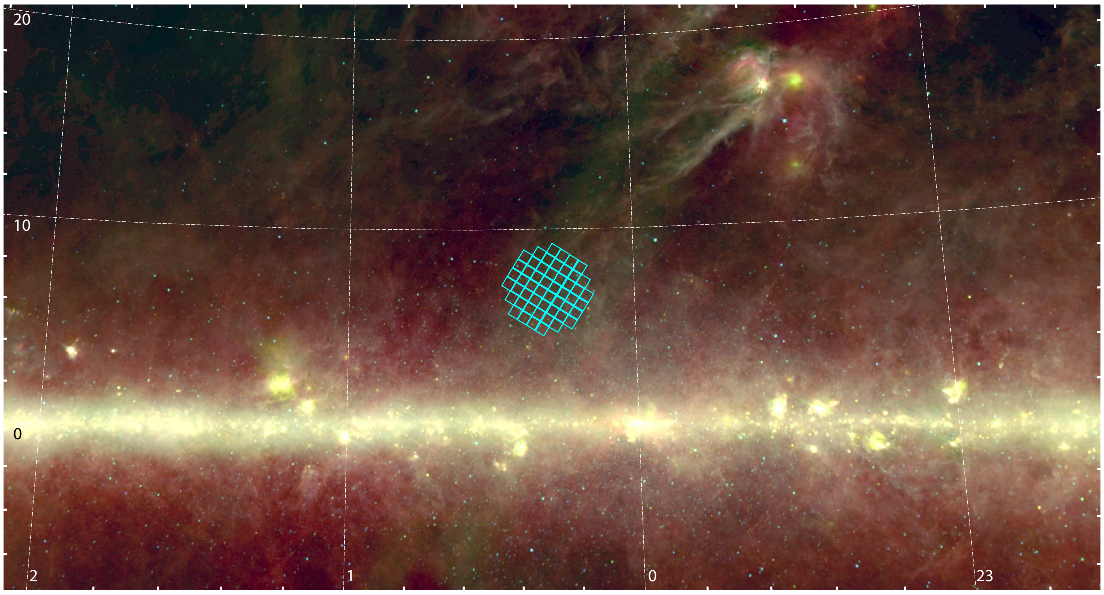

Figure 2.2: Footprint of the 52 analyzed WFI fields (cyan color) on an IRAS 12 µm (blue), 25 µm (green), 60 µm (red) color mosaic. Kepler's supernova remnant is located in the center of the mosaic, 6.5°above the galactic plane. Due to the close proximity to the Galactic center, the field is contaminated by a high density of field stars. The image is presented on a Galactic coordinate grid.

In order to find light echoes around Kepler's supernova, a circular area with a 4° diameter was observed in two epochs. This samples the entire light-speed-radius around Kepler. The light-speed-radius defines the area around the radiation burst source, were r (see Figure 1.6) equals the distance light can travel during the delay time (ct). The observed field equals to this area for the most commonly stated distance to Kepler ($d = 3.9\,\mathrm{kpc}$, Sankrit et al. 2005). If the recent distance estimation ($d = 6.5\,\mathrm{kpc}$) by Aharonian et al. (2008) is correct, the observed field would probe a larger illuminated area. Most light echoes around Cas A were found in this light-speed-radius area.

To cover this 12.5 square-degree field-of-view, 52 R-band mosaics with the Wide-Field-Imager (WFI, Baade et al. 1999) at the 2.2 m ESO/MPG telescope on La Silla, Chile, were acquired in June/July 2008 and June/August 2009. R-band images provide good image quality, as they do not suffer from interstellar extinction and usually feature better seeing than, for example, V-band images. As optical light echoes from Tycho and Kepler usually had surface brightnesses between 20.5 and 23.5 mag/arcsec^2, an exposure time of 25 min is required to reach a signal-to-noise ratio of at least ~ 5 for such sources.

Once two imaging epochs have been obtained, these images can be subtracted from each other to create a difference image. Such an image would be free of all stationary objects, like stars or galaxies, and would reveal all variable or moving sources with high contrast. Light echoes should be easily identified as diffuse sources, either appearing in the new epoch or nearby a diffuse structure from the earlier epoch.

Due to the proximity of Kepler's supernova remnant to the Galactic center, the field of view is expected to be very crowded by field stars. Therefore, it is essential to observe these fields at excellent seeing conditions to discriminate faint echo emission. In order to produce good difference images between two epochs, the seeing conditions should also be matched as well as possible. The atmospheric conditions were therefore a major decision factor during the second observing run, in which sequence the separate fields were observed. Remaining differences in the seeing conditions were than compensated by a special convolution described in section 2.1.3. A summary of the center positions of the observed fields and the achieved seeing conditions for the two observing runs is presented in Table 2.2.

After the second observing run, any evident echo candidates would immediately be observed with a spectrograph on an 8 m class telescope. The acquisition image of such an instrument would also ultimately verify the echo origin of any questionable echo candidate, before the multiple-hour spectroscopical integration.

2.1.2 WFI Observations

WFI utilizes a focal plane of eight $2\,\mathrm{k} \times 4\,\mathrm{k}$ CCD-chips to simultaneously observe a $33.6' \times 32.7'$ field (about the size of the full moon). It has a pixel-scale of $0.238''$/pixel, which optimally samples typical seeing conditions at La Silla. The average seeing during the 2008 observing run was $1.01''$, while in 2009 the conditions were a bit worse, with an average value of $1.1''$. The best observed seeing was $0.54''$ on July 5th 2008.

To optimally sample the gaps between adjacent CCD-chips and to achieve a uniform sky-background, a 5-point dither pattern, with an exposure time of 300 s each, was chosen. The combined total exposure time for both epochs was about 43.3 hours.

Table 2.2: Observed fields and seeing conditions

	Center Position		Epoch 1		Epoch 2	
Mosaic	RA	DEC	Date	Seeing	Date	Seeing
01	$17^{h}31^{m}42^{s}$	$-21^\circ11'55''$	11.06.2008	1.02	18.06.2009	1.55
02	$17^{h}29^{m}25^{s}$	$-21^\circ12'21''$	11.06.2008	1.14	15.06.2009	1.21
03	$17^{h}29^{m}24^{s}$	$-21^\circ44'21''$	11.06.2008	1.02	13.06.2009	1.13
04	$17^{h}31^{m}45^{s}$	$-21^\circ46'17''$	11.06.2008	0.93	13.08.2009	0.90
05	$17^{h}34^{m}00^{s}$	$-21^\circ44'16''$	11.06.2008	0.95	12.06.2009	1.05
06	$17^{h}33^{m}60^{s}$	$-21^\circ12'17''$	11.06.2008	1.07	12.06.2009	0.94
07	$17^{h}33^{m}58^{s}$	$-20^\circ40'02''$	12.06.2008	1.02	18.06.2009	1.19
08	$17^{h}31^{m}41^{s}$	$-20^\circ40'03''$	07.07.2008	1.04	18.06.2009	0.93
09	$17^{h}29^{m}27^{s}$	$-20^\circ39'56''$	07.07.2008	1.13	12.06.2009	1.06
10	$17^{h}27^{m}12^{s}$	$-20^\circ40'49''$	13.06.2008	0.79	18.06.2009	0.86
11	$17^{h}27^{m}06^{s}$	$-21^\circ12'02''$	13.06.2008	0.95	18.06.2009	0.99
12	$17^{h}27^{m}07^{s}$	$-21^\circ44'23''$	13.06.2008	1.26	20.08.2009	0.81
13	$17^{h}27^{m}07^{s}$	$-22^\circ16'19''$	25.06.2008	1.13	15.06.2009	1.10
14	$17^{h}29^{m}25^{s}$	$-22^\circ16'13''$	25.06.2008	1.09	15.06.2009	1.27
15	$17^{h}31^{m}42^{s}$	$-22^\circ16'07''$	25.06.2008	1.07	20.08.2009	0.91
16	$17^{h}34^{m}01^{s}$	$-22^\circ16'20''$	25.06.2008	1.21	15.06.2009	1.38
17	$17^{h}36^{m}19^{s}$	$-22^\circ16'01''$	08.07.2008	0.79	18.06.2009	0.88
18	$17^{h}36^{m}17^{s}$	$-21^\circ44'05''$	25.06.2008	1.05	16.06.2009	1.13
19	$17^{h}36^{m}16^{s}$	$-21^\circ12'03''$	25.06.2008	1.05	15.06.2009	0.91
20	$17^{h}36^{m}15^{s}$	$-20^\circ40'02''$	26.06.2008	0.95	19.06.2009	0.92
21	$17^{h}36^{m}14^{s}$	$-20^\circ07'59''$	26.06.2008	0.96	19.06.2009	1.15
22	$17^{h}34^{m}00^{s}$	$-20^\circ08'55''$	26.06.2008	0.93	13.08.2009	0.82
23	$17^{h}31^{m}41^{s}$	$-20^\circ07'59''$	26.06.2008	1.01	18.06.2009	1.27
24	$17^{h}29^{m}25^{s}$	$-20^\circ08'20''$	26.06.2008	1.17	12.06.2009	1.31
25	$17^{h}27^{m}14^{s}$	$-20^\circ09'08''$	26.06.2008	1.40	13.06.2009	1.06
26	$17^{h}24^{m}52^{s}$	$-20^\circ08'01''$	27.06.2009	0.95	19.06.2009	1.14
27	$17^{h}24^{m}50^{s}$	$-20^\circ40'03''$	08.07.2008	0.79	20.08.2009	0.80
28	$17^{h}24^{m}50^{s}$	$-21^\circ12'16''$	27.06.2008	1.14	12.06.2009	1.16
29	$17^{h}24^{m}48^{s}$	$-21^\circ44'06''$	27.06.2008	0.76	18.06.2009	0.93
30	$17^{h}24^{m}47^{s}$	$-22^\circ16'03''$	27.06.2008	0.76	18.06.2009	1.07
31	$17^{h}24^{m}45^{s}$	$-22^\circ48'04''$	27.06.2008	0.83	13.08.2009	0.97
32	$17^{h}27^{m}05^{s}$	$-22^\circ48'04''$	27.06.2008	0.83	18.06.2009	1.28
33	$17^{h}29^{m}23^{s}$	$-22^\circ48'04''$	08.07.2008	0.69	16.06.2009	0.92
34	$17^{h}31^{m}42^{s}$	$-22^\circ48'06''$	08.07.2008	0.81	20.08.2009	0.82
35	$17^{h}34^{m}02^{s}$	$-22^\circ48'20''$	05.07.2008	1.17	15.06.2009	1.30
36	$17^{h}36^{m}21^{s}$	$-22^\circ48'11''$	05.07.2008	1.07	15.06.2009	1.43
37	$17^{h}38^{m}38^{s}$	$-22^\circ16'16''$	05.07.2008	1.12	15.06.2009	1.27
38	$17^{h}38^{m}38^{s}$	$-21^\circ44'55''$	05.07.2008	0.54	13.08.2009	0.99
39	$17^{h}38^{m}35^{s}$	$-21^\circ12'20''$	05.07.2008	1.13	15.06.2009	1.16
40	$17^{h}38^{m}33^{s}$	$-20^\circ40'20''$	05.07.2008	1.19	20.08.2009	0.77
41	$17^{h}33^{m}58^{s}$	$-19^\circ36'22''$	05.07.2008	1.25	15.06.2009	1.42

Table 2.2: Observed fields and seeing conditions

	Center Position		Epoch 1		Epoch 2	
Mosaic	RA	DEC	Date	Seeing	Date	Seeing
42	$17^h31^m40^s$	$-19°36'04''$	07.07.2008	0.81	18.06.2009	0.86
43	$17^h29^m29^s$	$-19°36'53''$	06.07.2008	1.06	16.06.2009	1.37
44	$17^h27^m09^s$	$-19°35'57''$	06.07.2008	1.01	18.06.2009	1.48
45	$17^h22^m38^s$	$-20°40'47''$	06.07.2008	1.00	19.06.2009	1.27
46	$17^h22^m32^s$	$-21°11'59''$	06.07.2008	0.95	19.06.2009	1.25
47	$17^h22^m26^s$	$-21°44'21''$	06.07.2008	0.93	20.08.2009	0.86
48	$17^h22^m29^s$	$-22°16'15''$	06.07.2008	0.96	12.06.2009	1.00
49	$17^h27^m04^s$	$-23°20'04''$	07.06.2008	0.89	18.06.2009	0.90
50	$17^h29^m28^s$	$-23°21'07''$	06.07.2008	1.06	13.06.2009	1.15
51	$17^h31^m42^s$	$-23°19'58''$	06.07.2008	1.19	19.06.2009	1.27
52	$17^h34^m03^s$	$-23°20'21''$	06.07.2008	1.31	15.06.2009	1.45

2.1.2.1 Data Reduction

The acquired WFI data was reduced and processed into 2×52 mosaics, containing 9000×8650 pixels each, using the image reduction techniques and pipeline procedures from the Garching-Bonn Deep Survey (THELI; Erben et al. 2005). This pipeline enabled a uniform processing of all fields in both epochs with the best possible astrometric calibration, which is essential for the difference image technique.

Basic Calibration

All eight CCD-chips are treated individually, in order to achieve the best possible image co-addition. In a first reduction step, the raw frames, containing data from all chips, are split into individual files. Bias-subtraction and flat-field-correction in done afterwards, according to the standard procedures.

Astrometric Calibration

For each individual CCD-chip within a mosaic, a full astrometric solution was calculated, based on the positions of non-saturated stars. This ensures removal of image tilts and rotations invoked by microscopic mounting errors of the CCD-chips on the focal plane, as well as by optical distortions induced from the projection of the curved sky on the detector plane. After this internal astrometric calibration, the star positions in the CCD overlap regions are also fitted and a global fit to a reference catalog determines the absolute sky position. As a reference, the USNO-B1 catalog (Monet et al. 2003) was chosen. It features an absolute accuracy of about $0\overset{''}{.}3$ and a limiting R-band magnitude of 20. On average, this catalog provides about 25 000 stars per WFI field

Image Co-Addition

THELI performs a weighted mean co-addition using the `Drizzle` algorithm (Nonino et al. 1999). The weights are created based on normalized flat-fields to detect bad pixels (hot and cold pixels, bad columns, severe vignetting), cosmic ray identification (Nonino et al. 1999) and saturation detection using predefined thresholds. Prior to the actual co-addition, all images are brought to the same background level by subtraction of the night sky. The sky values are determined by subtracting all stars and large scale sources with at least 1.5σ over the sky-background and applying a convolution kernel with a size of 512 pixels (corresponding to $2'$).

To execute all reduction steps, the THELI-pipeline requires frequent user interaction. The required computation time to reduce a single mosaic is about 2.5 hours on a 2.5 GHz dual-core CPU with 4 GB RAM. Nevertheless, these steps yield to astrometrically well defined images, which can be easily registered using the IDL procedure `hastrom` for the following step to create difference images.

2.1.3 Difference Image Technique

As the atmospheric conditions (seeing and sky transparency) for any two observing times never match each other, a simple subtraction of two images would not yield the required accuracy to detect faint echo structures. Residuals due to different PSF size would dominate the resulting difference image. Therefore, it is necessary to find a suitable convolution kernel (K) to transform the PSFs of two images (I and J) into each other. Mathematical that means, one has to minimize the following equation

$$\sum \left([I \otimes K](x,y) - J(x,y)\right)^2 \tag{2.1}$$

by solving for the kernel K. I use the "High Order Transformation of PSF and Templates Subtraction" package (HOTPANTS) from A. Becker[1] to perform this kind of kernel fitting and image subtraction. This software has been successfully implemented into a number of data reduction pipelines, including SuperMACHO and the SDSS-II Supernova Search. Hotpants will also be used by the Large Synoptic Survey Telescope (LSST) collaboration.

The convolution kernel is build as a sum of three Gaussians, by comparing stellar sources from the two images, which have to be differentiated. As the convolution kernel is not globally constant over the entire image, for example due to distortion at the corner of the field-of-view, the entire image is divided into several sub-regions, in which a separate convolution kernel is fit. A region size of approximately 1000 × 1000 pixels delivers good results, while running with an acceptable computation time (2 hours).

---

[1] http://www.astro.washington.edu/users/becker/hotpants.html

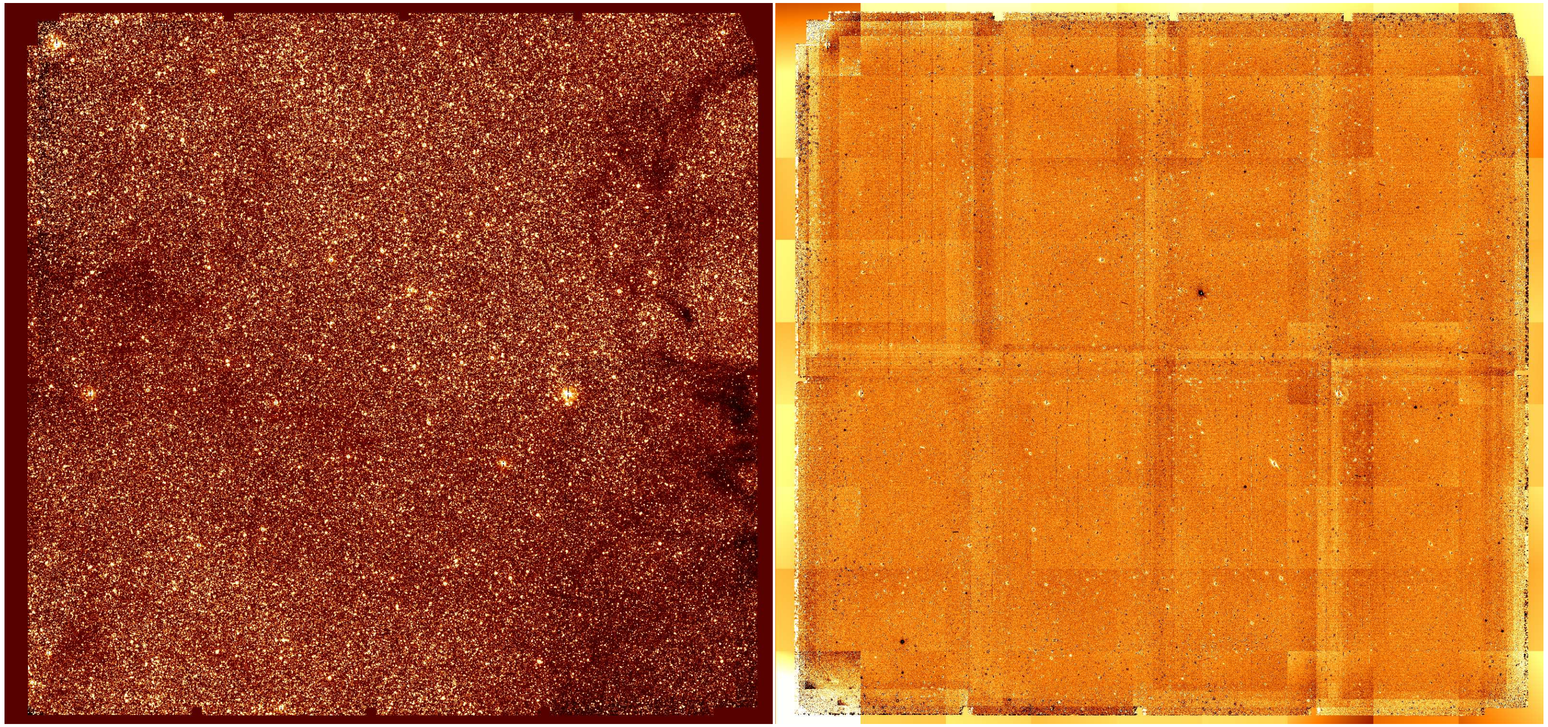

Figure 2.3: One of the 52 WFI fields, covering an area of 35.5′ × 34.2′ (mosaic # 13, centered at RA: $17^{\mathrm{h}}27^{\mathrm{m}}01^{\mathrm{s}}$, DEC $-22^\circ16'19''$) and the corresponding difference image between the 2008 and 2009 epoch. The WFI image contains more than 500 000 point sources; the difference image reveals 25 asteroids in the 2008 epoch and 35 asteroids in the 2009 epoch.

2.1.4 Analysis of Difference Images

2.1.4.1 Validation with known Tycho echoes

To validate and test the applied technique, I first analyze two-epoch imaging of a region with known light echoes around Tycho's supernova remnant. A field at RA: $00^{\mathrm{h}}28^{\mathrm{h}}07\overset{\mathrm{s}}{.}5$, DEC: $+60°05'54\overset{''}{.}55$ (J2000.0) was observed with the 2.2 m telescope on Calar Alto, which provides similar performance as the 2.2 m telescope at La Silla. Similarly to the Kepler light echo search, *R*-band imaging, with a total integration time of 20 min, was performed with the Calar Alto Faint Object Spectrograph (CAFOS). Both imaging epochs, and the resulting difference image, are shown in Figure 2.4.

At both epochs, emission from light echoes is already visible in the unprocessed

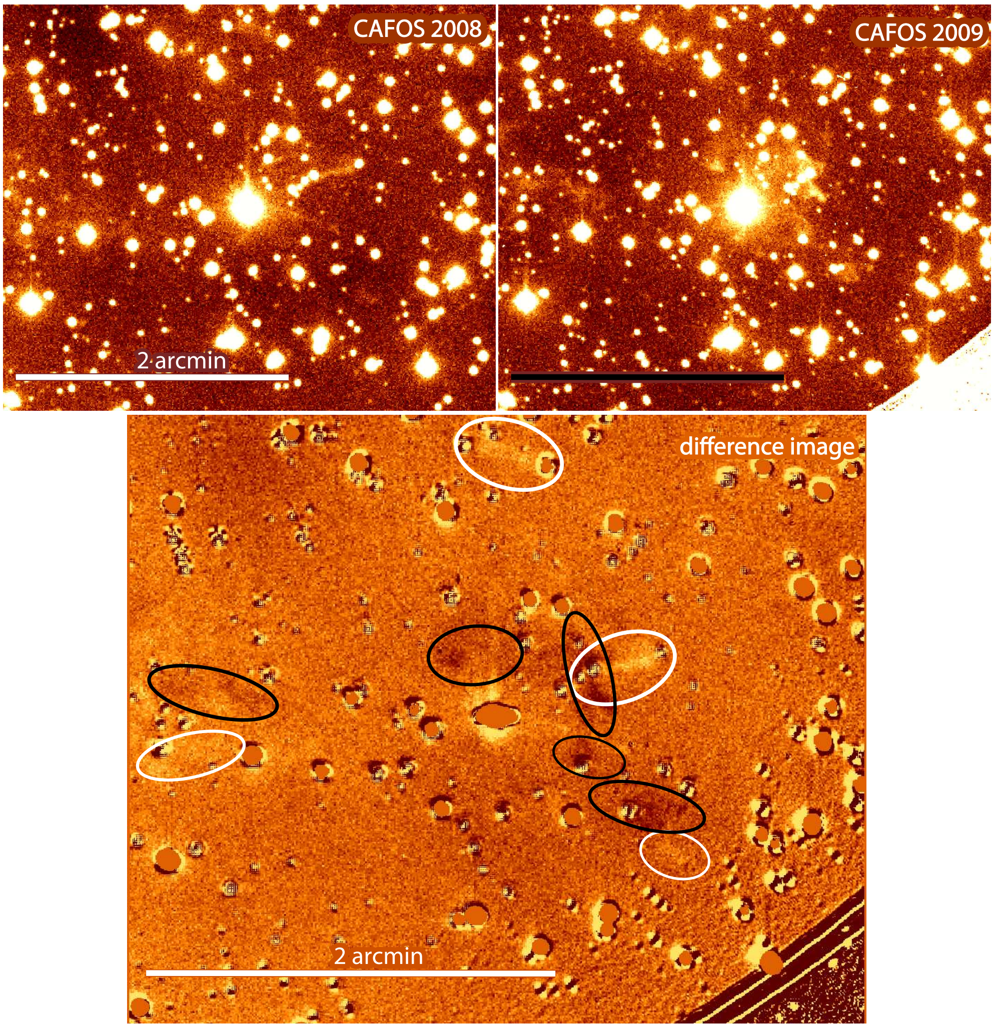

Figure 2.4: Two-epoch *R*-band imaging of an area with known light echoes around Tycho with CAFOS. Center of image is at RA: $00^{\mathrm{h}}28^{\mathrm{h}}07\overset{\mathrm{s}}{.}5$, DEC: $+60°05'54\overset{''}{.}55$ (J2000.0). The difference image reveals light echoes as either positive or negative pixel values (black and white ellipses).

images. The difference image reveals the echoing regions as either positive of negative pixel values across the field. The contrast between echoes and the background is higher in the difference image than in the single image, due to the removal of field-stars. This makes the identification of echoes by the human eye much easier.

As the CAFOS images were not processed to obtain a full astrometric solution, the subtraction process is imperfect and still leaves residuals at the position of many stellar sources. The fully processed WFI images around Kepler's supernova feature a much smoother background in the difference image. Stars above a predefined saturation threshold are zeroed out.

This example highlights that the detection of light echoes is easily possible by examining the difference image between two observing epochs. Even faint echo regions, embedded in a crowded field, can be found with this method.

2.1.4.2 Kepler Light Echo Candidates

The analysis of all 52 difference images between the 2008 and 2009 observations revealed no light echoes. No evidence for changing diffuse emission is present in any image. The difference images only show a number of asteroids (the ecliptic plane crosses the observed field), variable stars and other imaging artifacts, like optical ghost images.

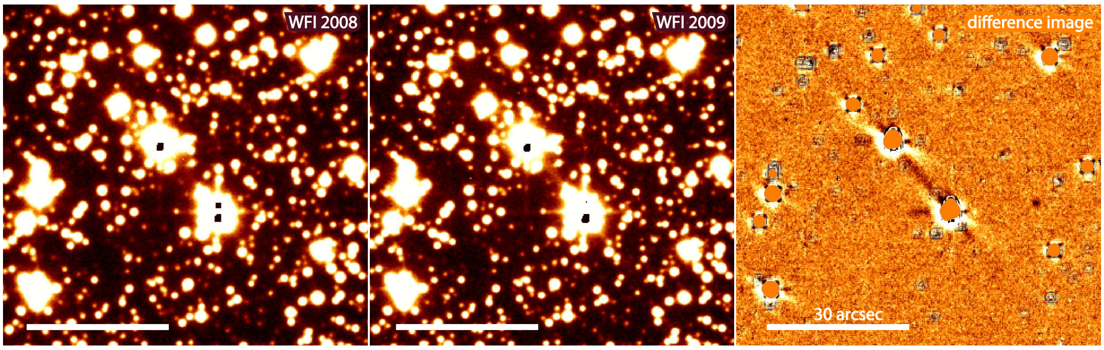

Figure 2.5: WFI observations from 2008 and 2009 and the corresponding difference image. Optical ghosts and reflexes can me misinterpreted as possible echo candidates. A slight rotation of the optical axis between the two epochs induces a positional change of these effects, for which the difference image is very sensitive. Such phenomena are similar around all bright stars in the field and thus can be excluded as light echo candidates.

An example of an image artifact is shown in Figure 2.5. Due to a slight image rotation in the two epochs, the two saturated stars leave slightly misaligned artifacts, which could be misinterpreted as emission from light echoes. As all other bright stars in this field deliver the same pattern, possible echo candidates could be ruled out immediately.

An example of a by-chance asteroid observation is shown in Figure 2.6. The path of the asteroid is easily discernible in the difference image, although it is not very prominent in the single frames due to the superposition of bright field stars. With respect to the average flux within a 100 pixel radius area around the white-encircled asteroid, the contrast in the difference image increases by a factor of 30. The distinctive

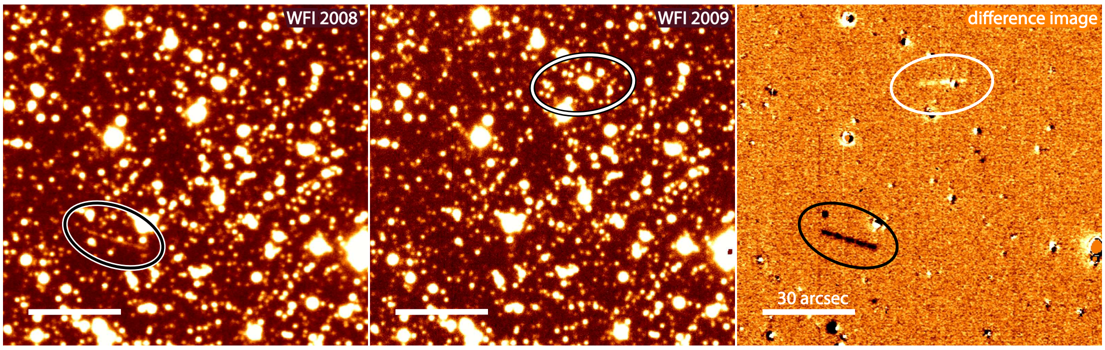

Figure 2.6: The trails of two asteroids are barely visible in the individual frames, but stand out clearly in the difference image between the two epochs. In comparison to the average flux within a 100 pixel radius of an asteroid, the contrast in the difference image is higher by a factor of ≥ 30. This field is located at RA: $17^{\mathrm{h}}26^{\mathrm{m}}18\overset{\mathrm{s}}{.}5$, DEC: $-22^{\circ}07'09''$ (J2000.0).

pattern of five elongated patches, separated by a tiny gap, originates from the five co-added 300 sec exposures and the time required for intermediate CCD read-out and telescope repositioning for dithering.

Although the examples above demonstrate the high sensitivity of the here applied difference image technique to detect variable sources, a possible failure of the method to identify diffuse echo emission, for example due to over-subtraction, was investigated. I visually compared all co-added images, by blinking the two epochs on a per-pixel basis (a total of 8.1 Gigapixels).

From the comparison it is evident that no bright and wide-spread diffuse echo emission, as seen from Tycho echoes and presented in Figure 2.4, is present in the entire 12.5 square-degree field. Several sky-positions featured some arcsecond-sized diffuse emission spots, which seemingly changed position and brightness between the two observing epochs. Such a region is shown in Figure 2.7. The corresponding difference image, how-

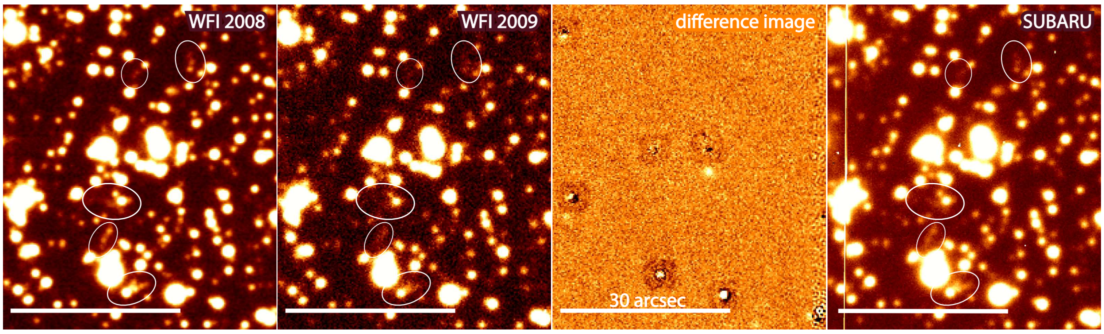

Figure 2.7: Faint diffuse sources at RA: $17^{\mathrm{h}}21^{\mathrm{h}}29\overset{\mathrm{s}}{.}6$, DEC: $-21^{\circ}49'40''$ (J2000.0) in the WFI 2008 image, which apparently changed in the 2009 image, but leave no trace of variability in the difference image. A 180 s Subaru image shows the same morphology as the 2008 image - no echo found here either.

ever, reveals no signs of variability; a `Simbad`[2] catalogue query lists no known astronomical sources at this position (RA: $17^{h}21^{m}30^{s}$, DEC: $-21°49'40''$, J2000.0). For further investigation we obtained a short Subaru-FOCAS acquisition image. The Faint Object Camera and Spectrograph (FOCAS) on the 8 m Subaru telescope would have been the instrument of choice for spectroscopic follow-up observations of light echoes. The 180 s FOCAS image has a similar depth as the 25 minute WFI exposure. In comparison to the 2008 maps, the new Subaru image shows no evidence of variability. Instead, the variations seen in the 2009 WFI image must be attributed to poor seeing and a lower transparency than in the earlier epoch. The diffuse faint emission probably originates from a galaxy cluster.

2.1.5 Search for Infrared Echoes with AKARI

Many light echoes around Cassiopeia A had been found in conjunction with infrared observations. Using regular infrared monitoring data from the MIPS 24 µm channel, Krause et al. (2005) were able to observe the first scattered light echo of Cas A. The thermal emission from echoing dust clouds is bright compared to surrounding cirrus clouds and emission from most stars is abscent in this wavelength regime, making the identification of echoes relatively easy, when multiple observation epochs are available. For Kepler, the *Spitzer* space telescope only observed the supernova remnant itself in a single epoch (Blair et al. 2007), making these observations unsuitable for the identification of infrared echoes.

The Infrared Astronomical Mission *AKARI* (also known as ASTRO-F, Murakami et al. 2007) is a Japan led space telescope, which performed an all-sky survey with a 9 and 18 µm filter using its infrared camera (IRC, Onaka et al. 2007). During the survey, each sky position should be observed at least twice. The survey results were published in form of a point source catalog[3], unfortunately no imaging data, suitable for a light-echo search, was released. Nevertheless, it was possible to obtain imaging products through the all-sky survey principle investigator, Dr. Ishihara, in May 2010. Figure 2.8 shows a $10° \times 10°$ field around Kepler at 18 µm during two epochs (September 2006 and March 2007).

The image quality of the second epoch is highly compromised due to proximity of the moon and the passage of the spacecraft through the South Atlantic Anomaly. About 50% of the original WFI monitoring area is not covered by the *AKARI* all-sky survey in this second epoch.

Analysis shows, that even the first *AKARI* epoch does not exceed a 5σ-point-source sensitivity of 0.12 Jy. This is roughly the brightness of the brightest infrared echoes around Cas A. The AKARI images show no signs of echo emission brighter than 0.12 Jy around Kepler and also do not show any other diffuse emission, for example from cirrus clouds. The data products from this mission are therefore not suitable to identify light echoes.

---

[2] http://simbad.u-strasbg.fr/simbad/

[3] available through http://darts.isas.jaxa.jp/astro/akari/cas.html

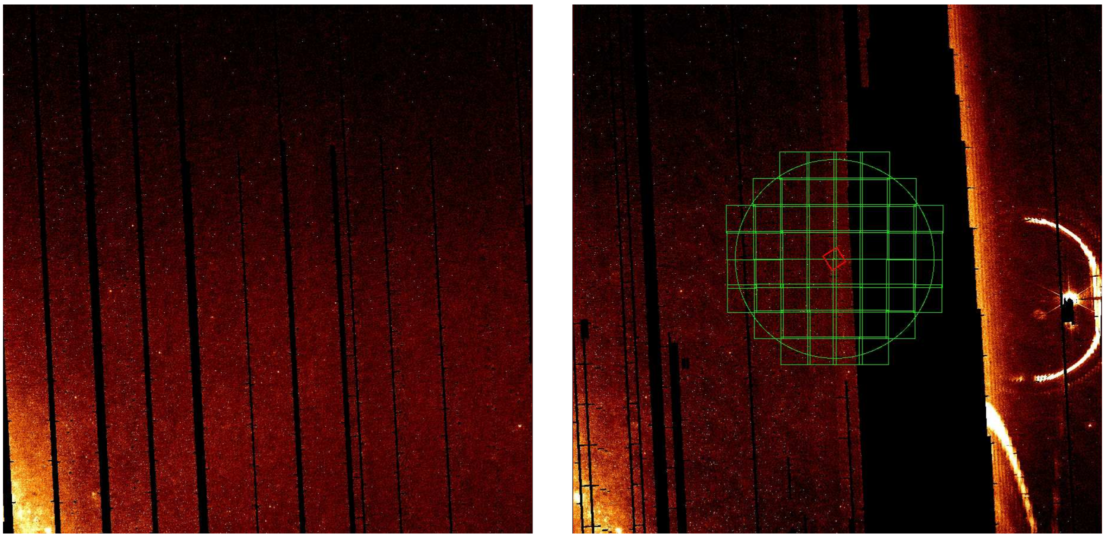

Figure 2.8: *AKARI* IRC maps at 18 µm, centered on Kepler's SNR (red box in the overlay on the 2007 image). The second observation from March 2007 has a poor quality due to the proximity of the moon and a spacecraft passage through the South Atlantic Anomaly. At a 5σ point-source sensitivity of 0.12 Jy, no emission from light echoes or other diffuse sources can be detected.

2.1.6 Summary and Outlook

Within a 2° radius around Kepler's supernova remnant no light echoes have been found. The applied technique has been successfully tested with known echoes around Tycho. Consequently, it can be concluded that no suitable optical echoes were present in the observed fields. Even if light echoes fainter than the achieved detection limit, mag 23.5, were present in the observed field, it would not be possible to spectroscopically analyze those regions, as the required exposure times would be too long and the much brighter, and omnipresent field stars would dominate any spectroscopic slit.

The recent release of data from the near- and mid-infrared all-sky survey mission *WISE*, which has a similar sensitivity and resolution as *Spitzer*-MIPS maps, opens new possibilities to search for infrared echoes and perform directed searches for the optical counterparts. The next chapter will describe a pathfinder-study of preliminary release *WISE* data to observe infrared echoes around Cassiopeia A. Future studies can use the therein established criteria to systematically search for light echoes around other historical supernovae, including Keplers SNR, over huge regions of the sky. In chapter 2.3, I provide an outlook with possible echo candidates.

2.2 Observations of Infrared Echoes with WISE around Cassiopeia A

In this section I use the Preliminary Data Release products from the Wide-Field Infrared Survey Explorer, in an attempt to identify previously unknown infrared echoes outside of the original Cassiopeia A Spitzer monitoring area. I find that echoes can be characterized by their morphology and their 22/12 µm *flux ratio.*
The results are valuable to perform optical follow-up spectroscopy to reveal supernova explosion mechanism asymmetries, as well as to map ISM structures around Cas A at previously unknown locations. I find indicators for dust processing with respect to distance from the supernova.
Parts of the following chapter have been published in Besel and Krause (2012), A&A.

2.2.1 The Wide-Field Infrared Survey Explorer

The Wide-Field Infrared Survey Explorer (*WISE*; Wright et al. 2010) is an all-sky near- and mid-infrared survey space telescope, which operated between January 2010 and February 2011. After its launch from Vandenberg AFB on December 14th 2009, *WISE* entered a sun-synchronous orbit and surveyed the entire sky in four infrared bands (3.4, 4.6, 12 and 22 µm) simultaneously. The 1°/day precessing orbit and the $47' \times 47'$ detectors allowed a survey strategy, which observed the same region on the sky about 12 times on average (lower coverage (~ 8) is found at the ecliptic equators, while the ecliptic poles were observed during every scan leg). This approach allows multiple redundancy to get a higher signal-to-noise ratio as well as the ability to detect moving or shortly variable objects (e.g. asteroids or flaring black-holes). The entire sky was surveyed within a six month time-span. *WISE* ceased cryogenic observations on August 6th 2010, but continued observations with warmed-up detectors in the two shorter bands until February 1st 2011. This resulted in partial dual- (and triple-) epoch coverages on the sky (see Figure 2.9), which are of great interest to search for infrared echoes.

The 40 cm telescope and optical components of *WISE* are placed inside a solid-hydrogen cryostat. Table 2.3 summarizes the optical characteristics of the four bands. All detectors feature 1024^2, 18 µm sized pixels. *WISE* works diffraction limited at 12 and 22 µm. At the shorter passbands a combination of attitude control errors, optical track errors and undersampling of the PSF limits the resolution to about $6''$ (FWHM). Exposure times were 7.7 seconds (3.3 and 4.6 µm) and 8.8 seconds (12 and 22 µm).

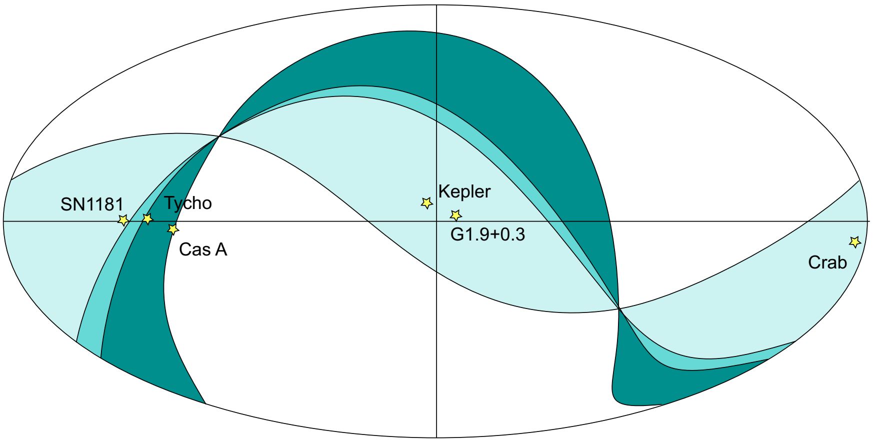

Figure 2.9: Dual-epoch coverage in a Galactic coordinate illustration. The colored areas have been observed during a second epoch with a time gap of approximately six months under cryogenic conditions. The darkest shade corresponds to the area covered by all photometric bands. The 22 µm band was disabled in the middle shade, and both 22 µm and 12 µm were disabled in the lightest area. Although the white areas are also covered in a second epoch of observations, only the two shortest wavebands were used. Data from this region were used exclusively by the NEOWISE mission extension and will not be published in imaging formats.

2.2.1.1 Data Products and Data Reduction

In the framework of the Preliminary Data Release, the Infrared Science Archive (IRSA)[4] from NASA/IPAC provides all single exposure frames as well as stacked "Atlas-" Images from the first 105 days of the *WISE* mission.

The single exposure frames are photometrically and astrometrically uniformly processed at the original image scale ($2.75''$ and $5.5''$ @ 22 µm). For this, the *WISE* Science Data System (WSDS) corrected raw-frames for droops (an additive signal proportional to the total signal and/or to a particular bright pixel), dark-current subtraction, linearity calibration on a per pixel basis, flat-fielding (created like a Master-Flat from the entire survey data) and a step called sky-correction, which subtracts a moving median of 40 flattened images; this step removes short-term variations in the bias and dark structure, as well as long term effects like latents.

The Atlas Pipeline produces 4095^2 images at a pixel scale of $1.375''$/pix. These images are co-added from the individual Single Exposure Frames, after they were brought to a common photometric zero-point and were background level matched. As this is done on a per-tile basis, the background gradients are not continuous across the Atlas tile boundaries and would introduce a systematic step-like pattern across the sky if several Atlas images would be stitched together.

When *WISE* started its all-sky survey on January 14th 2009, it pointed its first survey leg $20'$ to the southwest of Cassiopeia A, yielding a full coverage of the eastern part of the

---

[4] http://irsa.ipac.caltech.edu/applications/wise/

Table 2.3: WISE instrumental characteristics.

Wavelength	3.35 µm	4.60 µm	11.56 µm	22.08 µm
Detector	HAWAII 1RG (Teledyne)		Si:As (DRS)	
Temperature	32 K		8 K	
Pixel Size [arcsec]	2.75	2.75	2.75	5.5 (binned)
FWHM [arcsec]	5.79	6.37	6.60	11.89
5σ point source sensitivity [mJy]	0.048	0.1	0.73	5.9
Saturation limit [Jy]	0.3	0.5	0.7	10.0

Notes – Sensitivities are stated for a nominal 8 frame coverage. As most fields feature deeper coverages, these values should be seen as a lower limit.

original *Spitzer* infrared echo monitoring area, which will be described in section 3.1. In order to find infrared echoes, it is necessary to examine huge areas of the sky, which are uniformly processed; thus, I used Single Exposure images to avoid the inconsistencies induced by stitching Atlas images and their varying backgrounds. I obtained about 6700 Single Exposure images (equaling about 26 gigabyte) per wavelength band through IRSA, from an 8.5° × 16° area adjacent to Cassiopeia A. The portion of the original *Spitzer* infrared echo monitoring area makes out approximately 1/20th of the new *WISE* map.

Prior to any post-processing steps, all images had to be corrected for zodiacal light contamination. Zodiacal light arises from the illumination of the interplanetary dust cloud within the solar system. Kelsall et al. (1998) used *DIRBE* data to construct a three-dimensional model of the dust cloud and built a software tool to calculate near- and mid-infrared intensities of zodiacal light, which reflects seasonal and line-of-sight variations. Depending on the observation day and sky position, the zodiacal light was removed on a per-pixel basis in all Single Exposure images.

The `Montage`[5] software package from IPAC was used to process and co-add the zodiacal light corrected Single Exposure images for a final pixel scale of $2.0''$/pixel. This samples the instrumental PSF well ($\sim 6 - 12''$), while not exceeding disk and memory space as much as the Atlas tile pixel size of $1.375''$/pixel (factor of ~ 2 in file size). In the first step the input images are projected onto the predefined output grid. A tangent-plane projection, which is half centered around the supernova remnant, was chosen. Afterwards the overlapping input pixels are co-added by determining the median flux in each pixel stack. This removes most artifacts described in the *WISE* Explanatory Supplement, although not bright artifacts such as latent images or (minor-) planets. These artifacts do not impede the identification of light echoes, thus I do not try to correct for them at this time. On average all final mosaicked pixels contain input information from 19 single exposure images, except for the most eastern $30'$, where the survey coverage of *WISE* started.

The data products provided by IRSA have intensity units of ”Digital Numbers” (DN). In order to perform photometric measurements, the *WISE* Preliminary Data Release Explanatory Supplement provides a preliminary absolute flux calibration. The used

---

[5] http://montage.ipac.caltech.edu/

DN-to-Jy conversion factors are listed in Table 2.4. Absolute calibration is based on observations of calibrator sources near the ecliptic poles, which *WISE* scans in nearly every survey leg. The internal photometric stability of *WISE* is better than 0.1% throughout the entire mission (Jarrett et al. 2011).

Table 2.4: WISE calibration factors

Band	3.4 µm	4.6 µm	12 µm	22 µm
center wavelength	3.353 ± 0.013	4.603 ± 0.017	11.561 ± 0.045	22.09 ± 0.12
bandwidth [µm]	0.6625 ± 0.0012	1.042 ± 0.0011	5.507 ± 0.017	4.101 ± 0.048
DN-to-Jy conversion [10^{-6} Jy/DN]	1.935 ± 0.046	2.705 ± 0.076	2.90 ± 0.13	0.523 ± 0.030

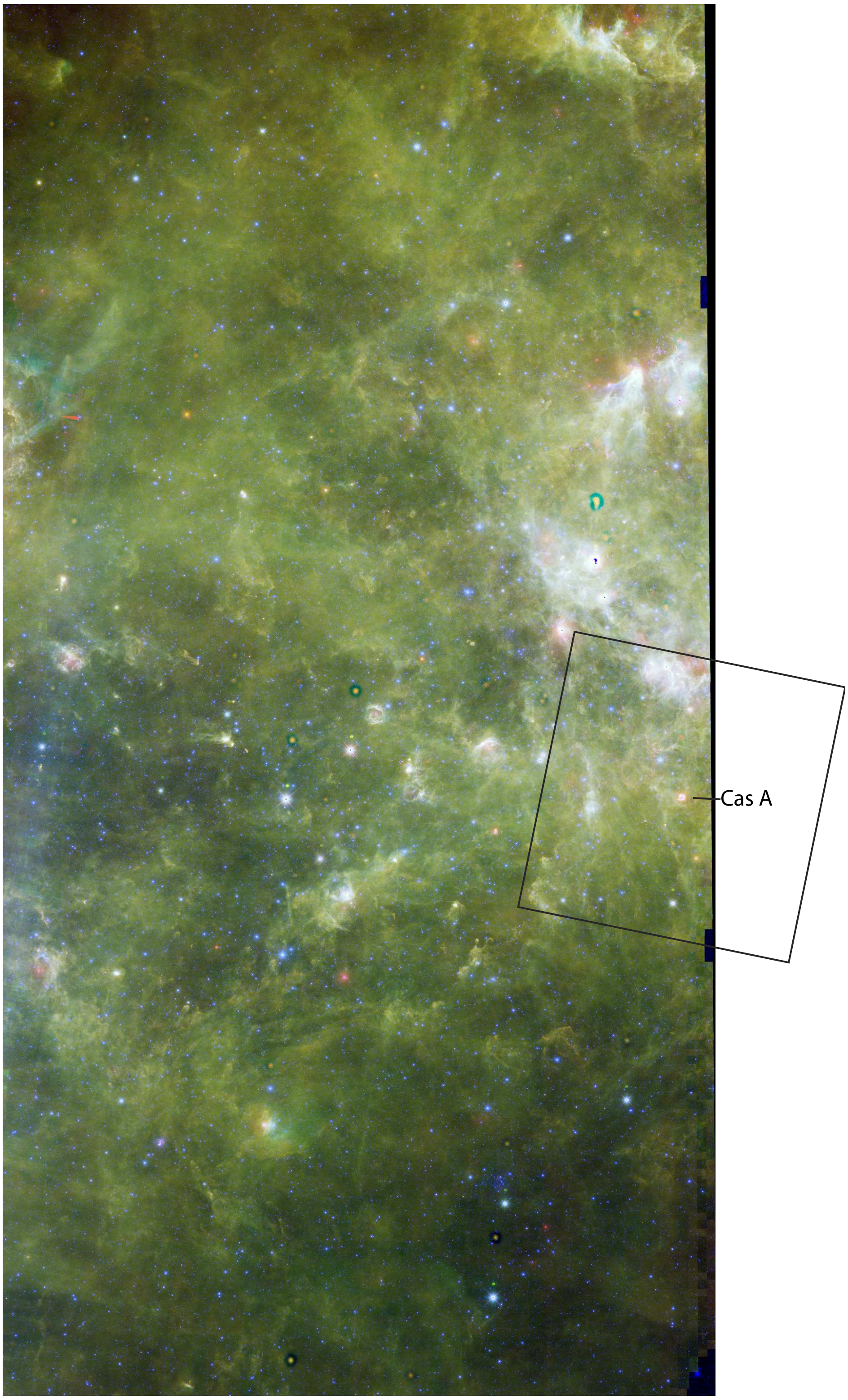

Figure 2.10: Three color representation of the here analyzed *WISE* field – *red*: 22 µm, *green*: 12 µm, *blue*: 3.4 µm. The field has a size of approximately 8.5° × 16°. At full resolution this image features 15 267 × 29 561 pixels per wavelength band.

2.2.2 Data Analysis and Discussion

In an attempt to identify infrared echoes over huge regions on the sky and under possibly varying illumination conditions, I first compare an area with many known infrared echoes from *Spitzer*-MIPS images with the new *WISE* map to explore possibilities to distinguish echo emission based on their properties in the *WISE* 22 and 12 µm bands. With this knowledge, it is then possible to extend the area of known infrared echoes beyond the original *Spitzer* fields.

2.2.2.1 Spitzer-WISE Difference Images

Since the last *Spitzer*-MIPS images were taken in 2008, the UV and optical bursts of the supernova illuminate different parts of interstellar dust clouds, making the projection of echoes on the sky appear as ”moving” or ”varying” structures. Although echoes can appear on the same spot on the sky in different observing epochs, they do not probe the same position in an interstellar cloud structure. As clouds are inhomogeneous objects, it is unlikely that the same position on the sky appears exactly alike at different epochs, which is easily discernable with the difference image method.

Figure 2.11 shows a *WISE* two-color composite along with a *Spitzer-WISE* difference image. The *Spitzer* 24 µm image (FWHM $6.45''$) was taken on January 29th 2006 (PID: 20381; PI: O. Krause) and was convolved to match the *WISE* 22 µm resolution (FWHM $11.9''$). Prior to the difference image creation, the two images were background-subtracted (via a common field with the lowest background emission possible) and scaled to the same Jy/pixel units.

The resulting difference image is mostly free of signatures from cirrus clouds. Only light echoes, along with variable stars, asteroids, latent images, and other artifacts, such as those produced by saturated PSF's, can be seen. Adjacent black and white structures are indicative of ”varying” or ”moving” structures. Echoes in the *WISE* image appear as positive pixel values (white color), while the negative ones (black) belong to the *Spitzer* map. This method is even sensitive to very low surface brightnesses or echoes, which cannot be directly identified in raw images.

2.2.2.2 Light Echoes Revealed by their 22/12 µm Flux Ratio

Comparing the difference image with the *WISE* 22–12 µm color-composite reveals that infrared echoes are characterized by reddish colors with respect to surrounding cirrus clouds (green). Closer examination shows that all visually confirmed echoes have a 22/12 µm flux ratio greater than 1.0, which is larger than the ratio for surrounding cirrus clouds.

Thus, I am able to extend the search area beyond the limit of the original $3^\circ \times 3^\circ$ maps by *Spitzer*, where the difference image technique cannot be applied.

Infrared echoes roughly share the same 22/12 µm color space as young stellar objects (YSOs) or quasi-stellar objects (QSOs). However, they can be discriminated in terms of their morphology. Most echoes have compact, unresolved knots that are connected by diffuse filamentary emission, while YSOs and QSOs are isolated point-sources.

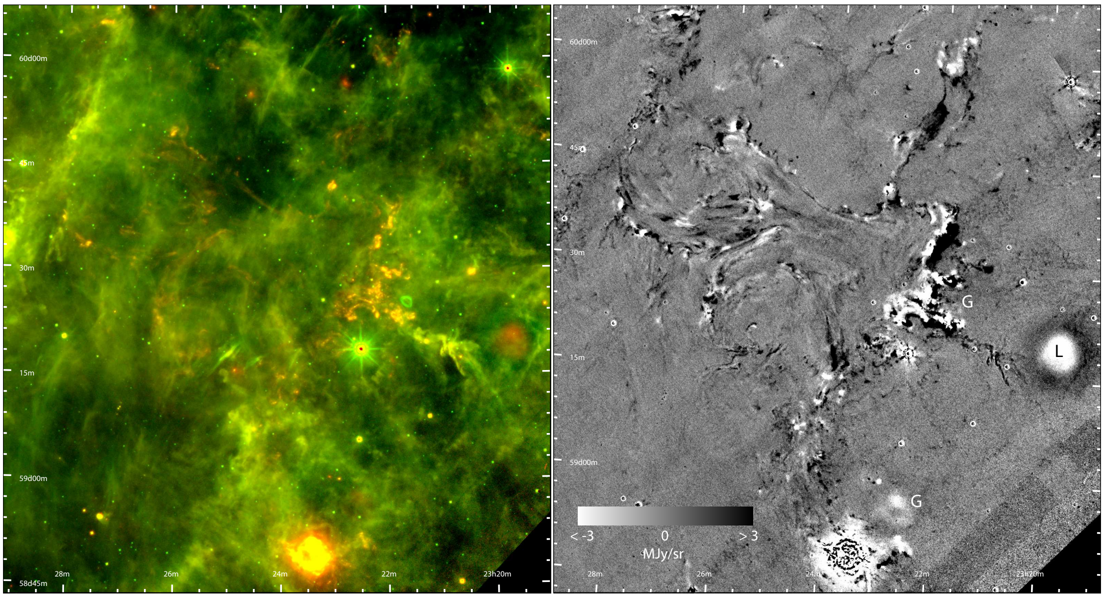

Figure 2.11: *left: WISE* two-color composite – *red*: 22 µm, *green*: 12 µm – of a particular active echoing region. The Cassiopeia A supernova remnant is visible at the lower border of the image. Light echoes are clearly seen as reddish filamentary structures distributed all over the field of view.
right: Two-epoch difference image from a *Spitzer*-MIPS 24 µm (2006) image and the *WISE* 22 µm image. Cirrus regions cancel out to a smooth background, while echoes can be identified as white (2010) or black (2006) structures. Saturated stars leave residuals owing to their complex outer PSF; a *WISE* latent image (marked "L") and a ghost ("G") of Cas A can be seen as white structures. Greyscale values correspond to flux variations in the range from −3 MJy/sr to +3 MJy/sr. Blacks and whites are saturated and can correlate to flux densities of up to ± 150 MJy/sr

To quantify the flux ratio, I measured echo regions and selected cirrus structures across the field of view. Cirrus regions were chosen to cover the full dynamic range of observed brightnesses. Photometry was carried out relative to "floor" points, separated by $\sim 17°$, at the northern and southern edges of the field. These regions mainly contain an offset signal and feature very low cirrus emission (~ 1 MJy/sr at 22 µm), as they are most distant from the Galactic plane. I performed the background subtraction as a constant offset over the entire field, as the variation in the background between the northern and southern floor points is on the order of 2%, which is similar to the inter-pixel variations of $\sim 3\%$. The main uncertainty in background subtraction arises from the remaining cirrus contamination at these floor points; I estimate this uncertainty to be 7%, yielding a total background subtraction uncertainty of $\sim 8\%$.

Figure 2.12 c shows a color-brightness diagram for all measured structures. Cirrus regions have an average 22/12 µm flux ratio of 0.83 ± 0.04, which compares well with the expected ratio of 0.86 for the standard ISM illuminated by the standard interstellar radiation field (calculated based on dust models by Draine and Li (2007) or Zubko et al. (2004), in concordance with *DIRBE* and *IRAS* observations). All light echoes

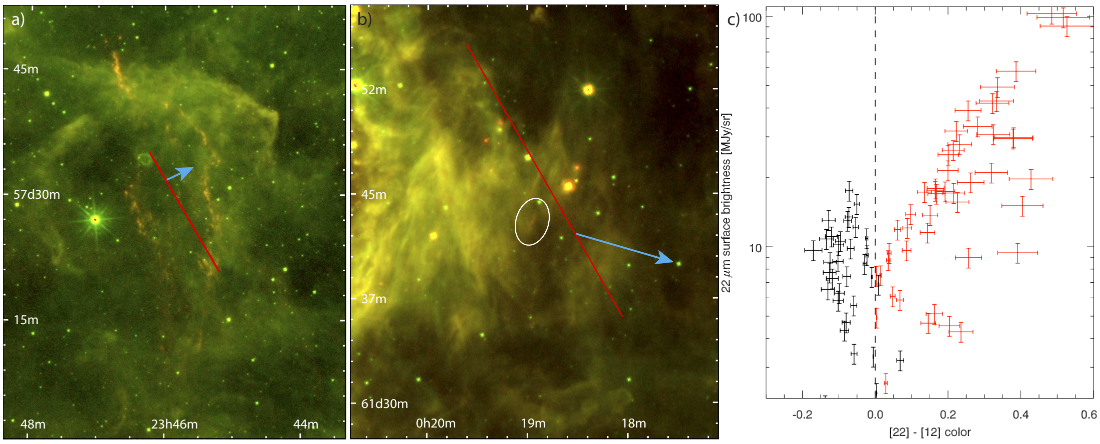

Figure 2.12: *a) WISE* two-color composite – *red*: 22 µm, *green*: 12 µm. The red line marks the extend and position of this echoing region as previously reported in scattered light by Rest et al. (2008). This region is referenced with "O" in Table 2.5.
b) Most distant infrared echo from Cas A at a distance ∼ 800 pc. The red line marks the location of the previously observed scattered light echo as reported in Rest et al. (2008), while the cyan arrow marks the direction towards Cas A. This region is referenced with "T" in Table 2.5.
c) Color-brightness diagram of echo regions (red data points) and selected cirrus regions (black data points). The [22]–[12] color is defined as $log_{10}(F_{22}/F_{12})$. Errors mainly arise from uncertainties in background subtraction and flux calibration. All infrared echoes are characterized with flux ratios > 1.0 (a flux ratio of 1.0 corresponds to a color of 0.0).

are characterized by 22/12 µm ratios greater than ∼ 1.0.

Figure 2.13 sketches the locations of all infrared echoing regions from the here described *WISE* field. The outer regions represent the first observations of infrared echoes at distances ≥ 500 pc from a supernova remnant. Full positional properties are given in Table 2.5.

2.2.2.3 The 22/12 µm Flux Ratio as an Indicator for Dust Processing

In chapter 3.2, the effects of the supernova radiation bursts on ISM dust is discussed by means of modeling infrared echo SEDs with different amounts of PAH dehydrogenation and dust destruction. It is found that a particularly bright echo, observed with the Infrared Spectrograph aboard *Spitzer*, at a distance of ≈ 60 pc from the supernova remnant, shows signatures of such dust processing. Small PAH's with ≤ 300 carbon atoms seem to be completely removed and hydrogen atoms from bigger PAHs seem to be partially removed.

The 12 µm band is very sensitive to the 11.3 µm PAH C–H out-of-plane bending mode, which was found to be highly degenerated. Thus, large 22/12 µm ratios are indicative of both dust destruction and PAH dehydrogenation. As the radiation field diminishes as r^{-2}, one would expect the ratio to decrease with distance from the supernova. At

Table 2.5: Positions and properties of detected infrared light echoes around Cassiopeia A

region identifier	RA J2000	DEC J2000	distance [pc] (1)	z [pc] (2)	scattering angle [degrees] (3)	PA [degrees] (4)	MSB @ 22 µm [MJy/sr] (5)	22 µm / 12 µm ratio (6)
A	$23^{h}23^{m}06^{s}$	$58°45^{m}15^{s}$	52.1	−51.9	175.1	−141.8	17.89	2.43
B	$23^{h}22^{m}31^{s}$	$58°52^{m}\ 1^{s}$	52.3	−51.7	171.3	−66.3	21.87	1.64
C	$23^{h}21^{m}16^{s}$	$58°38^{m}38^{s}$	53.9	−50.0	158.5	−120.5	25.83	2.08
D	$23^{h}23^{m}42^{s}$	$59°12^{m}21^{s}$	54.6	−49.2	154.7	4.5	23.35	1.71
E	$23^{h}22^{m}12^{s}$	$59°23^{m}16^{s}$	58.1	−45.7	142.4	−15.7	95.01	2.68
F	$23^{h}28^{m}18^{s}$	$58°35^{m}49^{s}$	59.5	−44.2	138.6	108.6	3.31	1.05
G	$23^{h}26^{m}03^{s}$	$59°48^{m}59^{s}$	71.1	−32.3	118.1	17.9	35.19	1.88
H	$23^{h}19^{m}01^{s}$	$59°48^{m}36^{s}$	74.5	−28.8	113.9	−29.2	15.12	1.61
I	$23^{h}21^{m}34^{s}$	$60°\ 3^{m}35^{s}$	79.5	−23.6	108.5	−10.8	15.06	1.56
J	$23^{h}27^{m}23^{s}$	$60°\ 4^{m}57^{s}$	83.7	−19.3	104.7	21.0	27.45	1.87
K	$23^{h}14^{m}37^{s}$	$59°40^{m}26^{s}$	86.4	−16.5	102.4	−51.8	37.89	2.45
L	$23^{h}23^{m}51^{s}$	$60°22^{m}58^{s}$	93.9	−8.8	96.9	1.8	7.46	1.43
M	$23^{h}33^{m}20^{s}$	$59°45^{m}\ 4^{s}$	93.9	−8.8	96.9	52.3	8.06	1.25
N	$23^{h}30^{m}25^{s}$	$60°25^{m}54^{s}$	109.3	7.1	88.1	27.7	8.66	1.28
O	$23^{h}46^{m}43^{s}$	$57°45^{m}\ 4^{s}$	223.1	124.4	59.3	106.7	17.71	2.11
P	$23^{h}37^{m}55^{s}$	$61°43^{m}49^{s}$	242.5	144.3	56.9	30.0	11.74	1.45
Q	$0^{h}01^{m}31^{s}$	$57°50^{m}25^{s}$	445.9	354.0	42.5	97.0	4.12	1.54
R	$23^{h}01^{m}43^{s}$	$65°10^{m}21^{s}$	705.5	621.6	35.1	−19.5	3.77	1.15
S	$0^{h}01^{m}44^{s}$	$62°30^{m}54^{s}$	571.5	483.4	38.2	47.6	3.19	1.13
T	$0^{h}18^{m}57^{s}$	$61°42^{m}56^{s}$	799.4	718.4	33.5	61.2	4.95	1.13

Notes – The table lists the properties of the brightest echoing features in the regions defined in the Fig 2.13.
(1) Direct distance between supernova and echoing dust cloud.
(2) Distance between supernova and dust cloud along the line of sight - negative values indicate a position behind the SNR with respect to Earth.
(3) Scattering angle.
(4) Position angle with respect to the SNR. North is 0°, east +90°.
(5) Maximum surface brightness in the 22 µm band; no local cirrus subtraction.
(6) 22/12 µm flux ratio average across the region; no local cirrus subtraction.

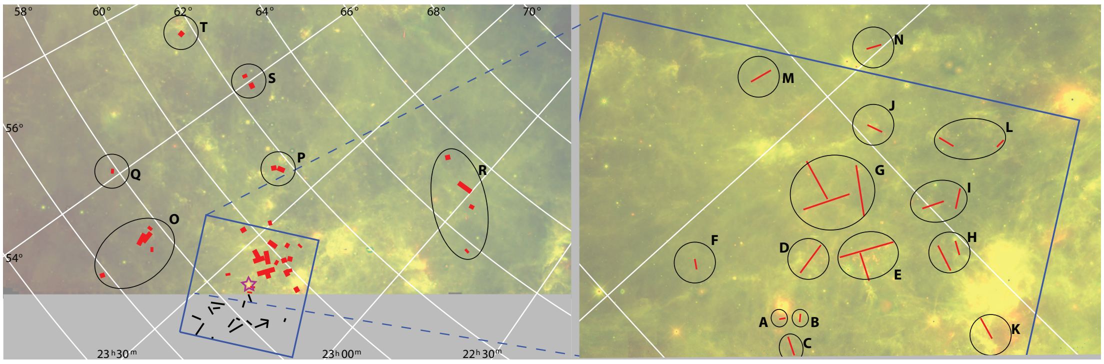

Figure 2.13: Sketch of echo positions (red markers) in the field described in this study. The original 3° × 3° MIPS field is depicted in blue with the major light echo positions in black (for clarity only MIPS-LE positions outside the *WISE* coverage are marked). The full positions and properties of marked regions are presented in Table 2.5.

a distance of $d = 60\,\mathrm{pc}$ from the supernova, the expected color ratios for infrared light echoes are 2.5 for processed and 1.4 for pristine dust. These ratios change to 1.7 and 1.0 at a distance of $d = 600\,\mathrm{pc}$. The SEDs for processed dust close to the supernova remnant and pristine dust at greater distances are plotted in Figure 2.14.

The measurement of this effect with only one observing epoch at different echoing positions remains challenging, as the local cirrus structure varies on the same spatial scales as light echoes. Thus, it is impossible to calculate a physical 22/12 µm ratio, which is intrinsic to the echo region itself.

Flux ratios estimates, based on global background subtraction, are given in Table 2.5 and in Figure 2.14. As these ratios still include the local cirrus emission contribution, the echo-intrinsic values may be higher by several tens of percents. The resulting ratios are within the range of the expected values for both processed and pristine dust.

Estimation of the local background is especially difficult at 12 µm, where the cirrus-echo contrast is at its lowest. Any estimation would be unable to derive reliable flux ratios. For this reason, I cannot comment on the possibility of varying intrinsic flux ratios in different echo regions at this time.

However, I want to point out that data acquired at a second observing epoch could help to precisely disentangle echo emission from cirrus emission and would yield interesting insights into dust processing by the supernova radiation.

2.2.3 Conclusions and Outlook

WISE allows the detection of previously unknown infrared echoes around Cas A. The final data release will also include echo regions on the western side of the remnant seen on *Spitzer* images, but not covered in the preliminary release data. The final

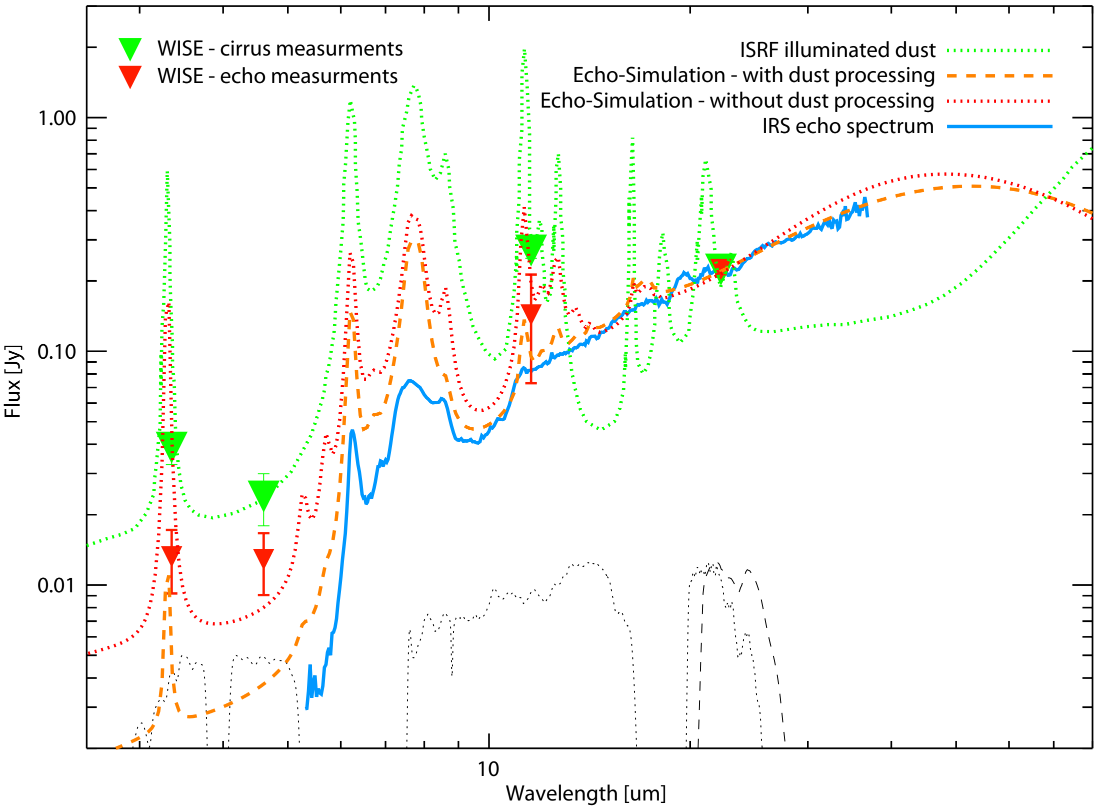

Figure 2.14: SED of infrared echoes and cirrus clouds. All SEDs and photometric points are scaled to have a common 22 µm flux density. The photometry in the 3.4 and 4.6 µm bands is based on four regions only, as the bright stellar emission in these bands inhibits accurate measurements for most regions. At 12 and 22 µm all regions from Table 2.5 were used. The error bars illustrate the observed variations of flux densities in different regions.
The IR echo SEDs do not account for flux contribution by scattered light echo emission, which increases the observed flux at 3.4 and 4.6 µm. The *WISE* and MIPS 24 µm normalized filter curves are sketched at the bottom for illustration (arbitrarily scaled for least interference with SEDs).

data release is currently scheduled for spring 2012[6] and covers 99.92% of the sky. The data products in this release use a complete and uniform reprocessing of the entire data produced by *WISE*. The best available calibration and processing parameters are derived from the analysis of payload and spacecraft performance during the lifetime of the mission and from analysis of the Preliminary Data Release processing results.

The complete mapping of infrared echoes allows new pointed searches for scattered light echoes, and follow-up spectroscopy of supernova spectra under new illumination and scattering conditions, possibly revealing new knowledge about supernova explosion

---

[6] The actual data release was on March 14th 2012; in section 2.3.3.2 I give a quick-look image comparison, which confirms the echo nature of region ”T”, which is most distant one from Cas A.

mechanisms and asymmetries.

As the spacecraft started its survey close to the supernova remnant, the aforementioned area was observed for a second time after the first all-sky scan was completed on July 17th 2010. *WISE* continued survey observations until February 9th 2011 allowing a second (and partially third) all-sky scan. However, owing to the cryogen exhaustion on September 29th 2010, not all photometric bands were used for the entire time. The lowest coverage is found in the 22 µm band, but still includes the entire area west of Cas A described here (see Figure 2.9)

At 12 µm, the dual-epoch coverage is larger (10 degrees, at the ecliptic equator) and includes an area with known optical light echoes around Tycho's supernova remnant.

The largest cryogenic coverage is found in the two shortest wavelength-bands and includes areas around the historical supernova remnants SN1181, Kepler, Crab and G1.9+0.3. However these short wavelength are already very crowded by the stellar emission from field stars. As *WISE* features a very stable PSF, the dual-epoch difference image should nevertheless reveal bright infrared echoes from these supernovae.

This second epoch data will also enable us to perform an accurate determination of the superimposed cirrus component, yielding physical 22/12 µm flux ratios for echo regions that changed their position sufficiently during these two epochs. Such studies will help to provide new insights into ISM structure and dust physics. Dust destruction efficiencies can be mapped as a function of distance from the supernova; in turn, a change in the dust destruction efficiencies can map supernova-explosion, circumstellar-material, and interstellar-material asymmetries.

On January 10th 2012 a "sneak preview" of the Final Data Release was presented by NASA; this image is presented in Figure 2.15. It covers a portion of the Milky Way with high star formation activity and many supernova remnants; it encloses the region described in this chapter as well as the complete *Spitzer* echo monitoring area. The image itself reveals all bright infrared echoes in the area not covered by the Preliminary Data Release.

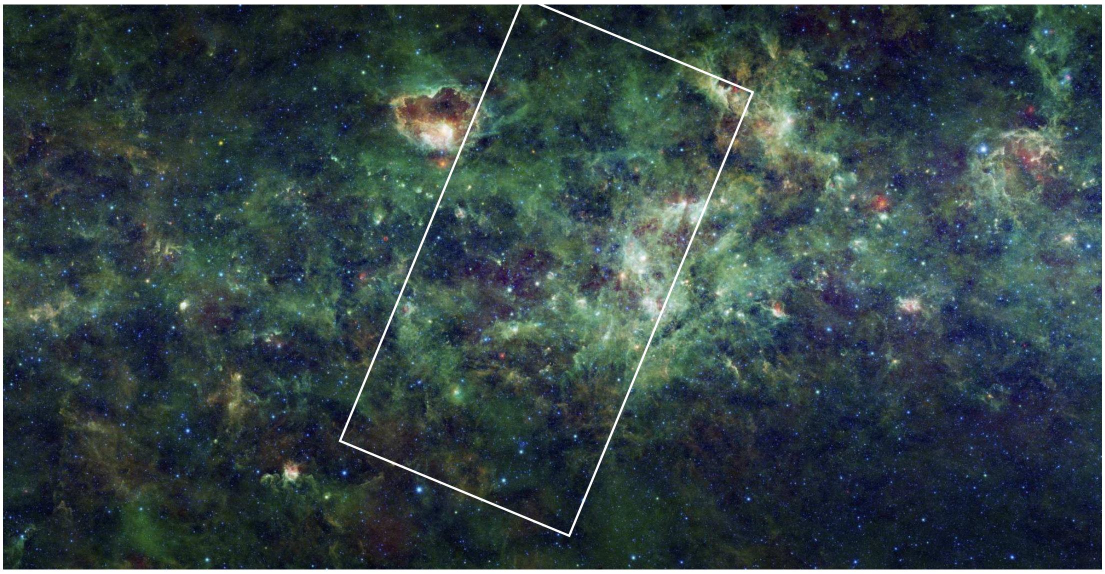

Figure 2.15: Sneak preview image from the Final Data Release from the *WISE* team. Blue and cyan represents the 3.4 and 4.6 µm channels, while green and red represent emission from 12 and 22 µm. The region analyzed in this work is sketched as a white box. Some bright infrared echoes, not covered in the Preliminary Data Release are visible just right to Cas A. Tycho's supernova remnant can be seen to the left of the field. Image Credit: NASA/JPL-Caltech/*WISE* Team

2.3 Infrared Echo Candidates around Crab, Kepler, Tycho and SN1181

Using the capabilities of Preliminary Release WISE all-sky data, I search an area of about 1800 square-degrees to identify infrared echoes from various historical supernova remnants. Based on color, morphology and comparison against IRAS data I find several echo candidate regions, which I list in this chapter. Future optical follow-up observations or two-epoch WISE images are needed to confirm the echo nature of these objects.

2.3.1 Data Set

As seen from the example of infrared light echoes around Cas A in the previous chapter, echoing structures can be spread over huge areas. In the special case of Cas A, echoes were found as far as 7° apart from the supernova remnant. Echoes from old Galactic supernova remnants may therefore be distributed across significant portions of the sky, making pointed searches nearly impossible.

The *WISE* Preliminary Data Release covered already 57% of the entire sky, including regions around the Galactic SNR's SN1054 (Crab Nebula), Cas A, Tycho, SN1181 and Kepler. I tried to analyze huge regions around these remnants to compile a list of possible light echoes.

To create large mosaics of the sky, the preferred method is to process and co-add single exposures images from the *WISE* data archive. These images are unprocessed and were not background-subtracted by the *WISE* science data pipeline. For computational convenience, however, I used the Atlas images for the mosaic creation with the Preliminary Release Data. To create a mosaic of $30^\circ \times 30^\circ$, for example, 125 000 single exposure frames would have to be downloaded and reduced from the data archive *per* wavelength band. For a two-waveband coverage, these images would already have a total file size of more than 1 TB. Atlas images are already co-added single exposure frames and cover an area of $1.5^\circ \times 1.5^\circ$. This reduces the computing requirements significantly, as the same $30^\circ \times 30^\circ$ area would be covered by only 1000 Atlas mosaics, with a file size of 120 GB for two bands.

As the Atlas images are co-added on a per-tile basis, they introduce non-continuous background variations when creating larger mosaics from them. The *WISE* pipeline also removes bright diffuse emission exceeding sizes of $10'$. Therefore, only relative photometry to nearby cirrus regions should be performed with Atlas mosaics, and the achieved resolution and depth is not as uniform and deep across the field as in mosaics of single exposures, as processed and described in the previous chapter. Nevertheless, I was able to re-identify echoes found in the previous chapter and will try to search for echoes around more historic supernovae in larger fields using Atlas images.

As very bright and large infrared echoes around Cas A are also detectable on images from the Infrared Astronomical Satellite's (*IRAS*, (Neugebauer et al. 1984)) all-sky survey from the year 1983, I also compared these data with the new *WISE* images. Light echo regions should either be detected in one or the other survey or changed their position significantly. *IRAS* had a very coarse PSF of $230''$ (FWHM; compared to $6''$ for *WISE*), making this survey only sensitive to the largest and brightest infrared echoes. Mosaics from *IRAS* data were created based on the "Improved and Reprocessed *IRAS* Survey" data (IRIS, Miville-Deschênes and Lagache 2005) using the `Montage` software package as described in section 2.2.1.1.

2.3.2 Light Echo Candidate Lists

I analyzed fields around the before mentioned supernova remnants and compiled lists of possible echo candidates based on the following three criteria:

- **Color** – Infrared echoes are characterized by reddish 22/12 µm flux ratios compared to surrounding cirrus emission,
- **Morphology** – Light echoes are clustered and clumpy, possibly connected by diffuse emission of the same color,
- ***IRAS*** – Echoes likely changed position or appeared/disappeared over the 26 year time-baseline between the *WISE* and *IRAS* surveys.

It should be emphasized that I do not claim these structures to be necessarily echoes, but these are promising candidates which need further investigation to verify their echo origin, either by difference imaging from a second *WISE* epoch, or from ground based observations.

The footprints of the mosaicked Atlas images are illustrated on three color composites of *IRAS* 12, 25 and 60 µm images, above the respective light echo candidate tables. The maps are plotted on a Galactic coordinate system.

A single mosaic of Atlas images usually has a size of $11^\circ \times 11^\circ$. For the Crab nebula, an area of ~ 945 square degrees, for Tycho, SN1181 and Cas A an area of ~ 720 square degrees and for Kepler an area of 170 square degrees was analyzed. A restricting factor for the size of the fields were the limitations of the *WISE* Preliminary Data Release. In the future, larger areas may be searched with the Final Data Release.

Some very promising echo candidate regions are depicted in Figure 2.16, and can be referenced with their respective stamp number given in the last row of the Tables 2.6, 2.8 and 2.7. The radius r stated in these tables illustrates the area of interest around the center coordinates.

Table 2.6: Light Echo Candidates from the Crab Nebula

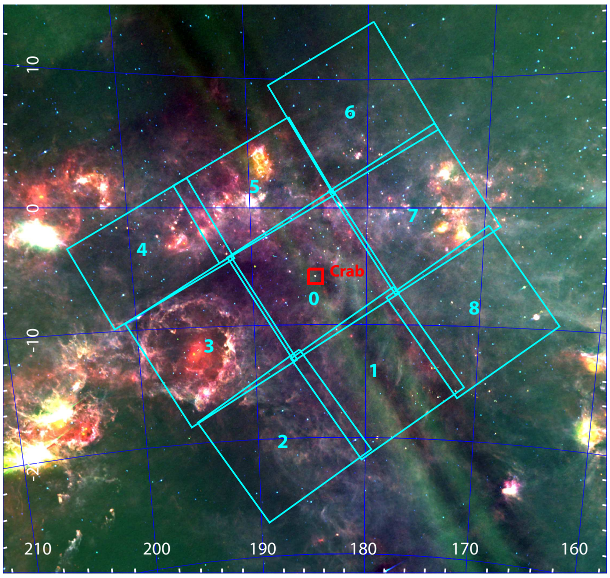

Field	Position		Properties					
	RA	DEC	r [″]	color	morph.	IRAS	remarks	stamp
0	$05^{h}33^{m}44^{s}$	$18^\circ30'54''$	3.8	✓	✓	✓	very promising	1
	$05^{h}49^{m}03^{s}$	$25^\circ33'42''$	6.7	✓		✓		
	$05^{h}49^{m}47^{s}$	$19^\circ58'01''$	6.7	✓		✓		
1	$05^{h}12^{m}11^{s}$	$34^\circ57'13''$	10.0		✓	✓	big, not det. in IRAS	
	$05^{h}12^{m}08^{s}$	$34^\circ31'03''$	1.7	✓	✓	✓	bright, not det in IRAS	
	$05^{h}13^{m}54^{s}$	$34^\circ12'08''$	6.3	✓	✓	✓	bright and long	2
	$05^{h}09^{m}30^{s}$	$37^\circ00'56''$	3.2		✓	✓	patchy filament	
2	$05^{h}02^{m}52^{s}$	$25^\circ49'34''$	2.8	✓	✓	(✓)	tiny, patch, very echo like	3
	$04^{h}30^{m}59^{s}$	$18^\circ02'27''$	5.2		✓	✓	color due to corner of FOV?	
	$04^{h}39^{m}56^{s}$	$17^\circ53'35''$	2.9	(✓)	✓	✓	bright ridge, no IRAS	
3	$05^{h}14^{m}45^{s}$	$07^\circ58'39''$	6.2	✓	✓	(✓)		4
	$04^{h}55^{m}58^{s}$	$13^\circ01'17''$	5.8	✓		✓	cloud moved wrt IRAS	
	$04^{h}59^{m}12^{s}$	$13^\circ47'25''$	5.9	✓	(✓)	✓	cloud moved wrt IRAS	
	$05^{h}01^{m}39^{s}$	$14^\circ09'29''$	4.5	✓	✓	✓		
5	$06^{h}19^{m}49^{s}$	$15^\circ24'52''$	3.0	✓	✓	✓	bright blobs	5
	$06^{h}11^{m}09^{s}$	$13^\circ23'35''$	3.1	✓	✓	✓	low likelihood, sim vicinity	
	$06^{h}06^{m}32^{s}$	$14^\circ01'59''$	2.0		✓	✓		
	$06^{h}17^{m}14^{s}$	$12^\circ57'10''$	4.4	✓	✓	✓	changed wrt IRAS	7
	$06^{h}22^{m}19^{s}$	$10^\circ35'54''$	4.0	✓	✓	✓	not in IRAS	
	$05^{h}57^{m}14^{s}$	$08^\circ43'42''$	6.7	✓		✓	drastic change wrt IRAS	
6	$06^{h}16^{m}57^{s}$	$22^\circ52'53''$	6.7	✓	✓	✓	top priority, best match	8
	$06^{h}21^{m}01^{s}$	$23^\circ55'25''$	3.0	✓	✓	✓	changed wrt IRAS	
	$06^{h}21^{m}59^{s}$	$25^\circ13'56''$	1.8	(✓)	✓	✓	changed wrt IRAS	
	$06^{h}09^{m}14^{s}$	$22^\circ06'17''$	2.7		✓	✓		
7	$06^{h}03^{m}58^{s}$	$31^\circ33'44''$	16.7	(✓)	✓	✓	very bright, not in IRAS	
	$06^{h}01^{m}24^{s}$	$31^\circ03'06''$	1.2	✓	✓	✓		
	$05^{h}56^{m}38^{s}$	$27^\circ06'54''$	6.7	✓	✓	✓	”front” moved wrt IRAS	
8	$05^{h}40^{m}54^{s}$	$30^\circ11'15''$	4.2	✓	✓	✓		
	$05^{h}30^{m}42^{s}$	$34^\circ38'09''$	4.8	✓	✓	✓		
	$05^{h}28^{m}37^{s}$	$35^\circ28'07''$	3.9		✓	✓	changed wrt IRAS	9
	$05^{h}29^{m}22^{s}$	$35^\circ07'02''$	5.2	✓	✓	✓	not in IRAS	

Table 2.7: Light Echo Candidates from Kepler

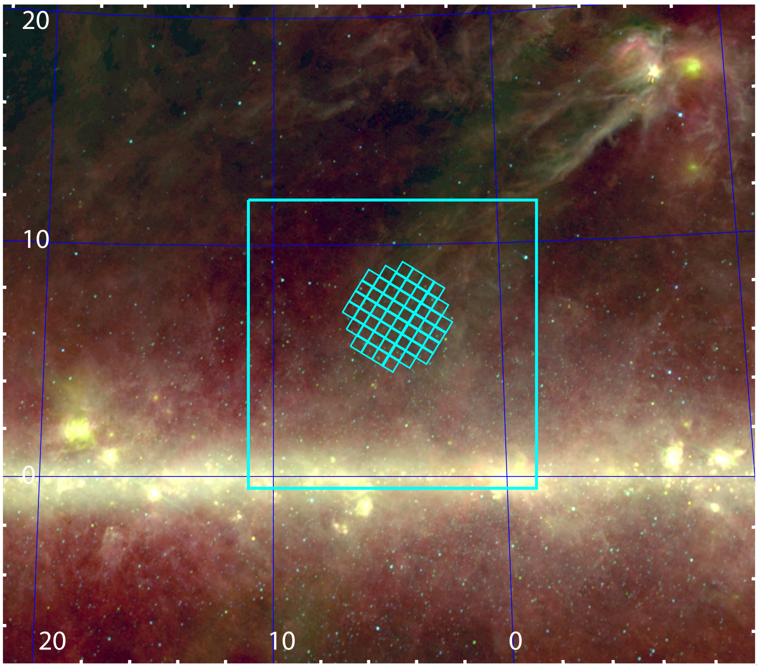

Field	Position		Properties					
	RA	DEC	r [″]	color	morph.	IRAS	remarks	stamp
	$17^{h}58^{m}16^{s}$	-17°59′18″	8.9			✓	diffuse, moved wrt IRAS	
	$17^{h}54^{m}02^{s}$	-18°46′24″	6.9	(✓)	✓	✓	interesting, bright	15
	$17^{h}51^{m}36^{s}$	-19°49′35″	5.4	✓	✓	✓	faint, no IRAS	
	$17^{h}53^{m}33^{s}$	-19°24′38″	7.1	✓	✓	(✓)	bright, very echo like	
	$17^{h}25^{m}08^{s}$	-26°43′30″	5.2	✓	✓	✓	clumpy	

Table 2.8: Light Echo Candidates from Tycho, SN1181 and Cas A

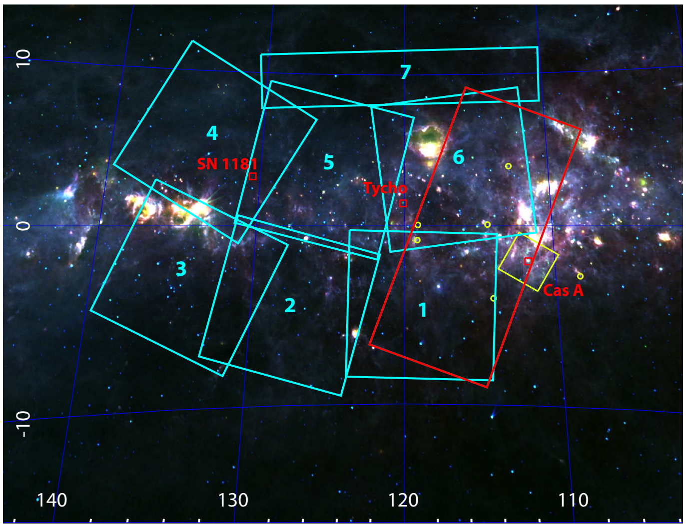

Field	Position		Properties					
	RA	DEC	r [″]	color	morph.	IRAS	remarks	stamp
1	$00^h33^m37^s$	62°06′18″	6.4	✓	✓	✓		
	$00^h39^m46^s$	61°38′10″	2.8	✓	✓	✓	very likely	10
	$00^h50^m09^s$	61°43′42″	3.2	✓	✓	✓	no emission at IRAS	
	$00^h57^m41^s$	59°53′10″	2.3	✓	✓	✓	no emission at IRAS	
	$00^h48^m31^s$	59°31′07″	5.1	✓	✓	✓	big region, no IRAS	
	$01^h02^m45^s$	58°50′13″	6.8	✓	✓	✓	faint, many	
2	$01^h39^m17^s$	60°50′37″	4.0	✓	✓	✓	bright, promising	11
3	$01^h52^m59^s$	57°54′49″	11.4	✓	✓	✓	few isolated candidates	
	$01^h32^m04^s$	63°00′30″	3.1	✓	✓	✓		
	$01^h39^m32^s$	60°45′44″	4.0		✓	✓	elongated, nothing at IRAS	
4	$01^h49^m15^s$	69°23′20″	7.0	✓		✓	too high- change, no echo	
	$01^h59^m27^s$	66°50′21″	3.2	✓	✓	✓	bright, no IRAS	
	$02^h48^m18^s$	63°03′21″	4.4	✓	✓	✓	bright elongated, no IRAS	
	$02^h13^m46^s$	69°53′21″	8.1	✓		✓	too high- change, no echo	
	$01^h57^m41^s$	61°37′26″	3.2	✓	✓	✓	bright, no IRAS,	12
5	$01^h39^m25^s$	60°46′28″	6.5	✓	✓	✓	long filament, no IRAS	
	$01^h57^m03^s$	63°57′54″	8.8	✓	✓	✓	faint, elongated, no IRAS	
	$01^h33^m30^s$	68°06′51″	5.7	✓	✓	✓	clumpy	
	$00^h40^m22^s$	67°39′40″	2.4	(✓)	✓	✓	very faint	
	$00^h40^m49^s$	66°38′26″	1.5	✓	(✓)	✓		
	$00^h53^m31^s$	65°26′42″	6.8	✓	✓	(✓)	bright, near optical echo	
	$00^h29^m29^s$	64°25′25″	6.2	✓	✓	(✓)		
	$00^h40^m15^s$	63°19′59″	5.9	✓	✓	✓	bright filament no IRAS	14
	$00^h39^m12^s$	63°40′07″	8.5	✓	✓	✓	no IRAS, promising,	13
	$00^h52^m50^s$	61°14′34″	5.5	✓	✓	✓	bright, diffuse, near echo	
	$01^h27^m05^s$	63°00′36″	3.9	✓	✓	✓	no IRAS, bright	
	$02^h00^m38^s$	61°59′54″	4.0	✓	✓	(✓)		
	$02^h01^m19^s$	61°26′49″	6.1	(✓)	✓	✓	diffuse, changed wrt IRAS	
	$01^h56^m13^s$	61°39′12″	8.5		✓	✓	changed wrt IRAS	
	$02^h06^m49^s$	64°29′41″	3.6	✓	✓	(✓)	faint	
	$02^h08^m48^s$	65°07′05″	2.5	✓	✓	(✓)	big clump	
	$01^h59^m26^s$	66°49′32″	3.3	✓	✓	✓	elongated, clumpy	
	$02^h04^m06^s$	69°01′40″	81.5	✓	✓	✓	very echo like, elongated	
6	$00^h12^m46^s$	64°40′20″	6.7	✓	✓	✓	bright, changed wrt IRAS	
7	$01^h42^m07^s$	70° 2′21″	4.7	✓	(✓)	✓	very faint	
	$02^h01^m25^s$	71°57′35″	6	✓	✓	(✓)		
	$22^h38^m21^s$	71°25′07″	2.0	✓	✓	✓	bright, not in IRAS	

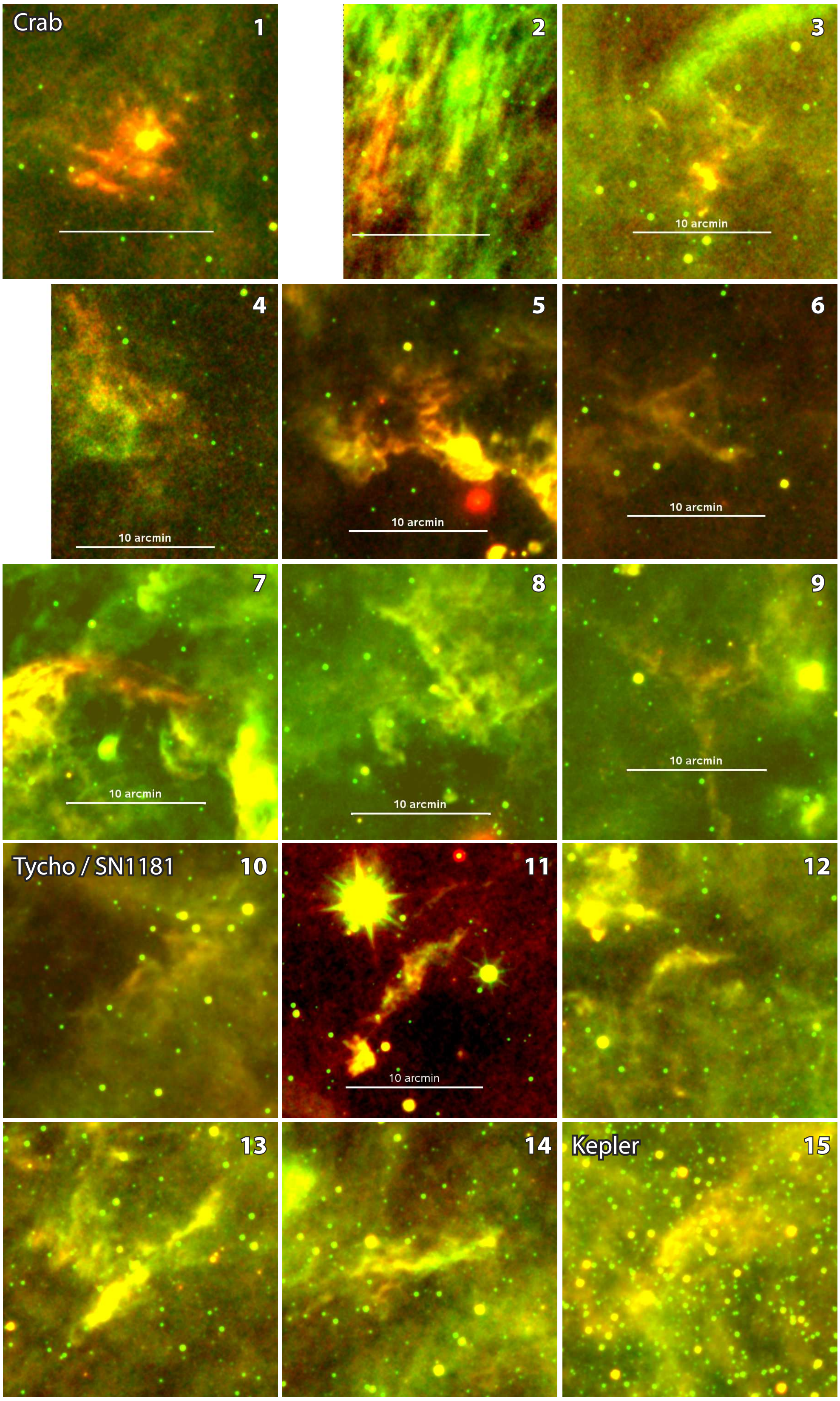

Figure 2.16: Stamps of selected echo candidates; *red*: 24 µm, *green*: 12 µm. Image size 20′ × 20′.

2.3.3 Verification of of Echo Candidates

2.3.3.1 Ground Based Surveys

Existing ground-based sky surveys were not able to confirm any echo candidates. The Sloan Digital Sky Survey (SDSS; York et al. 2000) mainly observed regions well above the Galactic plane and therefore does not cover regions with echo candidates.

Early science observations of the first Panoramic Survey Telescope and Rapid Response System prototype (Pan-STARRS PS1; Kaiser et al. 2002), lacked the sensitivity to detect any faint emission. The 30 second R-band images do not reach the necessary sensitivity (23 mag/arcsec^2) to detect light echo emission.

The upcoming Large Synoptic Survey Telescope (LSST; Ivezic et al. 2008, scheduled to be completed in $\sim$ 2014) aims for a sensitivity increase of 5 mag for single images with respect to PS1, but also visits each position on the sky in several consecutive nights per year, such that the finally achieved sensitivities are deeper by another 3-4 mag on an all-sky basis. This survey can unambiguously identify light echoes from a number of Galactic SNR, including Kepler. Unfortunately, LSST will not be able to identify light echoes around Tycho, Cas A, SN1181 and Crab, as these SNR's are located on the northern sky and not covered by the survey.

2.3.3.2 WISE All-Sky Release

As illustrated in Figure 2.9, significant areas of the sky have been observed in two epochs by *WISE*. Areas around Cas A and Tycho were observed two times using all available wavelength bands. Due to the early cryogen exhaustion on *WISE*, regions around Kepler and the Crab Nebula have not been observed by *WISE* for a second time in all bands. However, data at 3.4 and 4.6 µm was acquired for these areas, but is not released for the general public in imaging formats, as it is exclusively used by NEOWISE (Mainzer et al. 2011). It should be tried to establish a collaboration with the NEOWISE team in the future to gain access to this data, as the difference image technique could reveal light echoes from these bands despite crowding by field stars.

A quick look at the recently released all-sky release[7] confirmed the echo nature of the most distant echo from Cas A (marked "T" in Table 2.5), which I identified based on its color and morphology properties from the preliminary data release (see Figure 2.17). Within six month between the two epochs, different parts of the echoing cloud are illuminated. The emission peak shifted by about 10$''$.

This observation validates my proposed technique to identify infrared echoes based on their 22/12 µm flux ratios, as proposed in chapter 2.2. As this method was also applied to generate the here presented candidate lists, these regions should be reanalyzed based on the reprocessed Final Data Release images to either confirm the echo nature from available difference images or via new pointed observations from ground based telescopes with high sensitivity.

---

[7] Released on March 15th 2012; http://irsa.ipac.caltech.edu/applications/wise/

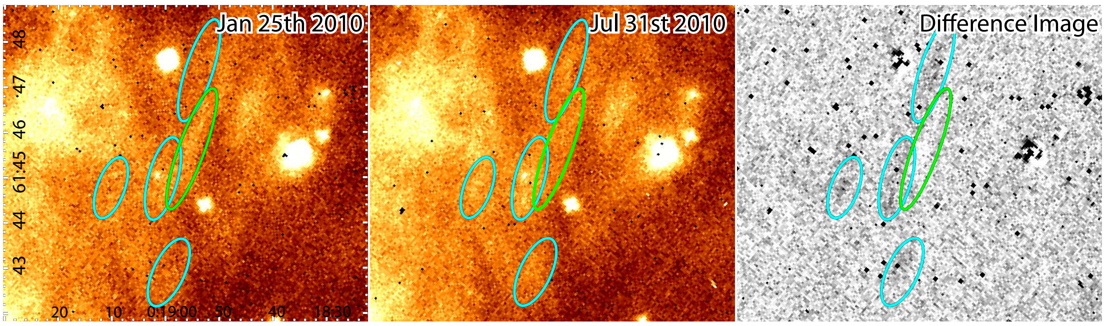

Figure 2.17: Single exposures from two *WISE* epochs toward echo ”T” of Cas A and the corresponding difference image (no image processing has been applied). Echoes from the first epoch are encircled in green, and echoes from the second epoch in cyan.

3 Light Echoes Reveal the Turbulent Interstellar Medium

Multi epoch Spitzer images of infrared echoes around the Cas A supernova remnant provide direct tomographic views of dusty material in its vicinity. With the help of high-resolution optical scattered light images, I am able to associate the infrared echoing material with the densest cusps of diffuse cold interstellar material. Comparison with theoretical studies show striking similarities with the proposed self-similar fractal structure of the ISM and its underlying turbulent movements, covering a considerable span of spatial sizes from more than 200 pc *down to* $\sim 2000\,AU$ *and densities of several* $10^3\,cm^{-3}$.

3.1 Observations and Data Reduction

After the first discovery of fast moving "knots and blobs" of infrared emission structures around Cassiopeia A by Hines et al. (2004), an extensive monitoring program was carried out in the following years. Krause et al. (2005) identified these structures as infrared echoes from the Cas A supernova explosion. With the Multiband Imaging Photometer for *Spitzer* (MIPS; Rieke et al. 2004) a roughly $3° \times 3°$ field was observed every year and regions with especially high activity were observed at an intermediate interval of about half a year until 2008 (PIDs: 233, 20381, 30571; PIs: G.Rieke, O.Krause). MIPS observations were reduced using the MIPS Data Analysis Tool (DAT; Gordon et al. 2005), starting at the RAW data product level.

Figure 3.1 shows such a 24 µm image. In comparison to the other epochs at a time interval of 6 month, it shows moving structures across the entire field of view. Individual features exhibit apparent motions of 10-20 arcsec per year, roughly the speed of light at the source distance of 3.4 kpc. Beside their apparent motions, the fine filaments and knots stand out clearly against the more diffuse cirrus emission around the remnant.

Using those monitoring observations, a particularly bright source was detected at the location RA: $23^h21^m40^s$, Dec: $+59°34'25''$. Figure 3.2 shows its evolution at 24 µm over a time period of 3 years. It is located at an angular distance of 47.6 arcmin away from the optical expansion center of Cas A. Although the source is already visible in the first epoch of observations, it changes its morphology, brightness and position drastically within just a few months time. In early 2006, it appears that most emission comes from three point like sources, suggesting that the real echoing structure is still

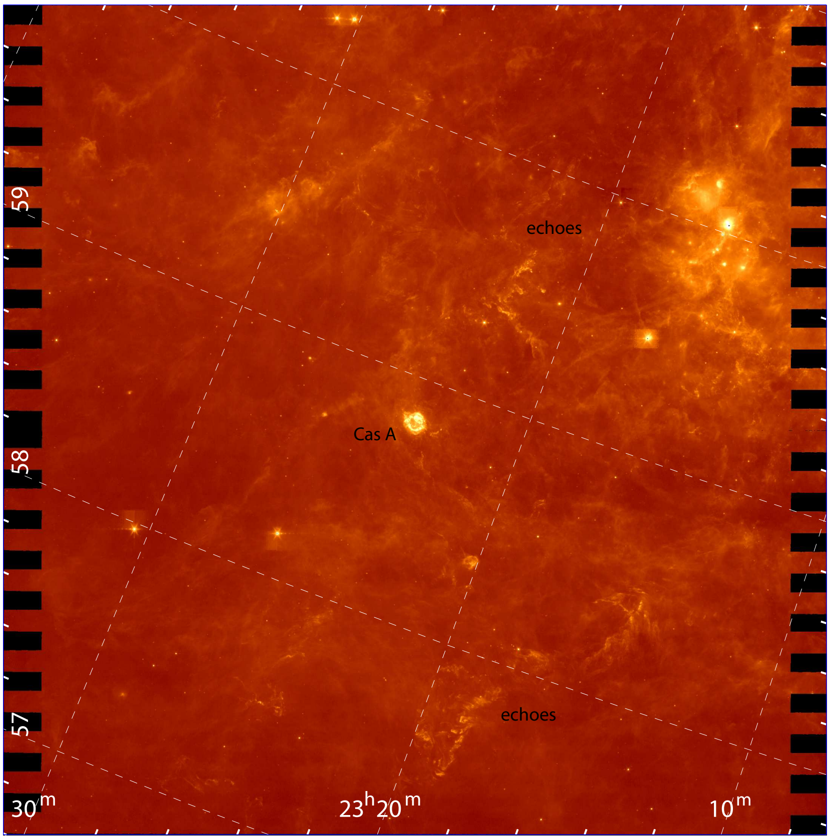

Figure 3.1: *Spitzer* MIPS 24 µm monitoring observation from January 26th 2006. Logarithmic scaling has been applied to show low surface brightness cirrus regions (~ 18 MJy/sr) and bright regions with more than 1500 MJy/sr in the Cas A supernova remnant (center). The size of the image is 3° × 3°.

unresolved with *Spitzer*. The emission diminishes very quickly between February and October 2006 indicating that the SN light beam swept past a probably very well defined end of the echo region.

On January 29th 2006, a low-resolution spectrum of this bright echoing source was obtained with the Infrared Spectrograph (IRS; Houck et al. 2004) as part of program (PID) 20381 (PI: O. Krause). A 24 µm aerial image of the echoing source is shown in Figure 3.3, with an overlay of the IRS red peak-up insert (rectangle) as well as the spectroscopic slit positions; 1× Long-Low (LL) and 3× Short-Low (SL). The red peak-up functionality of IRS was used to achieve the best possible centering of the slits on this fast moving echo-feature.

The S18.7.0 version of the Basic Calibrated Data (BCD) products from the *Spitzer* Science Center (SSC) pipeline were fed into SMART (Higdon et al. 2004; Lebouteiller et al. 2010) for final reduction. Depending on the used module, total exposure times ranged between 120s and 300s. One spectra was extracted for each of the two brightest point-like sources. They were averaged separately and combined later. A background was estimated based on the non-echo-contaminated parts of either the off-source order or the individual slits (contamination is easily evident on the MIPS 24 µm image for one

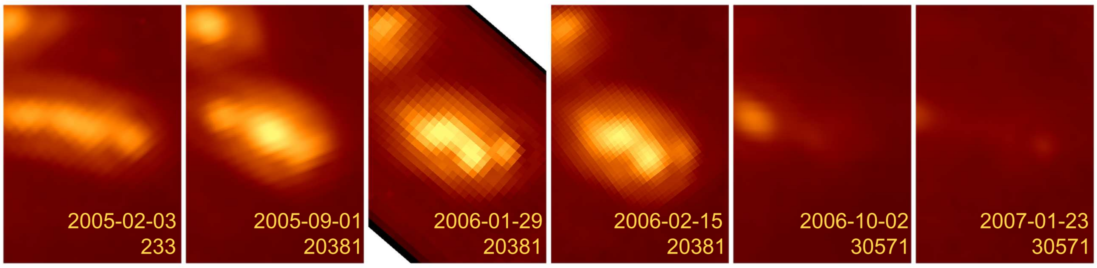

Figure 3.2: Time evolution of a bright echoing structure. Observation date and *Spitzer* Program Identification (PID) are imprinted in each panel. All observations are MIPS 24 µm images, except for an IRS red-peakup image (18.5 − 26 µm) on 2006 January 29. Each panel is displayed in logarithmic scale, with North up and East towards the left. The center is at RA $23^{\mathrm{h}}21^{\mathrm{m}}40^{\mathrm{s}}$, Dec $+59°34'25''$. The field of view is $51'' \times 69''$.

end of the LL slit). As the SL and LL modules cover slightly different special regions of the echoing source the resulting spectra were scaled to match each other's continuum levels. Absolute calibration was verified by comparing the integrated IRS flux and the measured 24 µm photometry.

In addition to space-based infrared observations, various ground based visible and near-infrared images from various 2 to 8 m telescopes exist. These images show the scattered light echo, not the thermal infrared radiation of the echoing dust. Since they were mainly obtained for the positional identification of the scattered light echo to perform spectroscopy of the supernova explosion, no exact calibration is available. Determining dust properties from infrared observations greatly simplifies the situation compared the visible observations anyhow, since interstellar extinction in the mid infrared is negligible. Observations in visible light suffer from mostly unknown extinction values along the line of sight and the reddening due to the differential scattering crossection. Therefor I use these observations mostly for morphological comparisons.

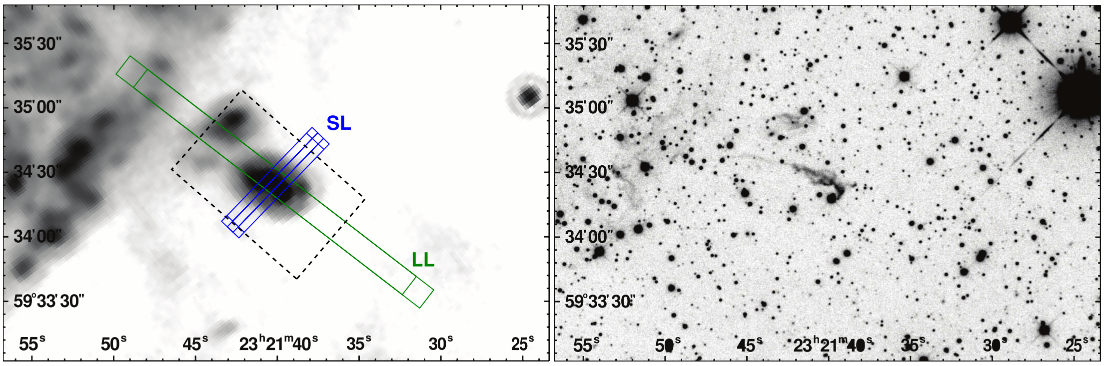

Figure 3.3: *Left*: 24 µm image of the echoing source with IRS red-peakup insert (dashed rectangle) and footprints of the Long-Low (LL, green) and Short-Low (SL, blue) spectroscopic slits positions. *Right*: The Omega2000 K_s-Band image reveals small scale clumpy and filamentary substructure.

3.2 Probing Interstellar Dust with Infrared Echoes

The following section is a brief summary of the results from our analysis of the infrared spectrum of the bright echo described above. I refer the reader to Vogt et al. (2012) for a detailed discussion.

Light echoes around Cassiopeia A represent a well defined experimental setup to probe the dust content of echoing clouds. The position of the clouds in space with respect to Cas A is well defined by the light echo geometry. Furthermore, the supernova explosion from Cas A was characterized with a spectrum from a scattered light echo by Krause et al. (2008a) and is similar to SN1993J, whose well studied light curves and spectral energy distribution can be used as a radiation template responsible for the echo emission.

A dust simulation program by K. Dullemond was modified in a way to account for this light echo geometry and irradiation characteristic, so that the spectral output could be calculated for a certain dust mix. The dust model contained a mix of PAHs, stochastically heated carbon and silicate grains, as well as thermal graphite and silicate grains, mainly based on the Li and Draine (2001) and Draine and Li (2007) models. It allowed particles in the range from 3.5 Å to 6000 Å.

Results from the Study

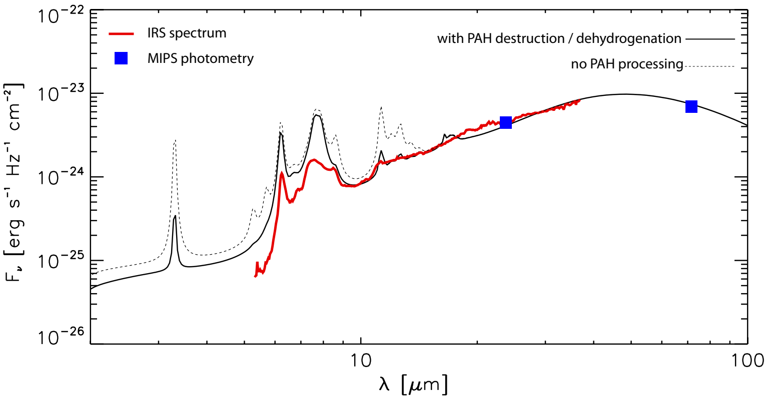

Figure 3.4: Extracted IRS spectrum and MIPS photometry of the echo region shown in Figure 3.3 and the modeled spectral energy distributions. Figure based from Vogt et al. (2012).

The recored IRS spectrum and the simulated spectral energy distribution are shown in Figure 3.4. Generally the infrared echo features a steeply rising SED towards longer wavelength and peaks beyond 24 µm, corresponding to dust temperatures lower than ~ 100 K.

The echo is the result of the UV and optical components of the supernova radiation field. In the 5 to 38 µm spectral range, the UV burst makes up $\sim 83\%$ of the total luminosity. The influence of the optical component rises at longer wavelength.

To fit the spectrum below 15 µm, about 50% of all PAHs smaller than 300 atoms and all PAHs smaller than 80 atoms had to be removed. This is probably the result of the photodissoziation by UV photons from the supernova UV burst. The weak PAH features in the 11 µm region require a dehydrogenation ratio of $\sim 80\%$ for all PAHs.

The dust simulation also determines a dust mass responsible for the observed emission under the consideration of the light echo characteristics. I use this estimate as an input for the upcoming density field comparison.

3.3 Multiphase ISM simulations

Neutral atomic hydrogen (HI) is the main constituent of the Interstellar Medium (ISM), and it is commonly believed that molecular clouds form through condensation of HI gas. As molecular clouds present the birth places for new stars, it is crucial to study the dynamics of interstellar gas to understand molecular cloud formation and therefore the initial conditions for star formation processes. Line-of-sight observations of interstellar gas (Heiles and Troland 2003, 2005) reveal a complex multi-phase structure, in which cold and dense structures (CNM) are embedded into a warm and diffuse phase (WNM). Both phases are approximately in pressure equilibrium, as early models by Field et al. (1969) predicted. The observations also show that this multi-phase medium is strongly turbulent, as revealed by the occupation of the traditional "unstable"-phase regime in the pressure-density diagram and a broad range of observed HI spin temperatures (Dickey et al. 1977)

In an attempt to understand the dynamic formation processes of this turbulent multiphase medium, Hennebelle and Audit (2007) developed a numerical simulation to model the effect of colliding turbulent WNM flows. The simulation is performed in a two-dimensional box, which is initially filled with a uniform WNM, consisting of an ideal gas with a density of $n_{\mathrm{WNM}} = 0.8\,\mathrm{cm}^{-3}$ and a mean weight $\mu = 1.4\,m_H$ (where m_H is the mass of a hydrogen atom; the factor 1.4 takes additional helium abundance into account). A converging flow of WNM gas is injected from the left and right side of the box with a speed of 1.5× the sound speed in the medium, modulated by a some random turbulent fluctuations. Gas is allowed to leave the box at the bottom and top sides. For each consecutive time-step, the Euler equations from classical fluid hydrodynamics, with an added cooling function $\mathcal{L}$ and thermal conductivity κ in the energy conservation equation, are solved

$$\frac{\partial \rho}{\partial t} + \nabla \cdot (\rho \mathbf{u}) = 0, \tag{3.1}$$

$$\frac{\partial \rho \mathbf{u}}{\partial t} + \nabla \cdot (\mathbf{u} \otimes (\rho \mathbf{u})) + \nabla P = \mathbf{0}, \tag{3.2}$$

$$\frac{\partial E}{\partial t} + \nabla \cdot [\mathbf{u}(E + P)] = \mathcal{L}(\rho, T) + \nabla \cdot [\kappa(T) \nabla \cdot T], \tag{3.3}$$

where ρ is the mass density, $\mathbf{u}$ the velocity field, P the pressure, T the temperature and E the total energy. $\mathcal{L}$ considers cooling by fine-structure lines (CII and OI), Ly-α emission, electron recombination on charged dust grains and heating by the photo-effect on dust grains due to UV radiation.

The Hennebelle & Audit simulation covers a huge span of sizes. With a box size of $20 \times 20\,\mathrm{pc}^2$, covered by $10\,000^2$ cells, a spatial resolution of 2×10^{-3} pc is achieved. This is reasonably good to resolve both the largest and smallest scales important to thermal condensation of HI gas.

The cooling length of the WNM is defined as the product of the cooling time and the sound speed and corresponds to size ranges of 3–10 pc. The typical fragment size of CNM structures is determined by the cooling length and the density contrast $\zeta \approx 100$ between the CNM and WNM fragments and is about 0.1 pc. The size of the thermal front between the phases is the "Field" length, $10^{-1} - 10^{-3}$ pc for WNM and CNM structures and the size of shocked CNM fragments is given by (fragment Size / Mach number^2) = 10^{-3} pc.

The fragment size and Field length are well resolved, but not the size of shocked fragments, thus the simulation underestimates the densities for fragments undergoing supersonic collisions.

The resulting density field of the simulation run is shown in Figure 3.5 at a time of $t = 26.82$ Myr after the beginning of the simulation. After about 5 to 15 Myr, the simulation reaches a permanent regime, where the statistical properties and the mass fraction in the different phases do not change anymore.

Results from the Hennebelle & Audit Study

The simulation shows that the cold neutral phase of the ISM naturally condenses out of an initially uniformly distributed turbulent WNM flow. Upon the collision of the two flows, a high pressure layer with two accretion shocks is formed. Trapped gas inside these layers becomes thermally unstable and can condense into cold gas, forming CNM fragments. The structure of the medium is rather complex, and the CNM is fragmented into many long lived structures and is interwoven with the warm phase. Typical CNM structures have a density of about $100\,\mathrm{cm}^{-3}$ and sizes of a few thousand AUs. These fragments are connected to each other by filaments of lower density ($\sim 10\,\mathrm{cm}^{-3}$). Such filaments occupy the thermally unstable regime in the pressure-density diagram, and are temporarily (few Myr's) stabilized by the turbulent flow. With increasing turbulence, more gas is found in this unstable regime and CNM fragments need more time to reach pressure equilibrium with the surrounding WNM. CNM fragments are generally not very far from pressure equilibrium with the surrounding WNM.

Large density fluctuation can be seen for CNM fragments, spanning over three orders of magnitude. The highest density cusps are produced by supersonic collisions between CNM fragments. These shocked regions are located at the interface between high-pressure WNM and low-pressure CNM clouds and can reach densities in excess of $10^4\,\mathrm{cm}^{-3}$. Yet, the sizes of these regions are very small and are likely lower than the resolution limit of the simulation (~ 400 AU). Such small scale, high-density structures have also been inferred observationally by Dieter et al. (1979) and others. These so called Tiny Scale Atomic Structures (TSAS), seen in absorption towards nearly all radio continuum sources, are characterized by high densities (up to $10^5\,\mathrm{cm}^{-3}$) and very small scales (several 10 AU's). Supersonic CNM collisions probably provide a viable mechanism for the formation of such features. The overall filling factor of gas denser than $10^3\,\mathrm{cm}^{-3}$ is about 1–3 %, whereas the majority of the medium is filled with low-density WNM ($\bar{n} = 0.8\,\mathrm{cm}^{-3}$).

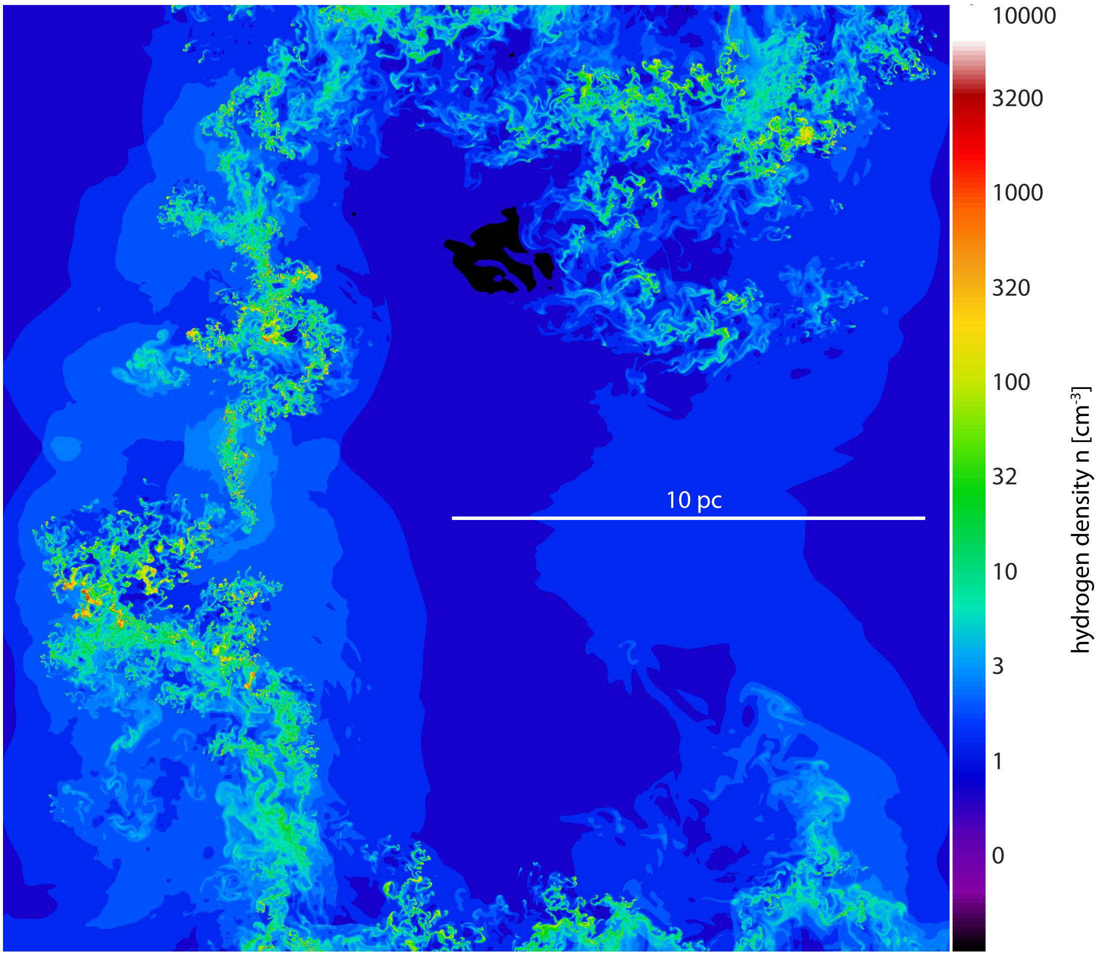

Figure 3.5: Original density field of the Hennebelle & Audit (2007) ISM simulation at time $t = 26.82\,\mathrm{Myr}$. The box has a size of 20 pc with $10\,000^2$ cells, corresponding to a spatial resolution of 2×10^{-3} pc.

A New Observational Approach

The interplay between different ISM phases and interstellar turbulence has been well studied by HI and other radio observations. However, theses methods only provide information on the physical parameters along a special line of sight (TSAS, for example, are inferred from absorption studies towards strong radio continuum sources, like quasars). In this study I want to present the first direct mapping observations and comparisons with high-resolution simulations of parts of the interstellar medium in the vicinity of Cassiopeia A, by observations of supernova light echoes.

Under the assumption of a certain dust-to-gas ratio, the interstellar gas is traced by the thermal emission of dust responsible for light echoes. *Spitzer*-MIPS monitoring of light echoes covered physical scales from 200 pc down to the resolution limit of 0.1 pc. With the additional use of high-resolution optical images from up to 8 m class telescopes, resolutions of about 2 000 AU have been achieved. While the individual *Spitzer* and optical images of echoes give a 2D "snap-shot" of ISM structures located on the light echo ellipsoid, the three year time span of *Spitzer* monitoring provides a spatial depth along the line of sight between 1.5 and 3.3 lightyears, thus probing a total volume of several $10^4\,\mathrm{pc}^3$.

In this exploratory study I want to compare the observed morphologies of infrared and optical light echoes with the 2D multiphase ISM simulations by Hennebelle and Audit (2007).

3.4 Density of Echoing Material

In order to compare echo observations with ISM simulations, a common comparative parameter has to be found. Infrared emission from dust is proportional to the emitting dust mass. This fact has been used in the study presented in section 3.2 to derive a dust mass estimate for a certain echo. P. Hennebelle kindly provided the computed density field of his multiphase ISM simulations. It is therefore tempting to derive a density field from the infrared observations, using the dust-mass estimate and the spatial extend of the echo regions, for direct comparison

To estimate the density of the echoing material it is necessary to determine the volume which gives rise to the observed dust emission. A schematic view of an echo region is given in Figure 3.6. Parts of the two light echo ellipsoids, at the beginning time t_0 and end time t_1 of the radiation event, are drawn in blue. Due to the finite illumination time $t_1 - t_0$ of the dust cloud, an observer will simultaneously receive emission originating from a volume element with thickness L_{burst} at any time:

$$L_{burst} = x_0 - x_1, \tag{3.4}$$

where x_i denote the distances to the light echo ellipsoids at the times t_i (see Figure 1.6 and 3.6).

The spatial extend of the echo on the sky, in the direction ($L_{sky,||}$) and perpendicular ($L_{sky,\perp}$) to the radiation burst origin, are observables. $L_{sky,\perp}$ points into the drawing plane in the figure. In this study, only echoes in the Galactic interstellar medium are considered and thus, the distances r_i and x_i are much larger than the on-sky extend of the echoing region. For simplification, the excited volume can be approximated as a parallelepiped, as the local curvature of the ellipsoid can be neglected in this case. The base of the parallelepiped is defined as:

$$L_0 = \frac{L_{sky,||}}{\cos\left(\frac{\beta}{2}\right)}. \tag{3.5}$$

With these quantities it is now possible to calculate the volume of the echoing region

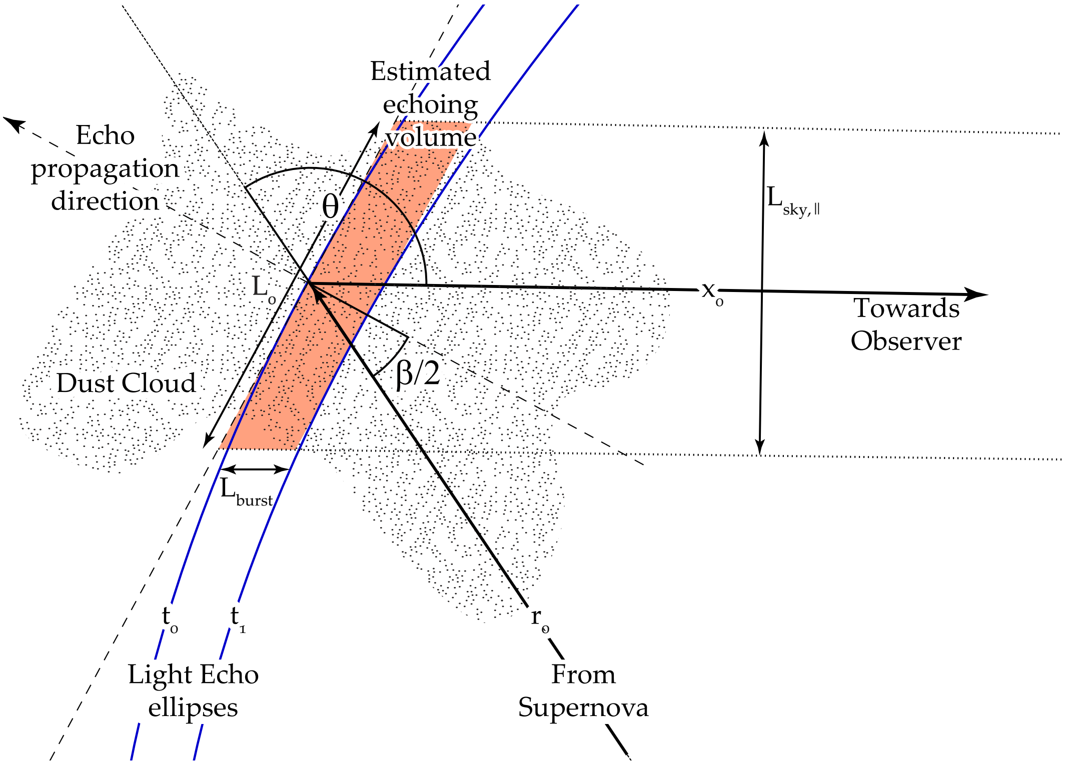

Figure 3.6: Geometrical sketch of an echoing region. Parts of the two light echo ellipsoids, which enclose the illumination duration of the outburst between the times t_0 and t_1, are drawn in blue. The red area marks the volume of the parallelepiped used to approximate the volume between the ellipsoids responsible for echo emission. As ISM structures are inhomogeneous and clumpy, the estimated volume of emitting dust is an upper limit.

V_{echo}, as seen from an observer on earth at any given time:

$$\begin{aligned} V_{echo} &= L_{burst} \times L_0 \times \sin(\theta/2) \times L_\perp \\ &= L_{burst} \times L_0 \times \sin\left(\frac{180^\circ - \beta}{2}\right) \times L_\perp \\ &= L_{burst} \times \frac{L_{sky,||}}{\cos\left(\frac{\beta}{2}\right)} \times \cos\left(\frac{\beta}{2}\right) \times L_\perp \\ &= L_{burst} \times L_{sky,||} \times L_\perp . \end{aligned} \tag{3.6}$$

Thus, the estimation of the emitting echo volume only depends on the on-sky extend of the regions perpendicular and parallel to the direction of the supernova and the line-of-sight thickness L_{burst}, induced by the illumination duration.

However, the illumination duration is not strictly defined. Light curves of supernovae vary substantially over time. For a core-collapse supernova, a short and intense UV-radiation burst by the shock heating of the thin envelope is followed by a longer optical light peak induced by the radioactive decay of ^{56}Co. Since faint flux levels contribute less to the echo emission than the initial bright bursts, one can approximate the illumination duration by an "effective width" or the time it takes to vary the flux level by 2 mag (Sugerman 2003). In the case of light echoes around Cassiopeia A, which was similar to the Type IIb explosion of SN1993J (Krause et al. 2008a), the UV radiation phase and the optical phase can be approximated by an effective time of 2.5 days and 25 days, respectively (Blinnikov et al. 1998; Richmond et al. 1994).

These two phases follow each other and are both responsible for the infrared emission as inferred by our dust content analysis of the echo in Vogt et al. (2012). To calculate the effective burst length, one can simply add the contributions of two consecutive parallelepipedes with the length L_{UV} and L_{opt}. For the echo at position RA: $23^{\mathrm{h}}21^{\mathrm{m}}40^{\mathrm{s}}$, Dec: $+59°34'25''$ on January 29th 2006, presented in Figure 3.2, and the general estimate of Cas A's explosion date in 1681 (Fesen et al. 2006) at a distance of 3.4 kpc, the physical parameters are

$$\begin{aligned} L_{UV} &= 1.51\,\text{light days} \\ L_{opt} &= 15.1\,\text{light days} \\ L_{sky} &= 0.0167\,\text{pc/arcsec} = 19.9\,\text{light days/arcsec} \\ V_{echo} &= 1.14 \times 10^{50}\,\text{cm}^3\text{arcsec}^{-2} \end{aligned}$$

The main source of uncertainty in the volume estimation arises from estimating the illumination duration. While adopting an effective width, which covers the entire supernova luminosity or adopting a flux density fall-off threshold (e.g. a drop of 2 or 3 mag), can yield to illumination durations higher or lower by a factor of ~ 3 (see Sugerman 2003). Additionally, observed supernova light curves never measured the extremely intense initial shock breakout flash, which only lasts between 1 and 2 000 seconds, but features a luminosity up to 5 orders of magnitude higher than the levels observed in the first few days of the UV-radiation burst (for example Tominaga et al. 2011). Its influence to light echoes has not been analyzed yet, but may be significant in terms of providing a much shorter illumination flash. A much more precise theoretical analysis of the light-curve to light-echo relationship would be needed here. Hence, the estimated volume and the derived absolute densities should only be considered as a "order-of-magnitude" analysis. It is worth noting that this approach does not influence the ability to perform relative measurements and morphological comparisons, as long as the respective models and approaches are used consistently.

To estimate the actual density of the echoing material, the output of the echo simulation is used. For a total MIPS 24 µm flux of 0.447 Jy, a dust mass of 7×10^{29} g was derived for an echo at a distance of 3450 pc. The used dust model (Li and Draine 2001) implies a dust-mass to hydrogen nucleon ratio of $m_{\mathrm{H,dust}} = 1.89 \times 10^{-26}\,\mathrm{g\,H^{-1}}$. Thus, for every 1 Jy at 24 µm, a total number of 8.3×10^{55} hydrogen nucleons can be assumed. The use of alternate dust models could change these values again by a factor of $\pm \sim 3$, but these numbers are consistent with the echo modeling done by Vogt et al. (2012), and differences are beyond the scope of this analysis.

Interstellar clouds are very inhomogeneous and clumpy and it is unlikely that the entire volume of the parallelepipeds is filled by dust. As a result, the estimated cloud-densities are *lower* limits. This effect might be small compared to the order-magnitude consideration, but it should be recognizable when using higher resolution images, and thus resolving smaller structures.

3.5 Morphological Comparison of Observation and Simulation

In order to perform a morphological comparison with the various observations, the density field of the simulation is convolved with a Gaussian to mimic the resolution characteristics of the instrument. To compare with *Spitzer*-MIPS observations, the simulated density field was smoothed to a spatial resolution of $6.5''$, corresponding to a physical resolution of 0.11 pc at the distance of the echoes. For comparison with various scattered light echo observations, the simulation was smoothed to the respective actual seeing values, under which the observations were performed.

3.5.1 Size Scales 20 pc to 0.2 pc

The largest scale suitable for direct comparison is set by the box-size of the ISM simulation. At a distance of 3450 pc towards an echoing region, this corresponds to an on-sky area of $\approx 20'$. A field of this size with bright echo emission was extracted from

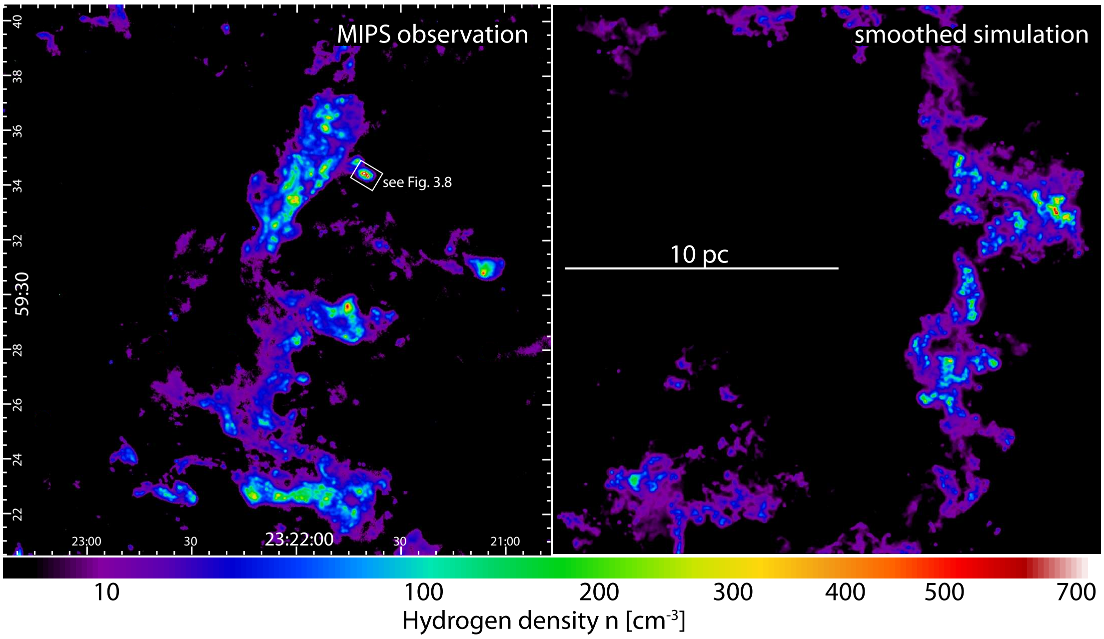

Figure 3.7: (*Left*): *Spitzer*-MIPS 24 µm $20 \times 20\,\mathrm{pc}^2$ field, with emission from infrared echoing clouds visible around Cas A. Intensity units are scaled to density levels depicted in the colorbar. (*Right*): Smoothed density field of the ISM simulation. The original density field has been convolved with a Gaussian leading to the same spatial resolution as the MIPS observations (0.11 pc).

Spitzer monitoring observations and is presented in Figure 3.7. Due to *Spitzer*'s PSF size, the finest achieved spatial resolution corresponds to 0.11 pc.

A first visual comparison of the ISM simulation and the echo observation reveals many similarities. The inferred densities for light echoes is on the order of 10 to 1000 cm^{-3}. This density regime is occupied by the cold neutral medium phase in the simulations. In fact, the overall size scales of echoes resembles the size scales of the CNM structures in the simulation. Most parts of the $20 \times 20\,\mathrm{pc}^2$ field are void of echo emission. Similarly, the simulation mainly contains the warm neutral phase. With the chosen colormap in the image, this is manifested by mainly black WNM (simulation) and black regions with no detected emission (observation). In turn, it means echoes trace CNM structures exclusively.

If CNM structures arise from the collisions of converging WNM flows, the emerging structures would be compressed and feature rather elongated structures. In this case the turbulent flow field would ensure a mixing of WNM and CNM structures, which means that some WNM is still present in the CNM phase. Thus the CNM would appear fragmented. Some very dense CNM structures could also "decouple" from larger sized CNM region and move, stabilized by the turbulent field, through the WNM.

Similar things are seen in the observed echo field. Light echoes are clustered to each other. An ensemble of several echoes builds a general CNM cloud within the converging WNM flow. The edges of such a cloud are rather sharp (density contrast > 10), which is similar to the simulation. The average thickness of the echoing cloud seen in the upper part of the image is ~ 2.7 pc, while the transverse length is about 7 pc. This corresponds to an aspect ratio of ≈ 0.4, which is also typical for the structures in the lower region of the image. The simulated density field is characterized by a mean aspect ratios 0.4–0.6 for larger sized cloud structures. On smaller scales, the bulk of echo emission arises from unresolved point sources, similar to the expected fragments in the turbulent flow field, enclosed by faint extended emission. The faint extended emission could arise from the simulated filaments of intermediate density, by which the densest CNM structures are connected in the simulated field.

Some dense decoupled echoes are also visible just outside of bigger CNM structures. Such a region will be analyzed in the next section by higher resolution images from ground based telescopes.

3.5.2 Size Scales 0.2 pc to 2 000 AU

In December 2005, a K_S-band image of the echo described in section 3.2 was acquired with Omega2000 on the 3.5 m telescope in Calar Alto. The seeing conditions allowed a spatial resolution of 0.013 pc, or about 2700 AU. *Spitzer*-MIPS 24 µm images of the same echo structure from October 2005, January 2006 and February 2006 each show the same total flux of about 0.45 Jy. By assuming that the mass responsible for the 24 µm emission, originates from the same structures seen in the K_S-band image, it is possible to calculate a density field based on the intesity distribution in the higher-resolution K_S-image. With the increased resolution (0.013 pc vs. 0.11 pc for MIPS), it is possible to track the density field more accurate, by resolving a higher number of underlying structures. This Omega2000–density field is shown in Figure 3.8.

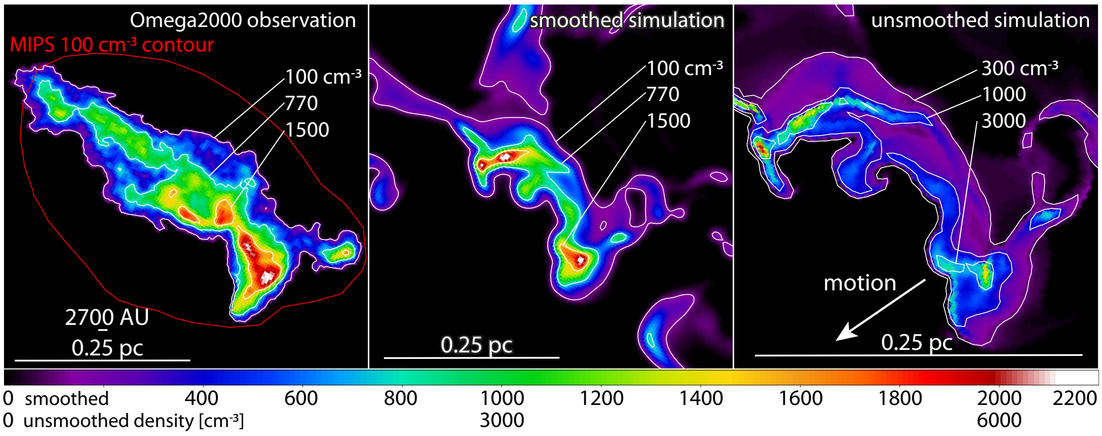

Figure 3.8: Zoom into a very dense echoing region at RA: $23^{\mathrm{h}}21^{\mathrm{m}}40^{\mathrm{s}}$, Dec: $+59°34'25''$. (*Left*): The Omega2000 K_S-band intensity distribution was used to derive the gas density field of the echoing cloud based on the dust-mass estimate from *Spitzer*. The resolution of the Omega2000 image corresponds to a physical scales of 2700 AU at the distance of the echo. (*Middle*): A cold neutral medium feature for comparison from the ISM simulation (smoothed to the corresponding resolution of Omega2000). (*Right*): Zoom-in on the unsmoothed representation of the cold neutral medium fragment. Due to the higher spatial resolution, higher densities are revealed (bottom numerics in color bar).

Due to the higher spatial resolution, the inferred maximum densities are higher (up to $\sim 2000\,\mathrm{cm}^{-3}$), than inferred from MIPS 24 µm images (up to $\sim 800\,\mathrm{cm}^{-3}$). The area is not filled completely, since a very elongated structure is responsible for the "extended compact" emission seen with *Spitzer*. The overall length of the structure (at a density threshold of $100\,\mathrm{cm}^{-3}$) is about 0.5 pc, while its thickness is approximately 0.1 pc. This very small aspect ratio (0.2) is mostly seen in shocked CNM structures in the Hennebelle & Audit simulation.

These echo region is further structured into several sub-clumps down to the resolution limit of 2700 AU. The brightest structures have an average density of more than $1800\,\mathrm{cm}^{-3}$ (within the resolution limit) and a similar aspect ratio (≈ 0.2) than the overall cloud. The individual clumps are connected to each other by lower density ridges.

A similar looking feature was found in the CNM part of the smoothed ISM simulation and is shown in Figure 3.8, alongside with the unsmoothed density field. The smoothed field shares the same overall characteristics (density, fragmentation and elongation) with the observed echo.

As expected, the underlying unsmoothed density field shows even higher densities by a factor of at least three. Due to convolution to a coarser spatial resolution, these sub-structures were unresolved in the smoothed field. Several very elongated (aspect ratio < 0.3) clumps with densities $> 5500\,\mathrm{cm}^{-3}$ are embedded in a $400\,\mathrm{cm}^{-3}$ substance (violet color). The entire cloud has a sharp border towards much lower densities of less than $5\,\mathrm{cm}^{-3}$ (black). The dense clumps are connected by filaments of intermediate density (1500 cm^{-3}). It can be noted that all dense fragments are located very close (0.008 pc $\cong$ 1650 AU) to the lower border (8 o'clock direction) of the WNM phase. This is an imprint of their creation process by shocks and indicates the velocity vector of the impinging WNM flow (or the movement of the cloud as seen from the initial system of the WNM). This is reminiscent of a "bow-shock" like shape, which indicates the overall velocity vector (this special region thus moves towards the bottom of the image). A similar pattern can be detected in the echo observation, where the density contours are twice as close to each other on the lower side of the image than on the upper side.

The temporal evolution of this echoing region was also imaged by *Spitzer* from 2005 till 2008 (see Figure 3.2). These observations probe the depth of the echo as the supernova light beam traverses through the structure. The echo is already visible in the first epoch of observations (February 2005) and already seems to consist of an elongated agglomeration of unresolved point sources. This appearance does not change much, until the echo emission diminishes very quickly between February and October 2005, indicative that the light beam swept past a probably very well defined end of the echo region. On physical scales it means the echoing cloud is rather sheet-like with dimensions of approximately $0.5\,\mathrm{pc} \times (> 0.3)\,\mathrm{pc} \times (< 0.1)\,\mathrm{pc}$.

A Tycho Light Echo

To test the universality of the above statements, a vast range of different echoing regions should be compared. On October 8th 2008, a spectroscopic analysis of the scattered light from an echo around Tycho's supernova was performed with the 8 m Subaru telescope. The 180 sec acquisition image from FOCAS has a similar angular resolution and depth as the other observations of light echoes around Cassiopeia A, thus making an comparative analysis possible. As no infrared observation or any other calibration is available, a mass and density estimate can not be made. Only a morphological comparison is possible for this echo around Tycho. At a distance of 3530 pc to the echo and a delay time of 440 years, a spatial resolution of about 2500 AU is achieved. The R-band image is shown in Figure 3.9.

The echoing region is elongated. At an overall length of more than 2 pc, it has an average width of only 0.16 pc, yielding an aspect ratio of 0.08. At smaller scales, the region breaks down into several substructures, which are elongated with an average aspect ratio of 0.2, and feature very bright (corresponding to high density) and unresolved knots, connected by lower surface brightness (low density) filaments. As the most dense parts are unresolved and point-like, it can be assumed that the underlying physical structures have even smaller length scales, similar to the previous echo example from light echoes around Cas A.

The brightest features tend to be located towards the lower border (8 o'clock direction) of the echoing clouds. This is a similar effect, as seen at the earlier described Cas A echo, and may indicate the overall direction of motion of the echoing cloud with respect to the surrounding WNM. It is worth noting that the clustering of bright clumps toward the lower border is not an effect of self-extinction of the echoing cloud, as the "light-front" of the supernova reaches the region at an angle of $\sim 90°$ and from even different angles in the case of Cas A echoes. Instead, this effect is a strong indicator of the shock formation model of such structures by supersonic collisions of CNM fragments.

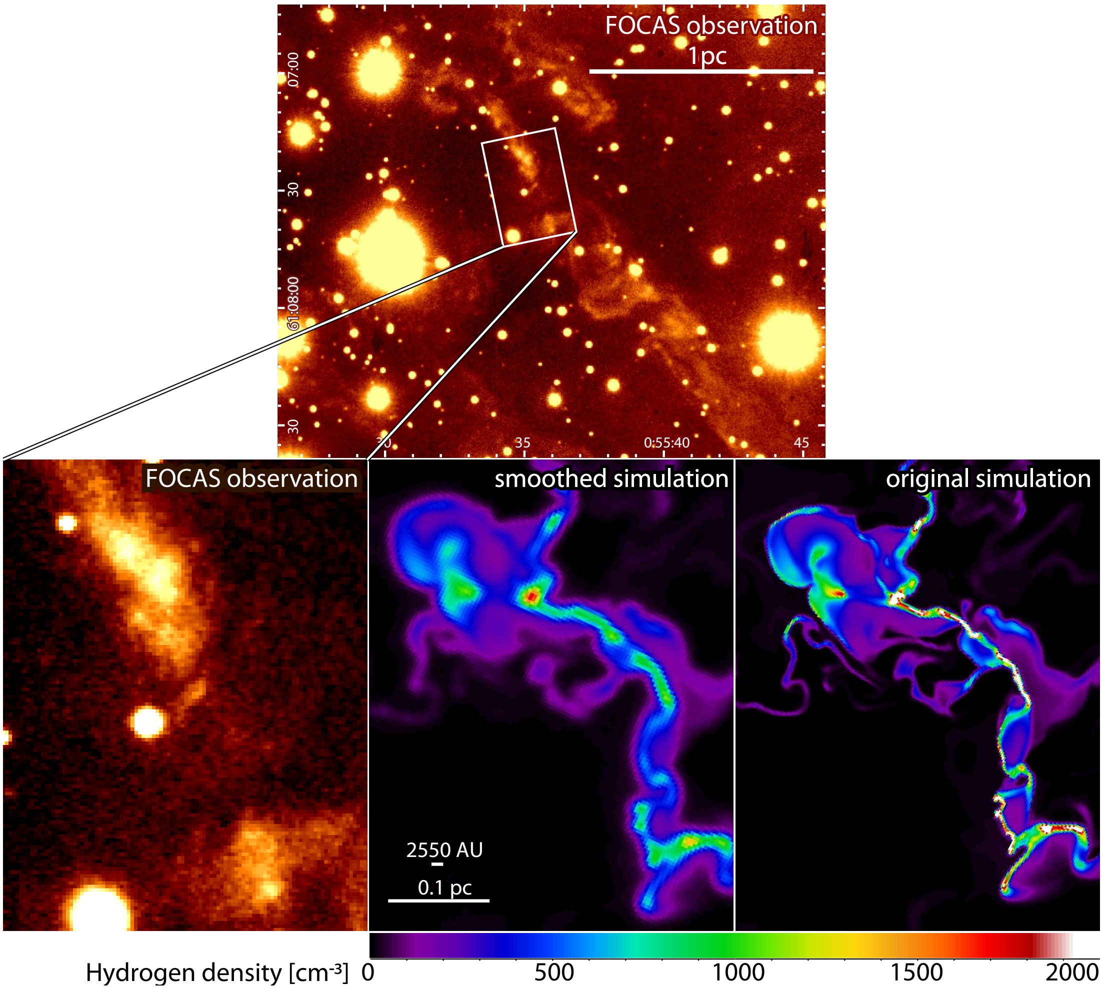

Figure 3.9: R-band observations of a light echo from Tychos supernova with FOCAS. A zoom on the brightest area is shown in the bottom panel, along with a reminiscent area from the ISM simulation at the same spatial scale in a smoothed and unsmoothed version. This region shows that the echoing clouds are very fragmented in dense cores, which are embedded in immediate density filaments. The resolution limit is about 2550 AU.

3.6 Outlook

3.6.1 Signatures of Magnetic Fields

Figure 3.10 shows a region of infrared echoes, which is different from most other parts of the MIPS field. The average of the derived densities is much lower (about $30\,\mathrm{cm}^{-3}$) and maximum densities are smaller than $250\,\mathrm{cm}^{-3}$. Although the region features many elongated substructures, their aspect ratio is peculiarly low. Some filaments are larger than 2 pc and appear unresolved in the orthogonal direction (< 0.08 pc), yielding to an aspect ratio smaller than 0.04. Such large scale low density filaments are not predicted in the ISM simulation by Hennebelle and Audit (2007). A possible explanation for this

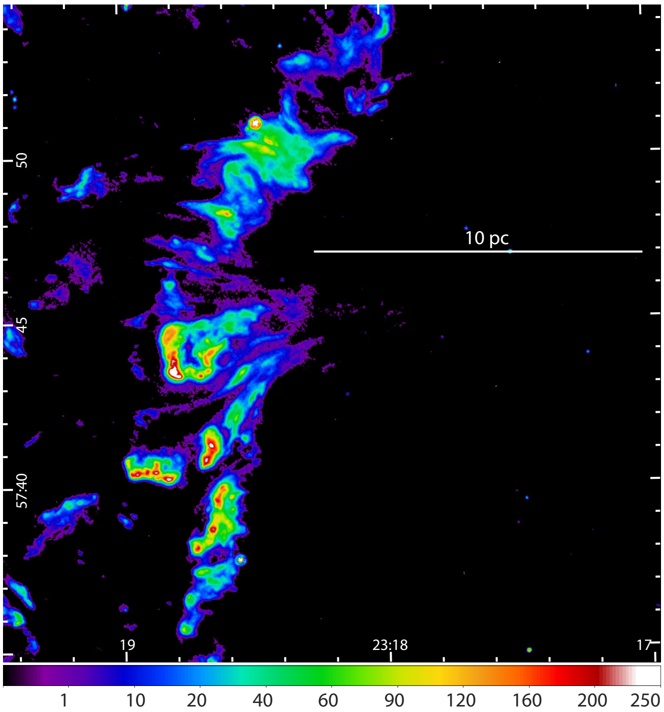

Figure 3.10: Light echo region around Cas A with MIPS, centered on RA: $23^{\mathrm{h}}18^{\mathrm{m}}12^{\mathrm{s}}$, DEC: $+57°44'33''$. The observed structures are unlike the results of the ISM simulation. Long and bended filaments of intermediate densities may be an indication for magnetic fields.

effect is the condensation of CNM structures along magnetic field lines (P. Hennebelle, private communication). It is believed that magnetic fields provide support for the gas to stay in the "unstable", intermediate density regime by the freeze-out of the magnetic field in the dust component. This builds up a counter-pressure to prevent immediate compression of the component. This effect delays the formation of high density structures and the onset of self-gravitational induced star formation (Hennebelle and Teyssier 2008). This effect needs to be addressed in future simulations with sufficient numerical resolution and verified by dust polarization studies from an observational standpoint.

3.6.2 Signatures of Shells and Bubbles in the ISM

The Hennebelle and Audit (2007) simulation does not allow the comparison of size scales larger than 20 pc, but the deprojected MIPS 3° × 3° field offers a probe to an area larger than $200 \times 200\,\mathrm{pc}^2$. Figure 3.11 emphasizes the positions of echoes in this field. It should be noted that the 2D image is a projection of the 3D light echo ellipsoid around Cas A. While echoes very close to Cas A (center of the image) are located about 53 pc *behind* Cas A, echoes at the edge of the field of view are roughly in the same plane as Cas A.

The general structure is reminiscent of the turbulent structure at small scales. Most echo regions are clustered and seem to be interconnected to each other by long fila-

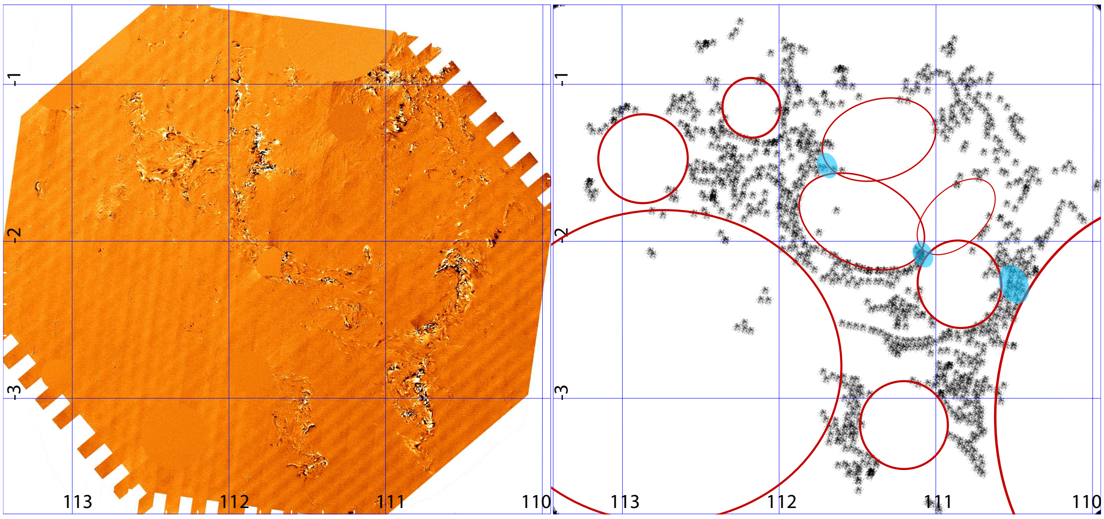

Figure 3.11: *Left*: Difference image between two MIPS 3° × 3° images. Residuals due to the complex PSF's or bright stars and Cas A are masked out. Only emission from light echoes is visible (either from the 2006 epoch in black or from the 2007 epoch in white). *Right*: Positional sketch of echoing clouds for better recognition of large scale structures. On large parts of the projected light echo-ellipsoid no echo emission is present. The overall elliptic structure of these void regions may be the interfaces of shells and wind blown bubbles in the ISM with the light echo ellipsoid. Echo structures with the highest densities are marked in blue.

mentary structures other across several hundred parsec. Most parts of the light echo ellipsoid is devoid of echoing material.

It is noticeable that echoes enclose void regions on elliptic regions. In the 3D deprojection these elliptic regions would correspond to the intersection of spheroids with the light echo ellipsoid. This probably is the imprint of bubbles, shells and cavities in the ISM (Dawson et al. 2011; Heiles 1979). These structures are formed by stellar winds and supernovae, which are the most dominant energy source for interstellar turbulence (Mac Low and Klessen 2004).

A thorough deprojection of these shells could reveal their origin and thus make light echoes a very unique probe of interstellar turbulence and stellar feedback at the same time, as both, the small scale patterns, and the origin of turbulence are inferred.

The accumulation of material at the edges of such bubbles has been suggested to drive molecular cloud formation (e.g. Hartmann et al. 2001; McCray and Kafatos 1987). In fact, the highest density light echoes are found at the intersections of several shell like structures (marked blue in Figure 3.11)

There are also some small isolated echo structures inside the void regions. An important question to address in future studies will be the chemical composition of these isolated groups in comparison to clustered echoes at the edges of the voids and how those structures survived the passage of the stellar winds and/or shocks.

3.6.3 SOFIA and LBT Observations

As the initial infrared echo analysis by Vogt et al. (2012) and the entire dust density estimation is based on a single *Spitzer*-IRS spectrum and MIPS 24 and 70 µm photometry, it is compulsory to verify the universality of the results. As the *Spitzer* space telescope run out of helium, the only facility available for high sensitivity pointed infrared spectroscopy and photometry is the Stratospheric Observatory for Infrared Astronomy (SOFIA; Becklin et al. 2007) until the James Webb Space Telescope (JWST) becomes available in ∼ 2020. SOFIA is a 2.5 m telescope based on Boeing 747SP aircraft, which can be deployed at altitudes up to 45 000 ft, above 99% of the infrared light absorbing water vapor in Earth's atmoshpere.

As part of the early science demonstration time, O. Krause and I were able to acquire two 1800 s images of echoing regions at 19.7 and 31.5 µm with the Faint Object InfraRed CAmera for the SOFIA Telescope (FORCAST, Herter et al. 2012). The chosen region (RA: $23^h22^m11^s$, DEC: $+59°33'27''$) featured very high surface brightness echo emission (up to 150 MJy/sr) during the entire *Spitzer* monitoring time from 2005 till 2008 and is already detectable in IRAS images from 1983. The used broad band filters ($\Delta\lambda = 5.5\,\mu m$) do not cover any emission lines and would directly probe the thermal emission component of the echo SED, ideal for constraining dust masses and densities. The higher spatial resolution ($\sim 3''$) allows the detection of physical structures of 0.05 pc at the distance of the echoes.

The RAW images revealed no discrete sources, thus image stacking had to be performed according to image shifts and rotations documented in the corresponding file headers. The co-added image (Figure 3.13) reveals no sources, but only the noise pattern from the telescope assembly.

Using the same co-addition technique, an in-flight calibration image of α-Boo was rereduced to check the validity of the approach. The resulting image is shown in Figure 3.12. As seen in the image, the star was not aligned according to the image header coordinates, even image rotations changed undocumented during the observing time.

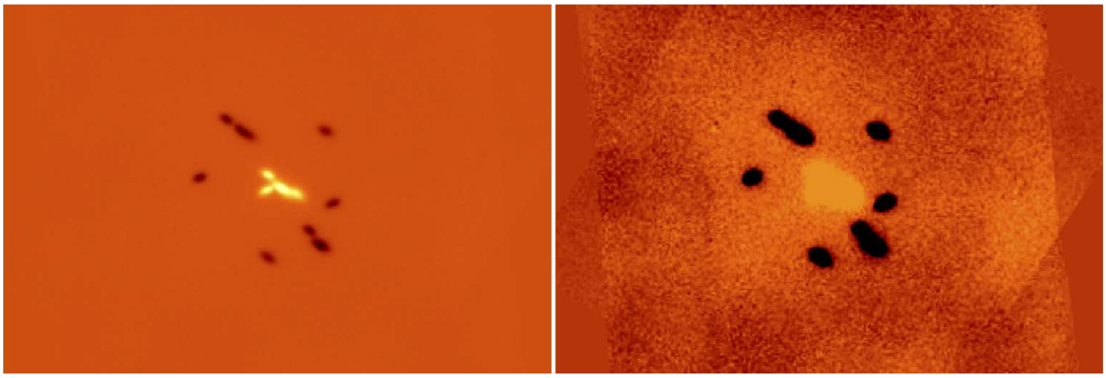

Figure 3.12: SOFIA calibration observations of the α Bootis. Our flight suffered from technical failures resulting in undocumented line-of-sight rewinds, which are only recoverable on observations of bright sources. The image in the right panel is equivalent to the left panel, expect for a colorbar stretch to make the noise structure visible.

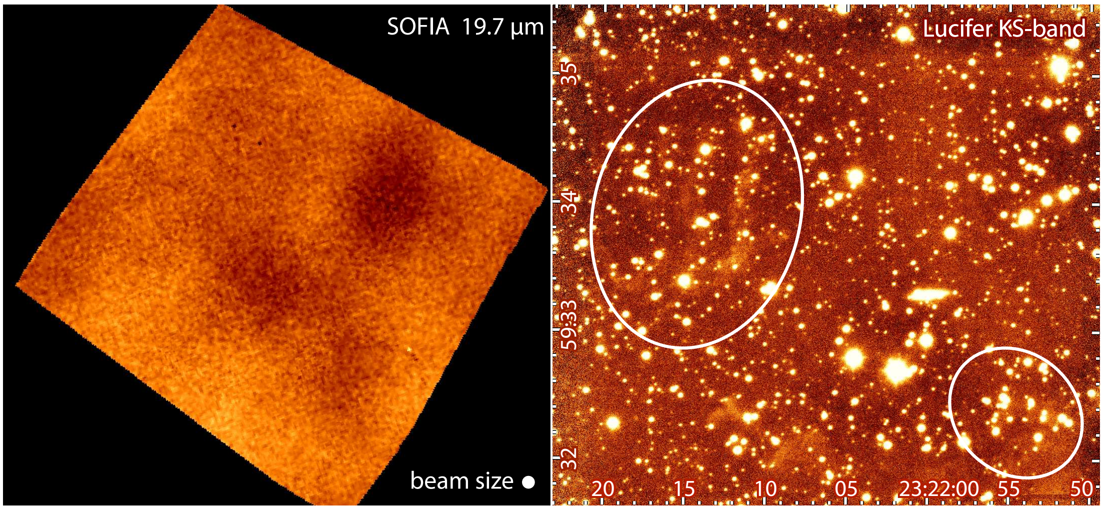

Figure 3.13: (*Left*): Acquired SOFIA image on June 10th 2010. Only the noise pattern is visible, no light echoes. (*Right*): LBT-Lucifer K_S-band image of the same region observed with SOFIA on April 30th 2010. Light echoes are clearly present in the field.

The rotation visible in the image is induced by undocumented line-of-sight rewinds, performed when the internal image-derotator exceeds its limits and has to back-up to the central position. This effect should have been documented in the according file header, but due to technical problems was not recoded during our flight. The recovery of such effects is only possible with bright stars in the field-of-view, but cannot be recovered for observations where no bright emission is present in the single images.

It is also evident that the achieved signal-to-noise (SNR) ratio is worse then expected for the instrument[1]. The shown image fails the expected SNR by a factor of 10. An exactly rotated and shifted (based on the central PSF peak of α-Boo) image stack features a central peak whose SNR is lower by a factor of two.

By chance, it was also possible to acquire a 1800 sec K_S-band image of the same region with LUCIFER on the 8.4 m Large Binocular Telescope (LBT; Hill et al. 2006). The image was taken during morning twilight and is able to reach the same limiting magnitude as a 3600 sec Omega2000 image (part of it shown in Figure 3.4).

As evident from Figure 3.13, some faint echo emission is present in the LBT image, although not as many and bright echo features as the images from the earlier epochs revealed around this location. No correlation of emission features between the LBT image and the SOFIA image can be seen. The surface brightness variations in the SOFIA image must therefore be attributed to the thermal noise level of the instrument.

Although less echo emission is evident in the LBT image than expected, it is still present and the non-detection of echo-emission by SOFIA can not be attributed to the lack of the source, but rather to technical problems (undocumented line-of-sight rewinds) and lower than expected sensitivity in the early science demonstration time

---

[1] The SOFIA Instrument Time Estimator (SITE; https://dcs.sofia.usra.edu/proposalDevelopment/SITE/) estimates a SNR of 1700 for α-Bootis at 19.8 µm.

phase. SOFIA observers of faint diffuse objects should make sure that a bright point source is present in the observed field until the image shifts and rotations can be reliably extracted from the image header.

3.6.4 Future Observations with Scales $< 2000\,\mathrm{AU}$

Investigations of size scales smaller than $\sim 1000\,\mathrm{pc}$ would be desired to identify TSAS-like structures by echoing regions. As the projected thickness of the radiation burst of the supernova already has a size of $\sim 2500\,\mathrm{pc}$, one has to keep in mind that successive structures might be illuminated simultaneously and resulting images would be dominated by diffuse emission, as all CNM structures along the line-of-sight are projected onto a single plane. This results in smearing of the structures, similar to the overall appearance of infrared cirrus clouds in the local vicinity of the sun.

Due to the overall beam size of current mid-infrared telescopes, such as *WISE* (see chapter 2.2), very short time baseline observations would not reveal any imprinted structure. Due to the survey strategy, *WISE* observed a single region with a time interval of $\sim$ 95 minutes for about 24 hours, which corresponds to physical sizes of $\sim 8\,\mathrm{AU}$ and $\sim 100\,\mathrm{AU}$. No variations are seen in such time intervals, as the spatial resolution of 0.1 pc averages through all small scale structures.

High resolution images with the upcoming *James Webb* Space Telescope could reveal spatial structure and density fluctuations down to 300 AU with combined NIRCam and MIRI imaging.

3.7 Summary

I compared observations of light echoes from supernovae with high resolution numerical simulations of the turbulent flow of neutral atomic hydrogen in the interstellar medium. Using a variety of infrared survey observations with *Spitzer* and high-resolution images from optical telescopes, it was possible to uniformly probe structures spanning over more than four orders of magnitude in size, from 200 pc to about 2 000 AU. As the expanding light outburst of the supernova acts as a "flash light", which briefly illuminates dust structures, it is possible to analyze thin slices of the interstellar medium. The observations are independent of strong background sources to study absorption line features and independent of nearby radiation sources, which could provide feedback to the structures themself. Therefore, it is possible to gain access to pristine interstellar material and describe both large and small scales in a consistent manner.

The comparison reveals striking similarities of the observed structures with the simulated turbulent flow fields in the ISM. Over all covered scales, structures are self similar. The derived density field for light echoes is consistent with an origin of the emission in the densest cusps of the cold neutral medium. Echoing clouds are fragmented into dense substructures, which are connected to each other by filaments of intermediate density. These structures are usually very elongated with aspect ratios smaller than 0.4. The three-dimensional analysis shows that most features are in fact sheet-like, as expected for structures formed in colliding turbulent flows.

Unresolved very high density fragments suggest an origin in shocked layers of the CNM. Those regions harbor the so called TSAS, which are the smallest resolved dense cores revealed from radio observations and simulations. The relative direction of motion of shocked structures can be inferred from the compression ratio on the side of the shock.

The presence of such turbulence induced shocks within the CNM fragments might also be an alternate explanation for dust processing (see Boulanger 2006; Micelotta et al. 2010) observed in a bright echo-spectrum. This would in turn mean that these structures feature the observed properties *initially*, and are not induced by the supernova UV flash.

Some of the observed echoing regions indicate the presence of magnetic fields, which lead to lower density filaments and delay the formation of high density substructures.

In the future light echo observations might also be a probe to stellar feedback. The global three dimensional distribution in *IRAS*, *Spitzer* and *WISE* data might allow a construction of the underlaying flow field and might point to local sources of interstellar turbulence, as indicated by the observed large voids of CNM structures which might be the borders of wind or shock driven shells and bubbles in the ISM.

4 The Dust Content of Cassiopeia A

In this chapter I use Herschel photometry of the supernova remnant Cassiopeia A to study its dust content. This research contributes to the longstanding discussion, whether supernovae are a reasonable origin of dust in the early universe or not.
After disentangling different emission components, a small amount of cool supernova dust is found. This cool dust component is located within the supernova reverse shock, indicating that it could be destroyed by the following passage of the shock. This study provides evidence, that these kinds of supernovae are likely not a significant dust polluter of the ISM and could even dilute its dust content.
Parts of the following chapter have been published in Barlow et al. (2010).

4.1 Introduction

The death of massive stars ($\geq 8\,\mathrm{M}_\odot$) is responsible for the vast production of elements heavier than Oxygen in the Universe. Supernovae (SNe) eject large amounts of these elements into the interstellar medium (ISM), synthesized during their stellar evolution and their final explosive burning. As the evolutionary timescale for those stars is relatively short (several millions of years), compared to their low-mass siblings (billions of years), they are the *only* source of metals in the very early Universe.

Observations of galaxies and quasars at high redshifts find large quantities of dust (e.g. Bertoldi et al. 2003; Priddey et al. 2003) at a time when the Universe was just one tenth of its present age. Today, the main source for dust injection in our Galaxy is thought to be the winds of asymptotic giant branch (AGB) stars (Morgan and Edmunds 2003). But in the early Universe there were no such stars present, as they did not have enough time to evolve from the main sequence. Only massive stars evolve fast enough to reach phases of high mass-loss, and herewith provide possible environments for dust formation, in a short period of time. Could supernova explosions therefore provide the required dust quantities seen in these high redshift sources?

Models of core-collapse supernovae predict the condensation of dust grains inside the dense, metal-rich He core in the expanding ejecta. Up to $0.1 - 1\,\mathrm{M}_\odot$ of dust is predicted per SN (e.g. Kozasa et al. 1991; Todini and Ferrara 2001), which appears to be sufficient to explain the dust observed in objects in the early Universe (e.g. Dwek et al. 2007; Morgan and Edmunds 2003).

Observations of supernovae confirm an on-set of dust formation several hundred days after the initial explosion, indicated by an increasing mid-infrared flux density (see Kozasa et al. 2009, for a review). But these studies only find trace amounts of hot dust (on the order $10^{-4} - 10^{-3}\,\mathrm{M}_\odot$ at $100 - 400\,\mathrm{K}$). Furthermore, it is also possible that some grain species can cool down very quickly, so that near- and mid-infrared observations would miss this dust component, making the above mentioned masses a lower limit.

Dust production in supernova explosions is, however, just one part of the story. Driven by the encounter of expanding ejecta with the surrounding circumstellar- and interstellar medium (CSM and ISM), a fast reverse shock forms and falls back into to the supernova ejecta. A hot plasma builds up inside the supernova remnant between this reverse shock and the before mentioned outer boundary of the ejecta (forward shock). Before being ejected into the ISM, dust grains have to pass this hot plasma, where the grains are exposed to erosion and destruction by sputtering due to the ubiquitous energetic ions. Their survival heavily depends on grain composition and size of the condensed dust (Nozawa et al. 2010). These authors even suggest that dust destruction by the reverse shock may be completely effective, leaving no freshly produced dust behind. Thus, supernova could dilute the dust content of the ISM by the propagation of the blast wave.

Studies of proximate supernova remnants thus seem promising targets for further investigation of their net dust contribution to the ISM. Cassiopeia A is a young (330-340 years, Fesen et al. 2006) and nearby (3.4 kpc, Reed et al. 1995) hydrogen-deficient Type IIb (Krause et al. 2008a) supernova remnant, which has been intensively studied over the entire electromagnetic spectrum. Using near- and mid-infrared observations with the *Spitzer* Space Telescope, Hines et al. (2004) and Rho et al. (2008) estimate $0.02 - 0.08\,\mathrm{M}_\odot$ of $60 - 300\,\mathrm{K}$ dust to be emitting between 5 and 70 µm, particularly in a bright ring coincident with the current position of the reverse shock.

Dunne et al. (2003) use submillimeter 450 and 870 µm SCUBA observations to find evidence for $2 - 4\,\mathrm{M}_\odot$ dust in Cas A at a temperature of $\sim 18\,\mathrm{K}$, which is significantly more than all earlier estimates and the predictions of dust formation models for supernova explosions. Using the same technique, Morgan et al. (2003) find a $\sim 1\,\mathrm{M}_\odot$ cold dust component in another nearby supernova remnant (Kepler's supernova). Those dust masses could not be attributed to swept-up circumstellar or interstellar dust, as both remnants are still young. The authors conclude that these dust masses are directly connected to the supernova remnant.

Contrariwise, these observations are challenged by Krause et al. (2004), who argued that most submillimeter excess could be associated to foreground molecular clouds and derived an upper limit of $0.2\,\mathrm{M}_\odot$ of 18 K cold dust for Cas A. This was recently confined by Sibthorpe et al. (2010), who find only $0.07\,\mathrm{M}_\odot$ of freshly formed dust at 40 K using observations made with the *AKARI* satellite and the BLAST experiment.

In this study I aim to use the high resolution far-infrared capabilities of the *Herschel* Space Observatory (Pilbratt et al. 2010) to spatially resolve this possible cold dust component inside Cas A and try to characterize its content and vulnerability to destruction by the reverse shock.

4.2 Observations and Data Reduction

4.2.1 Herschel Space Observatory

As part of the `Mass`-loss of `E`volved `S`tar`s` (MESS) Guaranteed Time Key Project (Groenewegen et al. 2011), the *Herschel* Space Observatory observed the supernova remnant Cas A with both of its imaging instruments PACS and SPIRE.

The Photodetector Array Camera and Spectrometer (PACS, Poglitsch et al. 2010 features two bolometer arrays with 64 × 32 pixels observing at 70 and 100 µm and an array with 32 × 16 pixels at 160 µm, as well as an integral field spectrometer array of stressed and unstressed Ge:Ga detectors (5 × 5 spatial pixels with 16 spectral pixels each). The bolometer arrays operate at a temperature of 0.273 K, which is provided by closed cycle ^{3}He coolers. Observed beam sizes (FWHM) are 5.8, 7.8 and 12″ for 70, 100 and 160 µm, respectively.

PACS observed Cas A on December 17th 2009 using the 70 + 160 µm and 100 + 160 µm dual-channel modes, using two orthogonal scan legs with a length of 22′ and a scan speed of 20″/s. For each of the filter pairs the on-source integration time was 2376 seconds. The uncertainty in absolute flux calibration is estimated to be 20%.

Data from PACS was reduced with the *Herschel* Interactive Processing Environment (HIPE; Ott 2010). The Microwave Anisotropy Dataset mapper (MADmap; Cantalupo et al. 2010) was used to remove effects from uncorrelated 1/f noise of the individual bolometers. Interim calibration factors of 1.05, 1.09 and 1.29 were applied to be consistent with the most recent calibration results (Poglitsch et al. 2010).

The Spectral and Photometric Imaging Receiver (SPIRE, Griffin et al. 2010) features three imaging bands (centered at 250, 363 and 517 µm) and a Fourier Transform Spectrometer. The photometer observes a 4′ × 8′ field simultaneously using a stack of bolometers which are cooled to 0.273 K. The diffraction limited beams have a FWHM of 18, 25 and 36″ in the three channels. Scan maps are used to increase the field of view. The uncertainty in absolute flux calibration is estimated to be 15%.

SPIRE observed the Cas A supernova remnant on September 12th and December 17th 2009 using 32′ × 32′ scan maps in all three bands. The on-source integration time was 2876 seconds.

Data from SPIRE was reduced using the standard photometer pipeline (HIPE v. 3.0 506, Griffin et al. 2010, the 250, 350 and 500 µm data products were multiplied by 1.02, 1.05 and 0.94, respectively to be in line with the most recent calibration campaign (Swinyard et al. 2010) available at this time.

A composite of the obtained *Herschel* images in the six photometric bands is presented in Figure 4.1. The 70 µm PACS image closely resembles the warm dust emission seen in a *Spitzer* 24 µm image (see Figure 4.7) at a similar angular resolution. A bright ring of dust emission coincides with the position of the reverse shock, which is encircled by a fainter outer emission component whose edge is coincident with the forward shock. At longer wavelengths, diffuse structures of interstellar dust emission become more and more prominent. At 250 and 350 µm these structures are the dominant emission contributers and the contour of the supernova remnant is barely detectable. Bright interstellar emission is present at the central, western and southern parts of the rem-

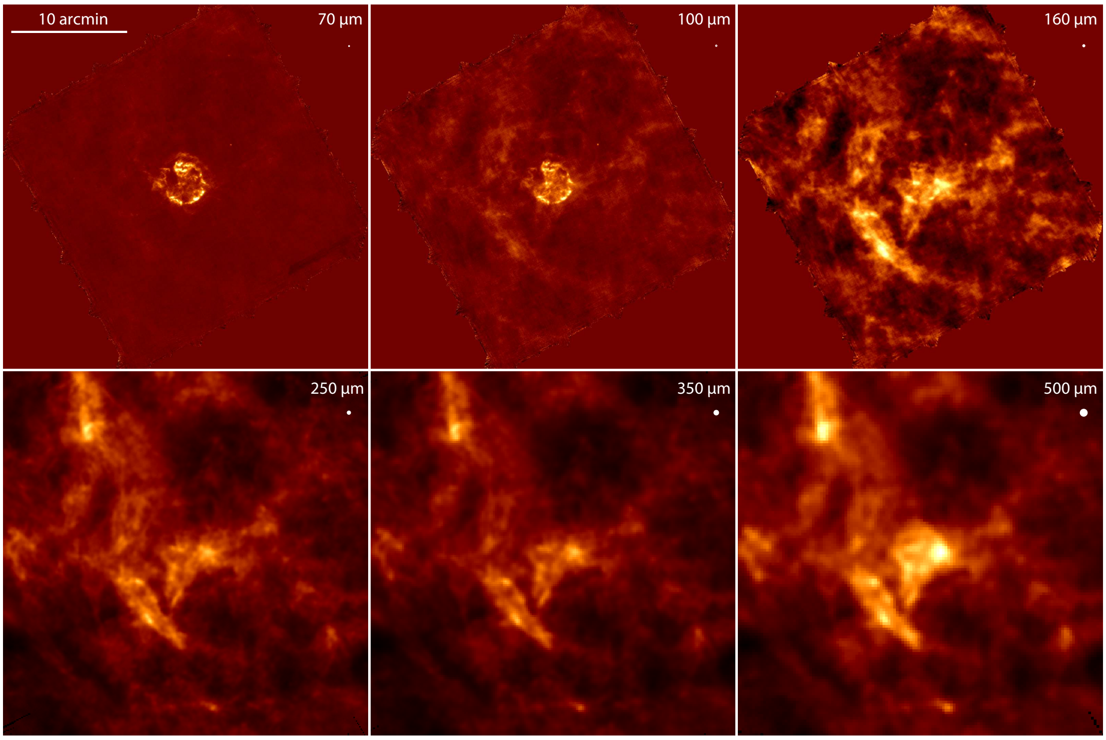

Figure 4.1: Images of Cas A, obtained with *Herschel*-PACS (top row) and SPIRE (bottom row), centered at $23^{\mathrm{h}}23^{\mathrm{m}}26\overset{\mathrm{s}}{.}3$ $+58°48'51\overset{''}{.}33$ (J2000.0). *North is up and east is to the left.* The instruments resolution is indicated for each band with a filled circle at the top right. For PACS the FWHM resolutions are 5.8, 7.8 and 12″ at 70, 100 and 160 µm, respectively. The SPIRE bands feature a beam-size of 18, 25 and 37″ at 250, 350 and 500 µm, respectively.

nant. Their morphology closely matches that of ^{13}CO molecular line maps presented by Wilson and Batrla (2005). In the 500 µm SPIRE image, emission from the non-thermal synchrotron component becomes prominent and the remnant stands out as a special feature again.

As *Herschel* does not measure absolute flux levels, a comparison to *DIRBE* data was carried out, using the maps as presented in an *AKARI*/BLAST-study by Sibthorpe et al. (2010). Although DIRBE has a beam of 44′ (FWHM), it was specifically designed to measure absolute flux levels. We therefore calibrated our maps at the position RA: $23^{\mathrm{h}}22\overset{\mathrm{m}}{.}8$, DEC: $+58°55'$ (J2000.0) with offsets of 29, 58, 150, 178, 87 and 48 MJy/sr, for the six PACS and SPIRE bands. Photometry was then carried out relative to "floor" regions located to the north and southwest of the remnant.

Table 4.1 lists the total observed flux densities within an aperture radius of 165″, centered at RA: $23^{\mathrm{h}}23^{\mathrm{m}}26\overset{\mathrm{s}}{.}98$, DEC: $+58°48'45\overset{''}{.}9$ (J2000.0), which should encompass everything within Cas A's forward shock located at 153 ± 12″ (Gotthelf et al. 2001).

Table 4.1: Total and individual component flux densities of Cas A.

	70 µm	100 µm	160 µm	250 µm	350 µm	500 µm
Total Flux	169 ± 17	192 ± 19	166 ± 17	168 ± 17	92 ± 10	52 ± 7
Non-Thermal	6.3 ± 0.6	8.1 ± 0.7	11.2 ± 0.9	15.4 ± 1.1	19.4 ± 1.3	24.9 ± 1.6
Warm dust	120 ± 12	63 ± 6	22 ± 2	7.0 ± 0.8	3.1 ± 0.4	1.2 ± 0.2
Emission lines		16 ± 2				
Cold SN dust	25 ± 7	29 ± 11	10 ± 17	4.6 ± 17	0.5 ± 10	
Interstellar dust	18 ± 4	76 ± 11	123 ± 17	141 ± 17	59 ± 10	27.5 ± 7

Notes – All flux densities are given in Jy. Values denote the total flux within an aperture of $165''$ radius centered at RA: $23^{h}23^{m}26\overset{s}{.}98$, DEC: $+58°48'45\overset{''}{.}9$ (J2000), which should encompass everything within Cas A's forward shock located at $153 \pm 12''$ (Gotthelf et al. 2001).

4.2.2 Other Data sets

In order to perform a disentanglement of the different emission components towards Cas A, I use several additional archival data sets from space and ground based observatories to better investigate the warm dust and non-thermal synchrotron emission components.

4.2.2.1 Spitzer MIPS Observations

As a template for shocked warm dust emission I extracted a *Spitzer*-MIPS 24 µm image from the *Spitzer* Science Archive (PID: 21899520, PI: G.Rieke, observation date: January 7th 2008). The dataset, which was acquired in the photometry mode, was reduced using the MIPS Data Analysis Tool (DAT; Gordon et al. 2005), starting at the RAW data product level.Special care was taken to remove signatures from the polluted scan mirror and the "jailbar" effect, which is ubiquitous in bright sources like Cas A.

The MIPS 24 µm image (see Figure 4.7) is dominated by thermal emission from small dust grains, which formed either in the pre-supernova wind or in the ejecta of the supernova itself (Arendt et al. 1999), heated by electrons within the hot plasma between the forward and reverse shock of the supernova. This emission component is at its brightest at the position of the reverse shock and is much less defined at the outer boundary of the supernova blast wave, which may indicate mixing with its surrounding circumstellar and interstellar medium. Additionally, this image shows a northeastern jet and southwestern counter-jet, indicating the symmetry axis of a probable axisymmetric explosion of Cas A (Hines et al. 2004).

4.2.2.2 Spitzer IRAC Observations

Ennis et al. (2006) noted morphological similarities of the emission seen in *Spitzer*-IRAC 3.6 µm and Very Large Array (VLA) 6 cm data, indicating a common origin from the non-thermal synchrotron emission component. Synchrotron emission arises from spiraling electrons a magnetic field. For further analysis I extracted basic calibrated data (BCD) from the *Spitzer* pipeline S18.7.0 from AOR-Key: 10737152 and 17849344 (PI:

L. Rudnick) taken on January 19th 2005 and December 28th 2006, respectively. The data was reduced according to the IRAC Instrument Handbook[1] using the MOsaicker and Point source EXtractor (`MOPEX`). The final PSF size is $1.66''$ (FWHM).

The image from 2005 is presented in Figure 4.2, *left*. It shows a bright ring, coincident with the position of the reverse shock region and a faint plateau, which ends at the position of the forward shock. Overall, it is dominated by diffuse filamentary structures.

4.2.2.3 Radio Observations

Archival VLA data at 21 and 6 cm (from November 30th 1997) represent the highest resolution radio images available (FWHM $\sim 1.6''$). For comparison, the 3.7 mm images from BIMA at the Hat Creek Radio observatory (taken on January 16th 1997, Wright et al.) already have a beam size of $\approx 6.35''$ (FWHM). Newer Mustang and Gismo maps (taken in Nov/Dec 2009, J. Staguhn) suffer from course resolution ($9''$ and $18.5''$). Nevertheless, they can be used for a global spectral index derivation of the non-thermal synchrotron emission component.

4.3 Emission Component Decomposition

To reveal the existence of a possible cold, unshocked dust component within the supernova remnant, the more prominent emission components will be successively subtracted from each *Herschel* band. First, the well studied non-thermal synchrotron emission and the warm dust components are subtracted. Estimated emission line contributions in PACS bands are also accounted for. After this, an iterative procedure to isolate the cold supernova and cold interstellar dust components will be applied.

4.3.1 Non-Thermal Emission

Gerardy and Fesen (2001) and Rho et al. (2008) first noted the similarities of near-infrared K_s-band images to radio continuum maps and inferred a common origin by synchrotron emission. Ennis et al. (2006) extended the detection of non-thermal synchrotron emission to the IRAC 3.6 µm band, where no strong line and hot dust emission is present. To reliably describe the non-thermal synchrotron emission component in the *Herschel* bands, I characterize the synchrotron spectral index from both both sides of the *Herschel* wavelength regime.

As the IRAC image still contains emission from other components (stars and light echoes) and is influenced by interstellar extinction they are subtracted consecutively.

Infrared Light Echo Decontamination

The 3.6 µm image (Figure 4.2, left) still contains scattered emission from near infrared light echoes. They are especially present in the western parts and the central northern "ring"-structure. To eliminate light echo emission, the difference image technique (as

---

[1] http://irsa.ipac.caltech.edu/data/SPITZER/docs/irac/iracinstrumenthandbook/

described in chapter 2.1.3) is applied to the two IRAC images, which were taken nearly two years apart from each other. The resulting image contains the signal from light echoes in the two epochs as either positive or negative values. By subtracting the respective positive or negative image components from the original images, an image free of light echoes can be obtained. Such an image is presented in the middle of figure 4.2.

Stellar Emission Decontamination

As the near-infrared image is still crowded by the Rayleigh-Jeans tail of stellar emission, PSF subtraction is performed using the `Starfinder`[2] software package. Due to the complex outer PSF of *Spitzer* and many saturated stellar sources, residuals remain. These residuals are corrected by local polynomial background fitting. The errors introduced by such a fitting procedure are much smaller than the errors introduced by the PSF-fitting residuals; considering the total synchrotron flux, they are smaller than 1%. The resulting star-free image is presented in Figure 4.2 on the right.

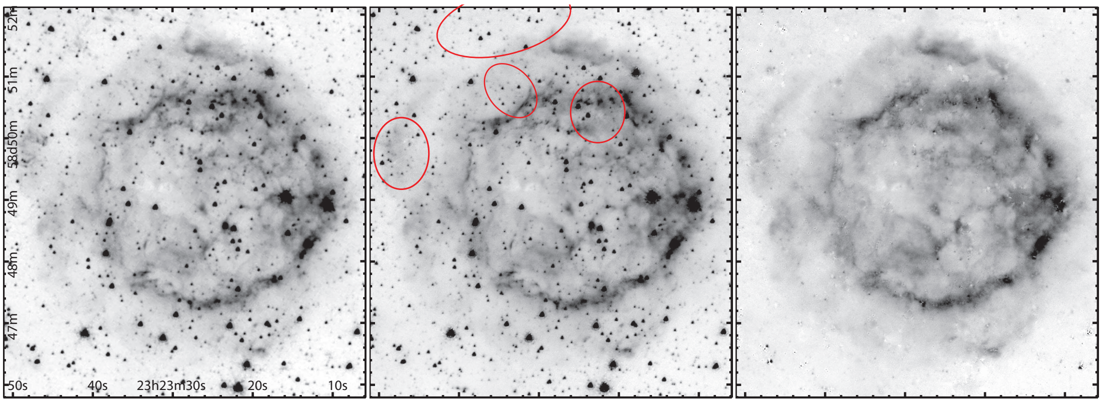

Figure 4.2: *Left*: Image of Cas A obtained in the *Spitzer*-IRAC 3.6 µm channel. The emission present in this band mostly originates from non-thermal synchrotron emission. Prior to the use as a non-thermal image other contributers had to be subtracted.
Middle: Emission from light echoes is eliminated (mainly within the red regions). The positions and fluxes of light echoes were determined by a difference image obtained from another observation of Cas A with IRAC.
Right: Stellar emission is eliminated by PSF subtraction and polynomial background fitting where necessary. Emission present in this image originates mainly from non-thermal synchrotron emission.

Interstellar Extinction

Cassiopeia A is subject to strong interstellar extinction (Eriksen et al. 2009, $A_V = 6.2$) due to intermediate molecular clouds in the line of sight, especially in the western parts

---

[2] http://cfao.ucolick.org/software/starfinder.php

of the remnant. Willingale et al. (2002) presented a column density map derived from X-ray absorption measurements over the entire remnant. Based on this map, I calculate the extinction corrected flux $F_{\rm cor}$ at each position as

$$F_{\rm cor} = F_{\rm in} \times 10^{(A_\lambda/A_V \times A_V/2.5)} \tag{4.1}$$

with the extinction coefficients $A_{\lambda=3.6\mu\rm m}/A_V = 0.058$ (Rieke and Lebofsky 1985) and $A_V = N_H/2.21 \times 10^{21}$ (Güver and Özel 2009), where N_H is the observed column density from Willingale et al. (2002) and $F_{\rm in}$ is the uncorrected flux.

Synchrotron Spectral Index Fitting

The total synchrotron flux within the 165″ aperture was determined for all radio maps and the 3.6 µm IRAC observation and plotted in Figure 4.3; to ensure sampling of the same region in all bands, the maps have been convolved to a common resolution prior to performing aperture photometry. The frequency dependent fading (∼ 0.9%/year at 6 cm) of the Cassiopeia A's radio flux was accounted for as described in Reichart and Stephens (2000).

Emission from non-thermal synchrotron emission S_ν can be described as

$$S_\nu \propto \nu^\alpha, \tag{4.2}$$

with the frequency ν and the spectral indexα which determines the power-law slope of the spectrum. A least-squares fit was performed for the Cas A data, resulting in

$$\alpha = -0.69 \pm 0.02 \tag{4.3}$$

Using the derived spectral index α and the VLA 6 cm image, I created synthetic non-thermal synchrotron emission maps for the corresponding resolutions and wavelength of the six PACS and SPIRE bands. Figure 4.4 shows the *Herschel* images with the appropriate non-thermal component image subtracted.

4.3.2 Warm Supernova Dust

The MIPS 24 µm image is shown in Figure 4.7. Hines et al. (2004) noted a similar morphology of their 24 µm and 70 µm images, which peak in a bright ring coincident with the position of the reverse shock. They inferred a common emitting component, which they fitted by warm (82 K) magnesium protosilicate.

The PACS 70 µm image has a higher resolution (similar to MIPS 24 µm) and deeper extended emission sensitivity than the earlier MIPS 70 µm image. Faint extended emission within the position of the reverse shock is visible (Figure 4.7), which was not detected in the *Spitzer* MIPS image by Hines et al. (2004).

In order to eliminate the common warm emission component in the MIPS 24 µm and PACS 70 µm image, the 24 µm image was scaled to match the surface brightness levels of the outer parts of the remnant in the PACS 70 µm image and was then subtracted. The resulting difference image is shown in Figure 4.7. The contribution of the warm component in the 70 µm image can be estimated as 120 ± 6 Jy.

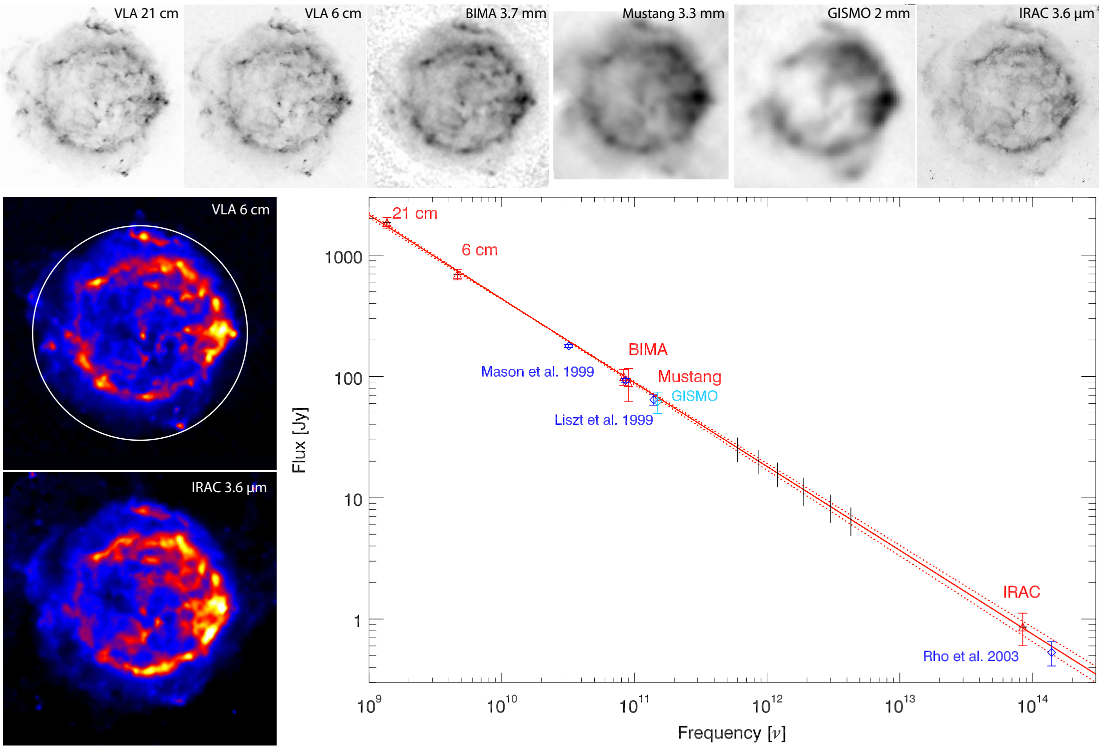

Figure 4.3: Estimation of the non-thermal synchrotron emission component within the *Herschel* bands.
Top: Various radio, sub-mm and infrared images of the non-thermal synchrotron emission component at their corresponding native resolutions. *Left*: Direct comparison of the morphology in the 6 cm VLA (convolved to 6″ FWHM) map and the corrected 3.6 µm IRAC image (convolved to 6″ FWHM), which correspond very closely, indicating their common non-thermal origin.
Right: Spectral energy distribution of the total flux density within a 165″ radius (circle in VLA 6 cm image) of all data sets, along some other values from the literature, I used to derive the spectral index of the non-thermal component. Least-square fitting yields a spectral index of $\alpha = 0.69 \pm 0.02$. The center wavelength of the six *Herschel* bands are indicated as short black lines.

This emission component was then extrapolated to longer wavelengths using the predicted spectrum for 82 K magnesium protosilicate (Dorschner et al. 1980) found by Hines et al. (2004) to fit the 24–70 µm MIPS spectrum. The inferred flux densities for this warm dust emission component are listed in the 4th row of Table 4.1. Images with a proper subtraction of this component are presented in Figure 4.5.

4.3.3 Emission Line Contributions

Docenko and Sunyaev (2010) observed Cas A with the ISO-LWS spectrometer between 43 and 197 µm. Their spectra, obtained for six on-source and one off-source positions

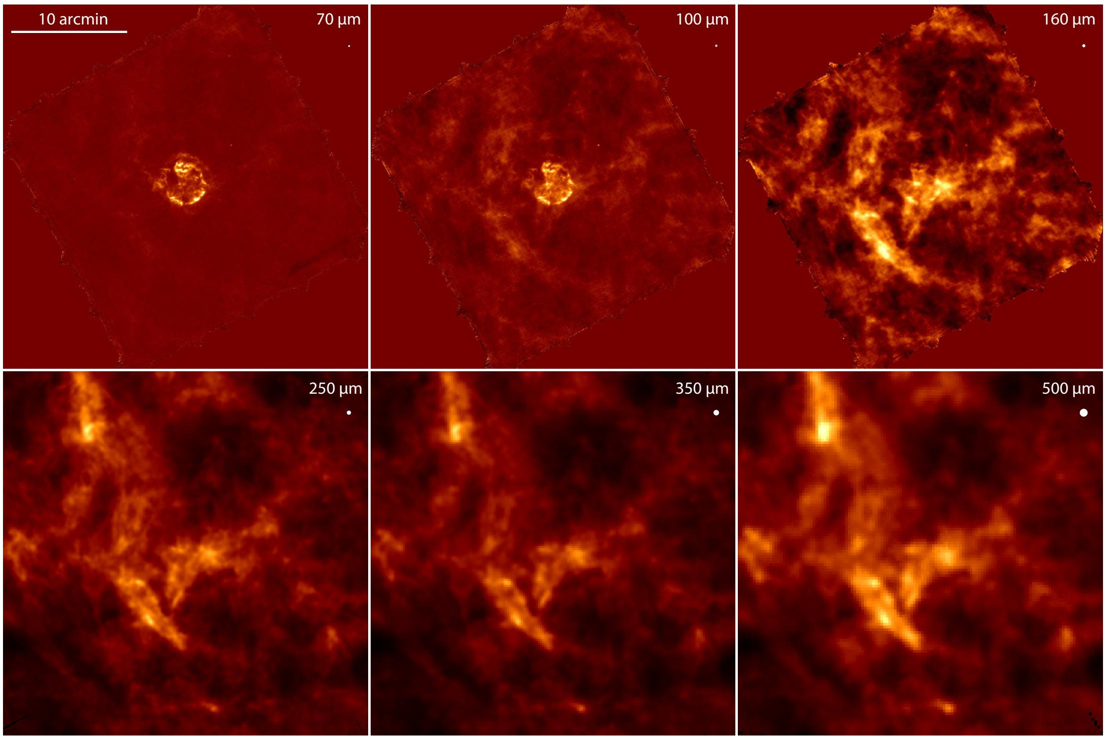

Figure 4.4: *Herschel* images (as in Figure 4.1) after subtraction of the non-thermal synchrotron emission component. Signatures of the Cas A supernova remnant are now barely visible in the three SPIRE bands, especially at 500 µm, where the non-thermal component dominated the total emission towards Cas A.

with an 80″ aperture, show broad emission from the [O I] 63 µm and [O III] 52 and 88 µm lines. After convolution with the PACS filter and instrumental response functions, the line contributions in the 70 and 160 µm bands are found to be negligible. However the 88 µm line flux makes a ∼ 16 Jy contribution to the PACS 100 µm band. This contribution was accounted for accordingly in the further analysis.

4.3.4 Cold Supernova and Cold Interstellar Dust

The warm-dust subtracted images in Figure 4.5 show a similar inner morphology of Cas A in the 70 and 100 µm band. At longer wavelengths the diffuse emission from interstellar dust dominates the field of view. To separate and investigate these two components individually, an iterative procedure was used to produce ”cold dust” and ”ISM” images.

In the following, all PACS images were convolved to the 160 µm resolution. For several bright ISM regions outside of the remnant, average 70/160 and 100/160 µm flux ratios for the ISM were determined. The corresponding ratios are 0.13 ± 0.02 and 0.45 ± 0.03. These ratios were applied to the 160 µm image and subtracted from the 70 and 100 µm image accordingly. The resulting 70 and 100 µm cool SN dust images show a consistent morphology. In this first step, a contribution of this cool SN dust component

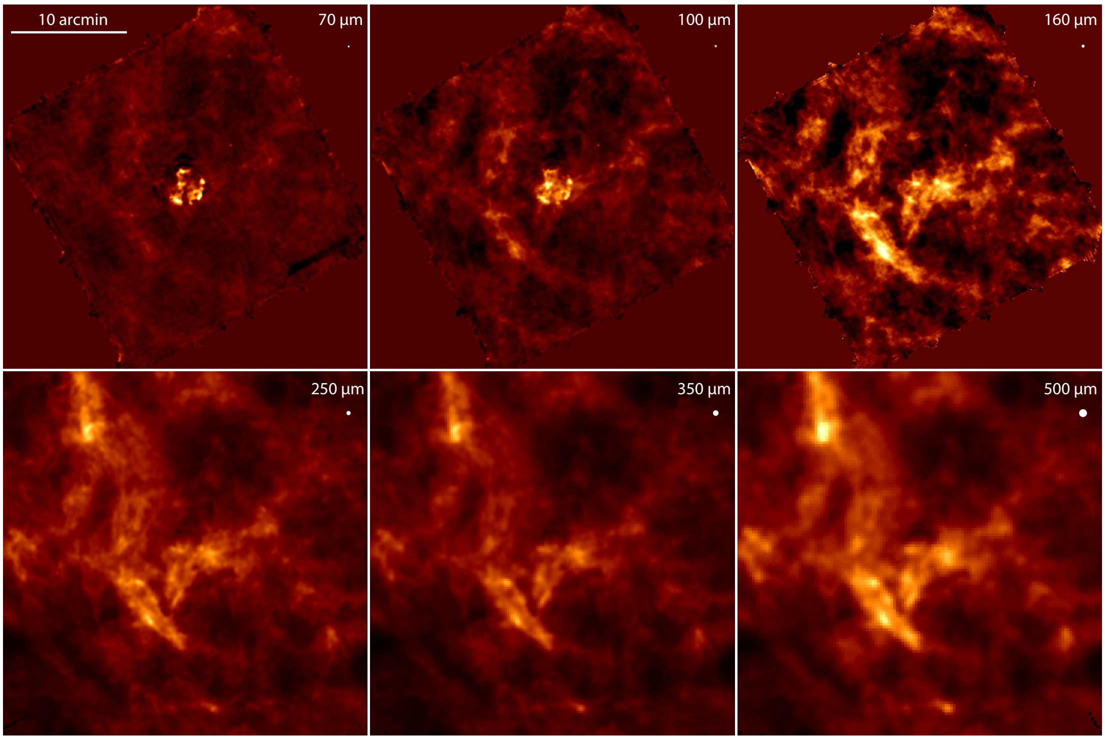

Figure 4.5: *Herschel* images (as in Fig. 4.1) after subtraction of the non-thermal synchrotron and the shocked warm-dust emission components. PACS bands (toprow) are convolved to a common 160 µm resolution of 12″ (FWHM). The morphologies in the 70 and 100 µm image correspond very closely and feature the least contamination by diffuse interstellar emission, as evident in the longer wavelength channels.

at 160 µm was still subtracted while applying the ratios. Consecutively a scaled image of the cool component at 70 µm (where the emission line and ISM contamination is lowest) was subtracted from the 160 µm map iteratively, until its visible imprint was minimized. This so obtained 160 µm ISM map was then used again to iteratively acquire more accurate 70 and 100 µm images of the cool SN dust component.

The resulting 70 µm cool SN dust image was then used again to determine the contribution to the longer wavelength PACS and SPIRE bands (the 70 µm image was convolved to the respective resolutions) by scaled subtraction until the visual imprint was minimized. At 350 and 500 µm this component was not detected anymore. The resulting flux density estimates for the cool supernova dust are given in the penultimate row of Table 4.1, along with the estimates for the cold interstellar dust in the last row, which is the remaining flux within the 165″ aperture around Cas A. The relative uncertainties of the individual emission components are smaller than the absolute calibration uncertainties associated with the total flux densities.

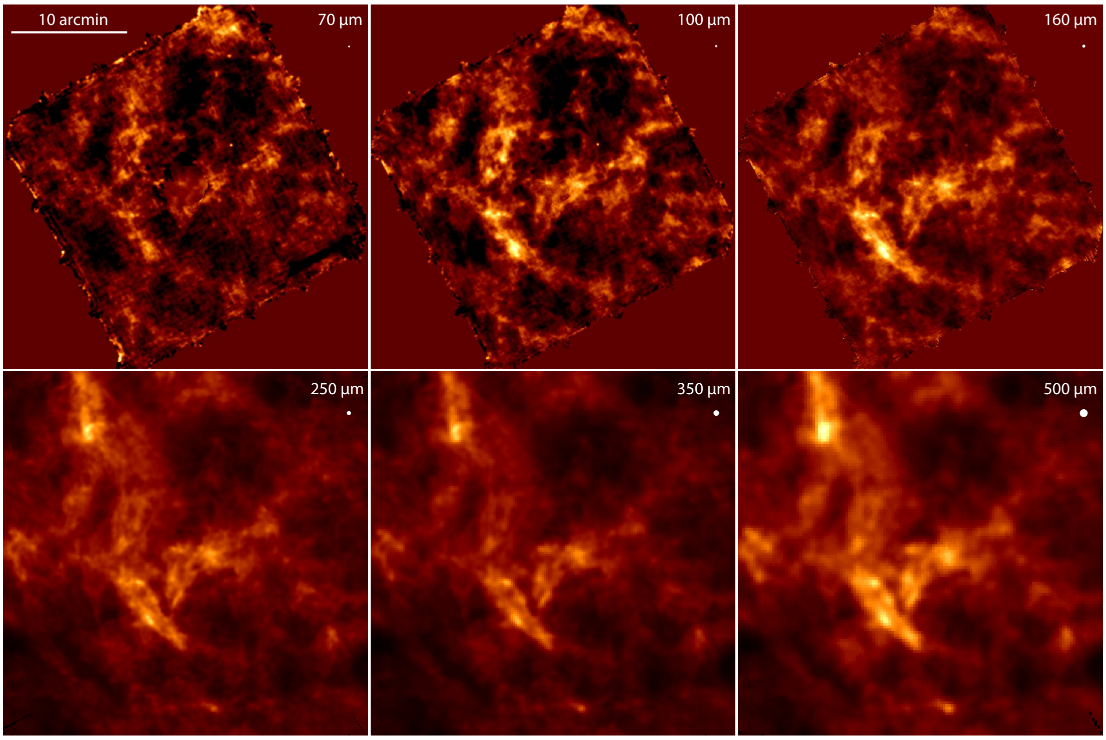

Figure 4.6: *Herschel* images (as in Fig. 4.1) after subtraction of the non-thermal synchrotron, the shocked warm-dust and the cold supernova dust emission components. PACS bands are convolved to a common 160 µm resolution of 12″ (FWHM). All wavelength channels feature the same diffuse emission morphology from interstellar clouds.

4.4 Discussion: The Cold Supernova Dust Component

Following the subtraction of emission from the non-thermal synchrotron, the shocked warm dust and the cold interstellar medium components, the 100 µm image (shown in Figure 4.7) shows a similar morphology as the cold supernova dust image at 70 µm. These represent the first resolved images of such a cold supernova dust component inside Cas A, which was first inferred by ISOPHOT observations by Tuffs et al. (2005) and AKARI/BLAST observations by Sibthorpe et al. (2010).

Figure 4.8 shows simple spectral energy distribution (SED) fits to the individual dust components from Table 4.1. The flux $F_{\nu,i}$ of each component i can be approximated by a single-temperature modified blackbody, as

$$F_{\nu,i} = \xi_i \, \nu^{\beta_i} \, B_\nu(T_{\rm dust})_i, \tag{4.4}$$

expect for the non-thermal synchrotron emission component, which is fitted as in equation 4.2. Here, ξ is a scale factor, related to the total dust mass of the particular component, $B_\nu(T_{\rm dust})$ the Planck-function for a certain dust temperature $T_{\rm dust}$ and $\beta = d \ln \kappa / d \ln \nu$ is the opacity spectral index, which depends on a multitude of factors,

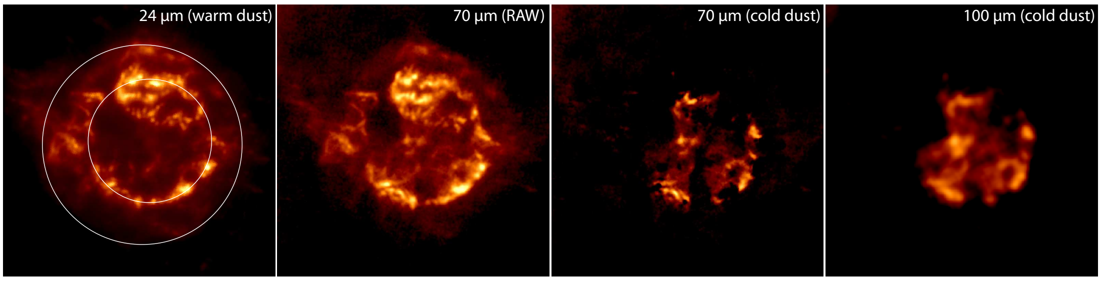

Figure 4.7: The shocked warm and unshocked cold dust components of Cas A.
Left: The MIPS 24 µm image resembles the emission from shocked warm dust. Its emission peaks at the position of the reverse shock and fades towards the outer forward shock. The newly obtained PACS 70 µm images (2nd from left) features more emission within the reverse shock. Its outer morphology is similar to the MIPS 24 µm image.
Right: After subtraction of a scaled MIPS 24 µm image from the PACS 70 µm image, the cold dust component is revealed. Its emission is only present within the position of the reverse shock. The 100 µm image shows the same cold dust morphology as the processed 70 µm cold dust image.

including the grain-composition and its size distribution (Draine 2006, and references therein). As this study only examines the far-infrared SED, and conditions inside Cas A likely harbor small grains (Nozawa et al. 2010), a spectral index of $\beta = 2$ was chosen.

The shocked warm dust component is fitted by an 82 K modified blackbody, as described in Hines et al. (2004, and private communications). The cold supernova dust component can be fitted by a dust temperature of 35 ± 3 K, while the superimposed cold interstellar dust component is well described by a 17 K model. For comparison the *COBE* average ISM spectrum by Dwek et al. (1997) is shown, including its 1σ uncertainty limits.

It can be seen that the 2–4 $M_\odot$, 18 K, $\beta = 0.9$ dust component (plotted as a dotted purple line in Figure 4.8), inferred by Dunne et al. (2003), can be ruled out by the high-resolution *Herschel* observations and the here described emission component disentanglement. The emission of such a component would have been detected in the SPIRE bands on top of the warm dust and non-thermal components, which is not the case. Their reported SCUBA fluxes arise from the non-thermal synchrotron emission as well as from superimposed interstellar dust along the line of sight.

Since thermal emission by dust and its underlying dust mass M_{dust} are related by

$$M_{\mathrm{dust}} = F_\nu D^2 / \kappa_\nu B_\nu(T_{\mathrm{dust}}) \tag{4.5}$$

it is possible to derive a physical dust mass for the cold supernova dust emission component. Using a distance $D = 3400$ pc (Fesen et al. 2006) and $\kappa_{160\mu m} = 9.8\,\mathrm{cm}^2\mathrm{g}^{-1}$ (Dorschner et al. 1995b) this component can be best fitted by $0.075 \pm 0.03\,M_\odot$ dust of temperature 35 ± 3 K.

The inferred mass is comparable to the cool dust mass ($0.055\,M_\odot$, at 33 K – with the use of the here applied mass absorption coefficient this mass would increase to

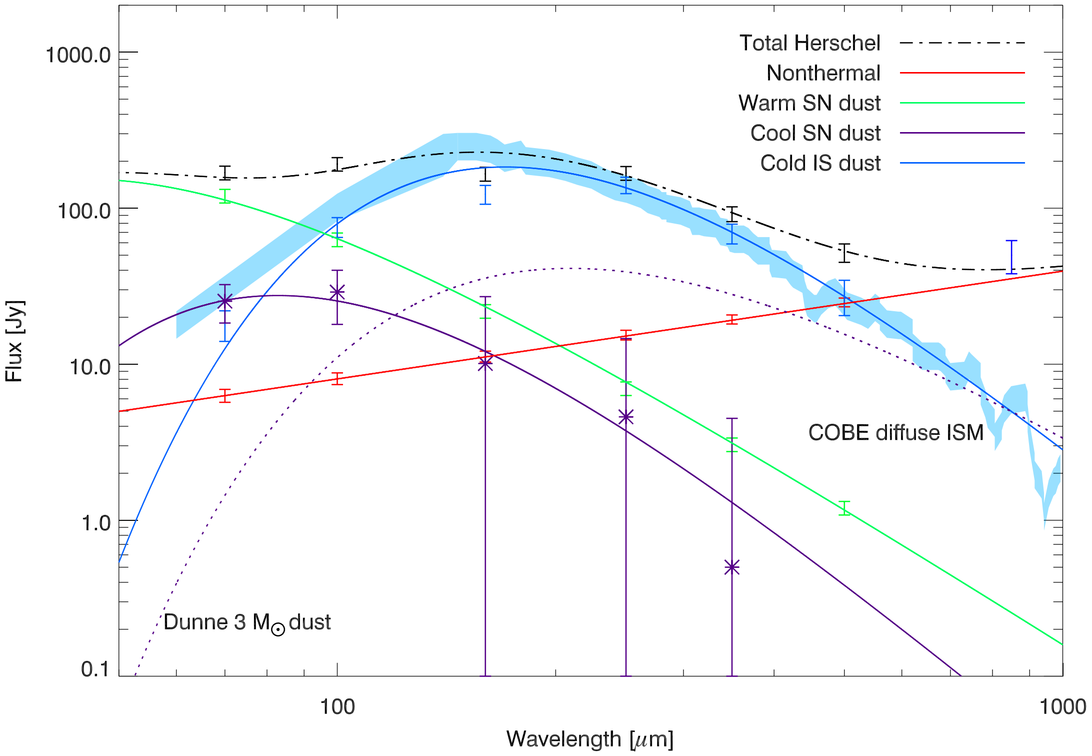

Figure 4.8: Derived far-infrared spectral energy distribution of the emission components observed towards Cas A.
Red: non-thermal flux densities are estimated as illustrated in Fig. 4.3;
Green: shocked warm dust component;
Blue: flux densities for the cold interstellar dust component, with a 17 K modified black body fit. For comparison the COBE average ISM spectrum by Dwek et al. (1997) is plotted in turquoise (area shows the quoted 1σ uncertainty limit).
Purple: the derived flux densities for the unshocked cool supernova dust component, together with a 35 K modified blackbody fit.
Black: total PACS and SPIRE flux densities measured towards Cas A. The dot-dashed black line corresponds to the sum of the fits to the non-thermal, warm dust, cool dust and cold interstellar dust component.
Dotted purple line: the presence of a 2–4 $M_\odot$, 18 K, $\beta = 0.9$ dust component component as proposed by Dunne et al. (2003) can be excluded, when noting the superposed cold interstellar dust emission component.

0.066 $M_\odot$) derived by Sibthorpe et al. (2010). The use of different mass absorption coefficients (for example those derived by Li and Draine 2001, Dorschner et al. 1995b or Jäger et al. 2009b) can pose a large amount of uncertainty, so that the actual value might be different by a factor of three.

In a recent dust formation model for hydrogen-poor Type IIb supernovae, Nozawa et al. (2010) modeled the Cas A explosion based on physical supernova explosion models and observations by *Spitzer* (Hines et al. 2004). They predict an initial condensation of

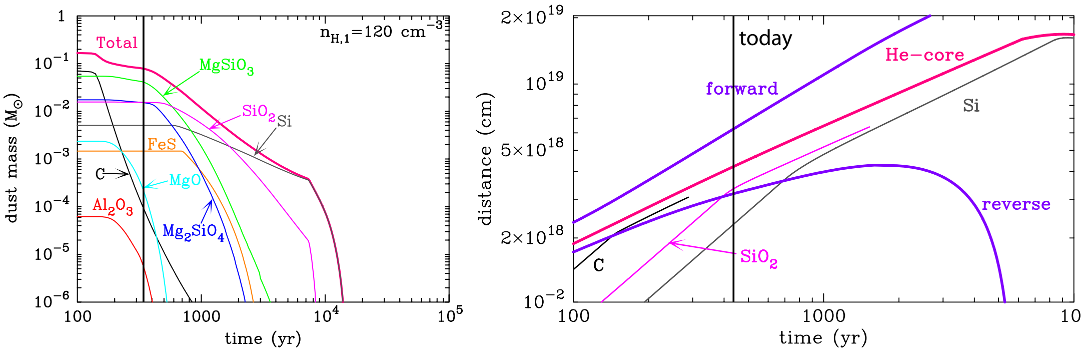

Figure 4.9: *Left*: Time evolution of the mass of the dust components inside the Cas A SNR running into its circumstellar medium with a density profile of $\rho \propto r^2$ for $n_{\mathrm{H},1} = 120\ \mathrm{cm}^{-3}$. Today, about half of the initially produced dust mass is already destroyed by the passage of the reverse shock. *Right*: Time evolution of the positions of different grain species and the trajectories of the forward and reverse shocks in Type IIb supernova remnants. Figures from Nozawa et al. (2010).

about 0.17 $\mathrm{M}_\odot$ of freshly formed dust in the first 300–700 days after the explosion. Due to the low gas density in the He core of such supernovae, the resulting average grain sizes are smaller than 0.01 µm. In the following expansion phase into the sourrounding circumstellar medium and upon encountering the reverse shock, the dust grains decouple from the gas and enter an area of hot plasma between the forward and reverse shock, where they quickly get heated up and destroyed by the plasma (see Figure 4.9). For an age of the supernova remnant of 330–340 years (appropriate to the condition in Cas A), Nozawa predicts that about 0.1 $\mathrm{M}_\odot$ – about half – of freshly formed dust is already destroyed by the encounter of the reverse shock. The remaining 0.072 $\mathrm{M}_\odot$ should then reside within the boundaries of the reverse shock.

This model is in good agreement with the observations made by *Herschel*. All of the detected cold dust is observed inside of the reverse shock, while the shocked warm dust is within the inter-shock region.

Only if the 0.072 $\mathrm{M}_\odot$ of cold dust was protected by very dense clumps, it could survive the 5 000 km/s encounter with the reverse shock. If most of the dust was eventually destroyed, as already predicted by the models from Nozawa et al., then supernovae of this type would not make a significant contribution to the dust content of the ISM, and could even diminish it.

4.5 Improvement Suggestions

In order to refine and improve the here described results, a number of follow-up suggestions can be made. For a better determination of the overall offset with respect to an absolutely calibrated map a complete pixel by pixel comparison with *DIRBE* data could be performed by bootstrapping as shown by Gomez et al. (2012). This should be done on newly reduced PACS images using the scan-amorphous technique, which recovers diffuse extended emission by the surrounding ISM clouds much better than the early-use MadMAP reduction.

The subtraction of the warm dust component could also be improved by allowing varying temperatures. Dust grains directly at the reverse shock front are hotter (∼ 120 K) than in the inter-plasma region (70-80 K). Continuum data within a *Spitzer*-IRS data cube could be used to derive such dust temperatures. Additionally the use of *SOFIA*-Forcast data at 31.5 µm as a warm dust subtraction template and the temperature information from IRS could resolve uncertainties induced by using the *Spitzer*-MIPS 24 µm image, which still contains some contamination from the [O IV] 25.89 µm and [Fe II] 25.99 µm lines (∼ 3%).

PACS and SPIRE spectroscopy can determine the amount and location of ejecta emission lines as well as the contribution from molecular CO emission from the superposed interstellar clouds within the photometry channels.

4.6 Conclusions

Utilizing the high spatial resolution and sensitivity of the photometric *Herschel* bands, it was possible to disentangle a variety of mid- and far infrared emission components within and towards the supernova remnant Cassiopeia A. Next to the previously established shocked warm dust and non-thermal synchrotron emission components, it was possible, for the first time, to resolve and separate an unshocked cold dust component, despite the dominant confusion by interstellar clouds along the line of sight. Figure 4.10 illustrates the superposition of the three dust components.

While total physical dust masses still remain uncertain, owing ambiguous dust models and uncertainties in absolute calibration, the relative dust content and the resolved spatial distribution of the components are a key result of this study. In concordance with evolutionary models of supernova explosions, freshly formed cold dust resides in the supernova ejecta *within* the region of the reverse shock. Upon the encounter with the reverse shock, dust grains get heated up and destroyed by electrons from the hot plasma between the forward and reverse shocks. This is affirmed by the fact that only hot dust grains are found in the inter-shock region, but no cold grains.

The relative masses of the hot and cold dust component suggests that the bulk of dust still belongs to the cold unshocked component, however it is greatly diluted in comparison to the total expected dust mass output for such a supernova explosion (cut in half, as predicted for the dynamical age of 330 years of Cas A). Only a few percent of dust grains survive the encounter by the reverse shock and get heated up to form the shocked warm dust component. Most of this hot dust is at the position of the reverse shock and gets subsequentially nearly completely destroyed – as seen in the fading of the warm dust in the 24 µm image in the inter-shock region.

If some of the remaining cold dust is not embedded and protected by dense clumps it would also be destroyed before an injection into the ISM could occur – this makes supernovae of Type IIb, as observed here, not a likely dust polluter of the ISM. In fact, the propagation of the supernova blast wave into the surrounding ISM could even dilute its dust contend, making such core-collapse supernovae efficient dust *destroyers*.

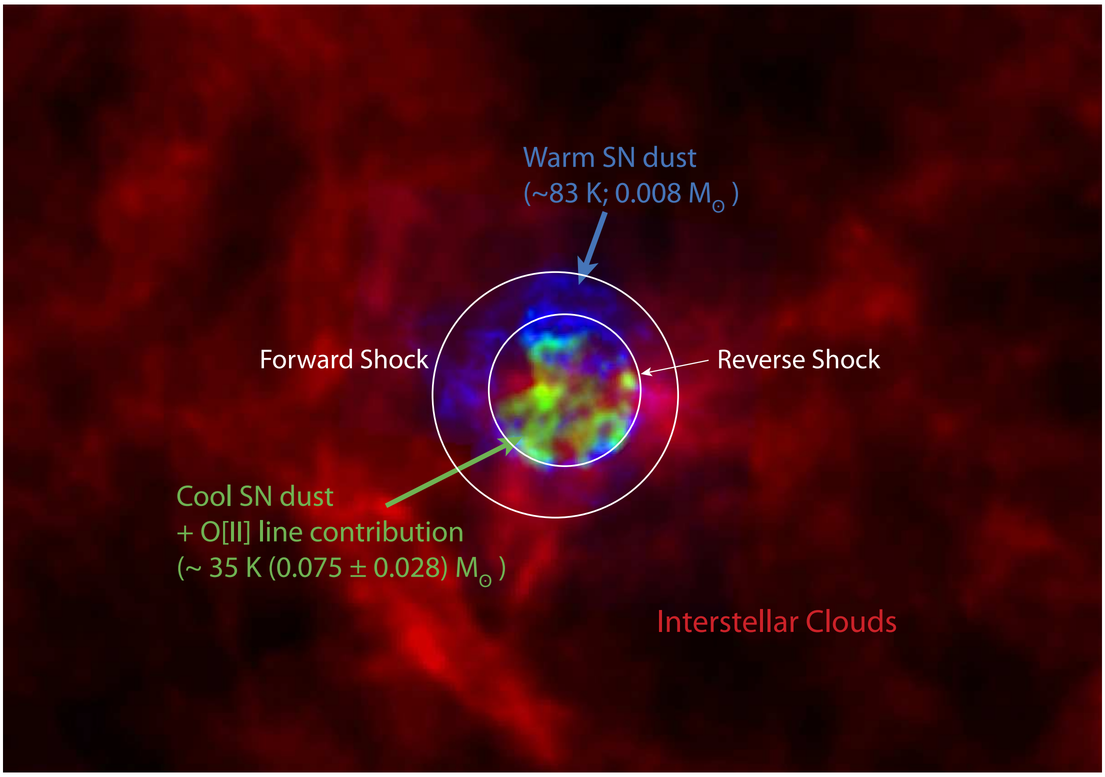

Figure 4.10: Disentangled mid- and far-infrared emission components in a three color representation. Interstellar clouds in-front of the remnant appear *red*. Shocked ejecta dust (*blue*) is situated within the forward shock, while a previously unseen unshocked, cold, dust component (*green*) sits within the reverse shock. It is likely that most of this unshocked dust will get destroyed when overrun by the reverse shock.

4.6.1 Results from Other Recent Dust Studies in SNRs

4.6.1.1 The Dust Content of the Type Ia SNe Tychos and Kepler

In Gomez et al. (2012) we do not find any evidence for cold supernova dust within the Type Ia supernova remnants Tycho and Kepler[3] using a similar approach as the one applied on Cas A with *Herschel* imagery. Only hot swept-up circumstellar dust, which was formed in the winds of the precessing Asymptotic Giant Branch (AGB) phase and the common envelope evolution phase, is seen in the near- and mid-infrared *Spitzer* images as a warm shocked dust component of mass $\sim 3.1 \times 10^{-3}\,M_\odot$ (Tycho) and $8.6 \times 10^{-3}\,\mathrm{M}_\odot$ (Kepler). Previously inferred substantial dust masses ($0.3 - 1\,\mathrm{M}_\odot$ for Kepler, Morgan et al. 2003) could be ruled out and attributed to interstellar clouds along the line of sight.

These observations suggest that also Type Ia supernovae are not producing substantial masses of dust in their ejecta and within the uncertainty limits are also not showing the amount of dust masses in the hot shocked component as expected from supernova

---

[3] The supernova type of Kepler is still controversial, as discussed in section 2)

evolutionary models by Nozawa et al. (2011). This hints supernovae of this type are very inefficient dust producers and/or are very efficient in destroying dust.

4.6.1.2 The Dust Content of SN1987A

SN1987A is one of the best studied core-collapse supernova, due its temporal and spatial proximity in the Large Magellanic Cloud. The progenitor star is believed to have a similar mass as Cas A ($18 - 20\,\mathrm{M}_\odot$; Arnett et al. 1989). Dust condensation was first observed within the ejecta between day 450 and 600 after the explosion in probably dense clumps ($\geq 10^{-4}\,\mathrm{M}_\odot$; Whitelock et al. 1989). However, due to the lack of far-infrared observations at this time, it was not possible to detect cold unshocked ejecta dust. Using *Herschel* Matsuura et al. (2011) claim to detect $0.5\,\mathrm{M}_\odot$ cold 20 K dust from the ejecta. Higher resolution studies with APEX at 350 and 870 µm by Lakicevic et al. (2012) confine this emission component to within $8''$ of the ejecta position. Due to a more recent synchrotron emission analysis and different dust models they claim only $0.01 - 0.2\,\mathrm{M}_\odot$ of dust.

Both authors claim that the presence of such dust quantities is sufficient to explain the dust masses in high-redshift galaxies. This statement should be considered with care, as they do not account for subsequent dust destruction by shocks. At an age of just 25 years, the extend of the forward shock region of SN 1987A is just 30 000 AU, or $0.6''$ (Racusin et al. 2009), much too small to be resolved with *Herschel* or APEX. Much, if not all, of the observed dust could be destroyed by the passage of shocks within the ejecta in the following thousands of years.

Future high resolution observations with an extended ALMA configuration could provide further clues about the position and quantities of the observed dust within SN1987A.

4.6.2 The Origin of Dust in High-Redshift Galaxies

Recapitulatory it is evident that core-collapse supernova explosions of massive stars initially produce some amount of dust. The following passage of the supernova shocks, however, likely destroys most, if not all, of the freshly produced dust. Additionally, the propagation of the supernova blast wave into the surrounding ISM efficiently destroys large quantities of dust. Draine (2003) estimates that each supernova can destroy $\sim 10\,\mathrm{M}_\odot$ of dust in the ISM; much more than any supernova can generate.

These results are in contradiction with theories where supernovae are responsible to provide the observed amount of dust in the early Universe.

On the other side, studies of presolar grains, extracted from the Murchison meteorite, show signatures of grain material which *must* have formed in supernova explosions (Hoppe and Zinner 2000; Hoppe et al. 2012). Among the evidences are Xe atoms trapped in nanodiamonds (which make out about 0.05% of the meteorite), and SiC grains of "Type X", which include abundances of ^{44}Ti at the time of grain formation (0.06 parts-per-million). These elements form just a tiny fraction of the entire meteoritic mass, but provide clear evidence that at least some parts must have formed from the ejecta of Type II supernovae.

In the literature it is a much too less considered fact that dust injection into the ISM is only a part of the story. Interstellar dust is continuously processed and the bulk of dust grains must have formed *within* the interstellar medium itself (Draine 2009; Draine and Salpeter 1979). It is estimated that stardust only accounts for $\sim 4\%$ of the interstellar dust mass. Grain growth by collisions of "seed" grains with other metal atoms can take place over relatively short timescales ($\sim 2 \times 10^5$ years) in ordinary HI clouds (Draine 2009).

Evidently, supernovae are required to produce a tiny amount of dust, which probably survives the propagation of the shocks when protected in very dense clumps, as "seeds" for further grain growth by collisions with other metal atoms in the ISM. This process alone is sufficient to explain the high dust reservoirs observed in the very early Universe and does not need artificially high supernova dust yields or changing dust physics throughout the lifetime of the Universe.

Observations of very late supernova remnants, when the reverse shock passed through the inner ejecta some 1 000 – 10 000 years after the explosion, could provide further insides on the amount of surviving seed-dust grains; however, the identification of dust associated with such supernovae will be very difficult, as the expected amount is very low and those remnants are very dispersed and will appear interwoven with the surrounding ISM and foreground cirrus structures.

5 Summary and Conclusions

In the first part of my studies I focused on the search for light echoes with the ultimate goal to perform postum classifications of various historical supernovae and possibly gain insights into their explosion mechanisms by explosion spectra from different reflection angles.

A wide-field survey around Kepler's supernova remnant has been performed in optical bands. While the method was successfully validated with observations of known echoes around Tycho, it was not possible to identify light echoes from Kepler, and thus I was not able to pursue spectroscopy for an identification of Kepler's supernova type and its progenitor.

Optical scattered light echoes tend to have relatively low surface brightnesses and may therefore be hard to find, especially when superimposed on bright field stars. In contrast, the thermal re-radiation of infrared echoes is very bright when compared to surrounding cirrus structures in the mid-infrared. With the intermediate release of preliminary data from the *WISE* infrared all-sky survey, I shifted my focus to the search for infrared echoes.

By chance, *WISE* started its all-sky survey near the supernova remnant Cassiopeia A, where infrared echoes have already been observed with *Spitzer*. While analyzing the multi-band *WISE* data, I identified a technique to systematically search for infrared echoes based on their intrinsic [22]-[12] color. The illumination of the echoing dust cloud by the supernova outburst heats and processes the dust content of the clouds so that their infrared color changes with respect to standard interstellar dust. With this technique it was possible to trace faint, yet unknown, infrared echoes to distances $> 800\,\mathrm{pc}$ away from the supernova remnant (as I commence the conclusions of this thesis, the echo nature of the most distant source has been confirmed, as two-epoch difference imaging from recently released final data from *WISE* unambiguously depicted the movement of the light flash).

Using this new method I searched large regions around other historical supernova remnants (namely Crab, Kepler, Tycho and SN 1181) and identified possible infrared echoes. These echo candidates allow systematic searches for their optical counterparts in the future, to ultimately receive spectral information about the supernova explosion and link the late type properties of these supernova remnants with the insights gained from spectroscopic and photometric observations of actual explosions.

As light echoes not only contain information about the radiation event itself, but also about the material which reflects and emits the echo, I concentrated a second part of my thesis to the study of the underlying structures.

In a collaboration with F. Vogt, we analyzed the infrared spectrum of a bright echo region. The spectrum shows the signatures of heated dust grains by the UV and optical outburst of the Cas A supernova explosion. Additionally, it differs from the emission by standard interstellar dust, as it shows dehydrogenated and destroyed PAH molecules. We conclude that the UV outburst of the supernova could provide a mechanism to explain these signatures of dust processing and destruction.

Light echoes allow three dimensional studies of the general interstellar medium. By using both, large-scale infrared survey observations and high-resolution optical imaging, it is possible to uniformly probe structures ranging over more than four orders of magnitude, down to size scales of several hundred AU's. As the expanding light outburst from the supernova acts as a short "flash light", it is possible to gain access to pristine interstellar material, which has not yet been processed by continuous radiation from nearby UV sources.

By comparing light echo observations with high-resolution numerical simulations of interstellar atomic hydrogen, I find that these observations resemble the turbulent flow structure of the ISM, in which structures are self similar across all covered scales from over 200 pc to less than 2000 AU. The echoing clouds are fragmented into dense substructures, which are connected to each other by filaments of intermediate density. The structures are usually very elongated. The three-dimensional analysis shows that most features are in fact sheet-like, as expected for structures formed in colliding turbulent flows. The derived density field of the light echoes is consistent with an origin of the emission in the densest parts of the cold neutral medium. Some regions suggest an origin in shocked layers of the CNM. Such structures may represent the building blocks for the onset of star formation in modern theories. Observations of light echoes can therefore give crucial constraints onto the initial condition of star formation.

An important question in theories including turbulence regards the origin and kinetic input of turbulent flows. Maps of light echoes show huge voids with no dense CNM structures, which are roughly elliptical in shape. After a three-dimensional disentanglement, these voids can represent the intersection of spherical shells with the light echo ellipsoid. Determining the center of such spheres could ultimately unveil local sources of the turbulent flows.

On a side note it is also worth mentioning that the presence of turbulence induced shocks within the CNM structures might be an alternate mechanism to account for the observed PAH dehydrogenation and dust destruction in the analyzed echo spectrum. In such a scenario the observed properties would be intrinsic to the echoing clouds and are not induced by the supernova UV radiation burst and could represent a dissipation scale of turbulence.

A third part, mostly unrelated to light echoes, but rather insightful study revealed the impact of shocks in supernovae on their dust content. Using the high-resolution far infrared capabilities of *Herschel*, it was possible to disentangle superposed emission components in the Cassiopeia A supernova remnant. For the first time it was possible to spatially resolve a cool, unshocked dust component. It's position within the region of the reverse shock suggests that dust forms in the ejecta of core-collapse supernovae, but the following passage of the reverse shock likely destroys most of this freshly formed dust. According to theories, about half of the initially produced dust is already destroyed at the current dynamical age of ~ 330 years.

Observers of supernovae should caution when they claim supernova explosions are responsible for producing the massive amounts of dust observed in galaxies in the early Universe. They should always consider the dynamical age of such explosions at the time of observations. The early spectra and light curves of supernovae only trace a short time of several years after the explosion, a time scale which is governed by dust condensation in the ejecta. Only observations of old supernova remnants can show their significance as dust polluters.

As of today, no observations of large amounts of surviving dust masses have been found in any supernova remnant. Massive dust production by supernovae is however not necessary to explain dust in high-redshift sources. Trace amounts of surviving dust grains are adequate for future grain growth in the dense parts of the interstellar medium, where a small fraction of supernova dust acts as seed grains.

This study therefore delivers an important input to the longstanding controversial issue of supernovae as massive dust production factories. This and future concentrated research on the exact dust production mechanisms in the ISM and the survival of seed dust grains after the passage of shocks might be crucial to solve this important question.

5.1 Light Echoes from a Galactic Perspective

Figures 5.1 and 5.2 illustrate the positions and geometries of the light echo observations from a Galactic perspective. The presentation of the Galactic structure is an illustration based on HI and recent *Spitzer* data. Details, like the exact positions of individual stars and nebulae, should not be seen as absolute, but rather as a good guess of the current understanding of the large scale Galactic structure. The illustration is more accurate close to the sun than far away.

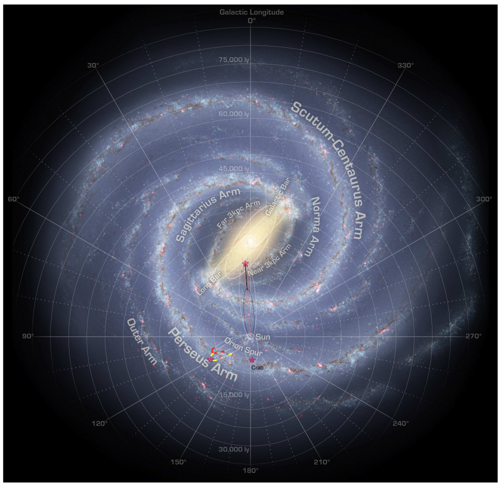

Figure 5.1: Illustration of the large scale structure in our Milky Way. The sun is located in the center of the Galactic coordinate system. This sketch has been modified from the original work of R. Hurt and R. Benjamin at the University of Wisconsin-Whitewater (Churchwell et al. 2009).

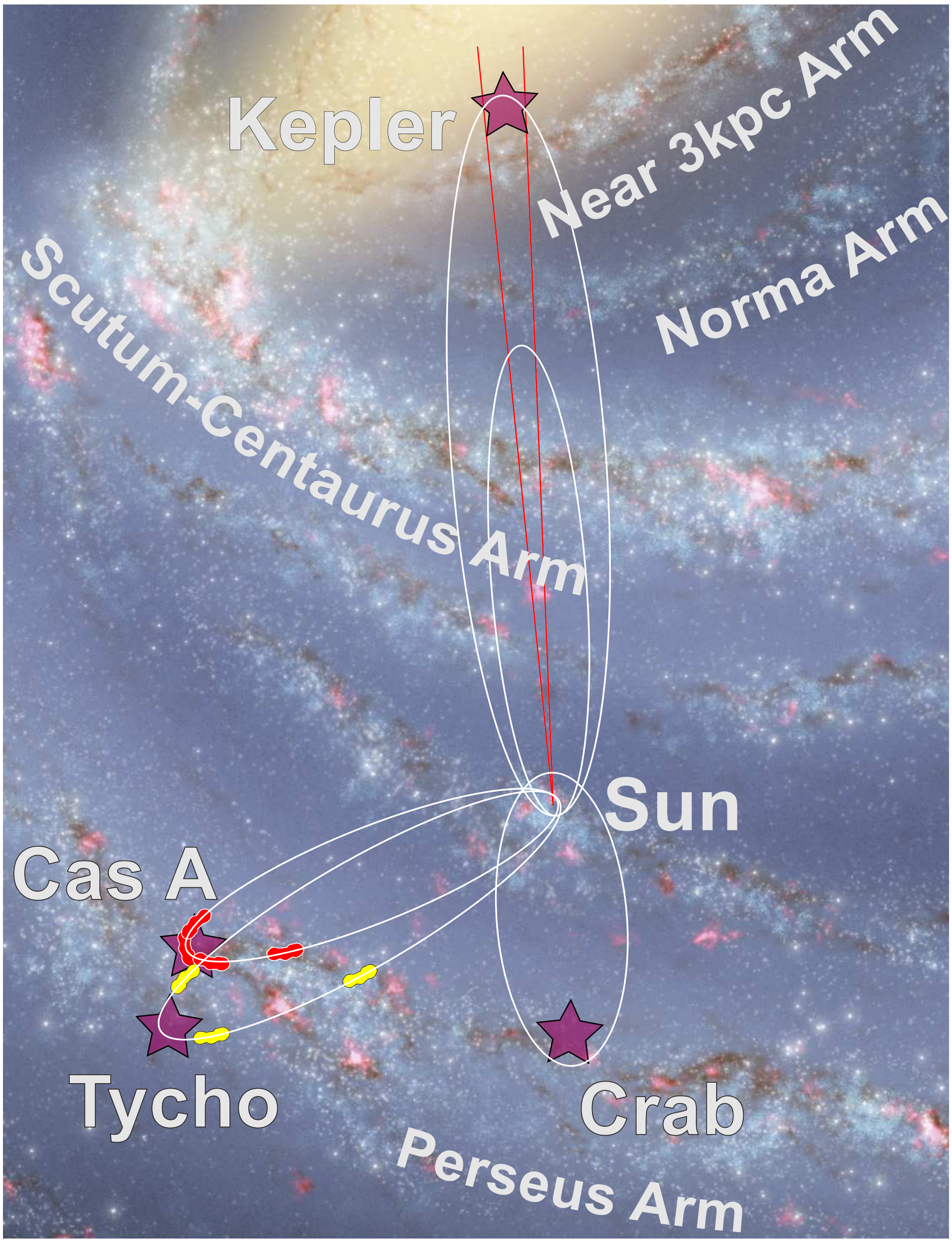

Figure 5.2: Light echoes in their Galactic environment. Close-up view from Figure 5.1 on structures near the sun with imprinted positions of the probed supernova remnants and their respective light echo ellipsoids. Positions of infrared and scattered light echoes from Cas A and Tycho are plotted as red and yellow clouds. As the distance to Kepler is uncertain, the light echo ellipsoids for the lower and upper estimate are plotted. The field of view from the optical search of chapter 2.1 (red lines intersecting with ellipsoid) does not probe significant parts of the spiral arms were all other light echoes form Cas A and Tycho have been found.

If we take a closer look at the light echo ellipsoids around Cas A and Tycho and plot the observed echo structures, it is evident that all echoes are part of the Perseus spiral arm. Light echoes are nearly found across the entire ellipsoid where it intersects structures in this galactic arm. The distribution ends abruptly at the border of the Perseus arm. This is consistent with my interpretation of light echoes being part of the cold neutral medium, which is not present (or much less abundant) in the inter-arm regions of the Milky Way, where nearly all CNM structures and molecular clouds are found within the spiral arms.

In retrospective, the non-detection of any light echoes from Kepler comes as no surprise as we look at the region probed by the performed optical survey. Since Kepler is probably the explosion of a runaway star, high above the Galactic plane ($\sim 500\,\mathrm{pc}$), the solid angle probed by the survey does not feature an intersection of the light echo ellipsoid with any spiral arms – and herewith likely places for dense CNM structures which could give rise to light echoes.

To eventually find light echoes around Kepler and other ancient Galactic supernovae, the observational search strategy should be redefined to concentrate the surveys to the possible intersections of the light echo ellipsoids with the known large scale structure of the Milky Way.

Table 5.1: Intersections of LE ellipsoid with Galactic Arms

Galactic Arm	6 kpc		4 kpc	
	west	east	west	east
Near 3 kpc	+4 – +5	-3 – -4	–	–
Norma	+7 – +9	−7 – −9	–	–
Scutum-Centaurus	+11 – +16	-12 – -18	+4 – +9	-5 – -10

Notes – Galactic longitude range of intersections of Kepler's light echo ellipsoids with spiral arms of the Milky Way.

For Keplers SNR the possible locations of those intersections are listed in Table 5.1. As the distance to Kepler is still not determined with high accuracy, I give the intersections for the two most cited distance scales. It might be worth noting that the light echo candidates listed in Table 2.7 are approximately at the position of the Norma Arm intersection, in a scenario where Kepler is located at a distance of 6 kpc from the sun. The quick-look at the *WISE* preliminary data from chapter 2.3 did only cover a 12° × 12° area and hence did not probe the possible intersections with other spiral arms.

Under the same considerations, the region I searched for echo candidates around the Crab Nebula completely covers the structures in the Perseus arm and a rapid analysis of the *WISE* final release data set should be started to immediately search for their optical counterparts.

Future of Light Echo Observations

Light echoes have proven to be an extremely helpful phenomenon to study various current questions in astronomy. Future studies will greatly benefit from the recently released *WISE* all-sky survey. The positions of infrared echoes will enable pointed searches to discover new scattered light echoes for spectral classifications of various supernovae and spectra under different scattering angles will possible reveal anisotropies in their explosion mechanisms.

In addition to three dimensional mapping of the turbulent interstellar medium, future observations of light echoes may also give new insight to stellar feedback. With the combination of data from *IRAS*, *Spitzer* and *WISE* it should be possible to three dimensionally map the turbulent flow field in the further vicinity of Cas A to infer the origin and sources of local interstellar turbulence. An analysis of the isolated echoing structures within the inferred bubbles, might also provide insights to to survival of dust in the presence of winds or after the passage of shocks.

While infrared observing capabilities are very limited until the launch of *JWST* (or until significant improvements of SOFIA), scattered light observations will benefit from the upcoming LSST in $\sim$ 2014, which should be able to detect all observable light echoes on the southern hemisphere. The new constraints on positions and properties of the echoing clouds from this study will help to identify them in such an extensive data set.

…
And the end of all our exploring
Will be to arrive where we started
And know the place for the first time.”

T. S. Eliot, Four Quartets, Little Gidding, V

Bibliography

F. Aharonian, A. G. Akhperjanian, U. Barres de Almeida, A. R. Bazer-Bachi, B. Behera, M. Beilicke, W. Benbow, D. Berge, K. Bernlöhr, C. Boisson, O. Bolz, V. Borrel, I. Braun, E. Brion, J. Brucker, R. Bühler, T. Bulik, I. Büsching, T. Boutelier, S. Carrigan, P. M. Chadwick, L.-M. Chounet, A. C. Clapson, G. Coignet, R. Cornils, L. Costamante, M. Dalton, B. Degrange, H. J. Dickinson, A. Djannati-Ataï, W. Domainko, L. O'C. Drury, F. Dubois, G. Dubus, J. Dyks, K. Egberts, D. Emmanoulopoulos, P. Espigat, C. Farnier, F. Feinstein, A. Fiasson, A. Förster, G. Fontaine, M. Füßling, Y. A. Gallant, B. Giebels, J. F. Glicenstein, B. Glück, P. Goret, C. Hadjichristidis, D. Hauser, M. Hauser, G. Heinzelmann, G. Henri, G. Hermann, J. A. Hinton, A. Hoffmann, W. Hofmann, M. Holleran, S. Hoppe, D. Horns, A. Jacholkowska, O. C. de Jager, I. Jung, K. Katarzyński, E. Kendziorra, M. Kerschhaggl, B. Khélifi, D. Keogh, N. Komin, K. Kosack, G. Lamanna, I. J. Latham, M. Lemoine-Goumard, J.-P. Lenain, T. Lohse, J. M. Martin, O. Martineau-Huynh, A. Marcowith, C. Masterson, D. Maurin, T. J. L. McComb, R. Moderski, E. Moulin, M. Naumann-Godo, M. de Naurois, D. Nedbal, D. Nekrassov, S. J. Nolan, S. Ohm, J.-P. Olive, E. de Oña Wilhelmi, K. J. Orford, J. L. Osborne, M. Ostrowski, M. Panter, G. Pedaletti, G. Pelletier, P.-O. Petrucci, S. Pita, G. Pühlhofer, M. Punch, A. Quirrenbach, B. C. Raubenheimer, M. Raue, S. M. Rayner, M. Renaud, J. Ripken, L. Rob, S. Rosier-Lees, G. Rowell, B. Rudak, J. Ruppel, V. Sahakian, A. Santangelo, R. Schlickeiser, F. M. Schöck, R. Schröder, U. Schwanke, S. Schwarzburg, S. Schwemmer, A. Shalchi, H. Sol, D. Spangler, Ł. Stawarz, R. Steenkamp, C. Stegmann, G. Superina, P. H. Tam, J.-P. Tavernet, R. Terrier, C. van Eldik, G. Vasileiadis, C. Venter, J. P. Vialle, P. Vincent, M. Vivier, H. J. Völk, F. Volpe, S. J. Wagner, M. Ward, A. A. Zdziarski, and A. Zech. HESS upper limits for Kepler's supernova remnant. *A&A*, 488:219–223, September 2008. doi: 10.1051/0004-6361:200809401.

R. G. Arendt, E. Dwek, and S. H. Moseley. Newly Synthesized Elements and Pristine Dust in the Cassiopeia A Supernova Remnant. *ApJ*, 521:234–245, August 1999. doi: 10.1086/307545.

W. D. Arnett, J. N. Bahcall, R. P. Kirshner, and S. E. Woosley. Supernova 1987A. *ARA&A*, 27:629–700, 1989. doi: 10.1146/annurev.aa.27.090189.003213.

D. Baade, K. Meisenheimer, O. Iwert, J. Alonso, T. Augusteijn, J. Beletic, H. Bellemann, W. Benesch, A. Böhm, H. Böhnhardt, J. Brewer, S. Deiries, B. Delabre, R. Donaldson, C. Dupuy, P. Franke, R. Gerdes, A. Gilliotte, B. Grimm, N. Haddad, G. Hess, G. Ihle, R. Klein, R. Lenzen, J.-L. Lizon, D. Mancini, N. Münch, A. Pizarro, P. Prado, G. Rahmer, J. Reyes, F. Richardson, E. Robledo, F. Sanchez, A. Silber, P. Sinclaire, R. Wackermann, and S. Zaggia. The Wide Field Imager at the 2.2-m

MPG/ESO telescope: first views with a 67-million-facette eye. *The Messenger*, 95: 15–16, March 1999.

W. Baade. Nova Ophiuchi of 1604 AS a Supernova. *ApJ*, 97:119, March 1943. doi: 10.1086/144505.

R. Bandiera. The origin of Kepler's supernova remnant. *ApJ*, 319:885–892, August 1987. doi: 10.1086/165505.

M. J. Barlow, O. Krause, B. M. Swinyard, B. Sibthorpe, M.-A. Besel, R. Wesson, R. J. Ivison, L. Dunne, W. K. Gear, H. L. Gomez, P. C. Hargrave, T. Henning, S. J. Leeks, T. L. Lim, G. Olofsson, and E. T. Polehampton. A Herschel PACS and SPIRE study of the dust content of the Cassiopeia A supernova remnant. *A&A*, 518:L138, July 2010. doi: 10.1051/0004-6361/201014585.

E. E. Becklin, A. G. G. M. Tielens, R. D. Gehrz, and H. H. S. Callis. Stratospheric Observatory for Infrared Astronomy (SOFIA). In *Society of Photo-Optical Instrumentation Engineers (SPIE) Conference Series*, volume 6678 of *Society of Photo-Optical Instrumentation Engineers (SPIE) Conference Series*, October 2007. doi: 10.1117/12.735903.

F. Bertoldi, C. L. Carilli, P. Cox, X. Fan, M. A. Strauss, A. Beelen, A. Omont, and R. Zylka. Dust emission from the most distant quasars. *A&A*, 406:L55–L58, July 2003. doi: 10.1051/0004-6361:20030710.

M.-A. Besel and O. Krause. Observations of infrared echoes around Cassiopeia A with WISE. *A&A*, 541:L3, May 2012. doi: 10.1051/0004-6361/201219082.

W. P. Blair, P. Ghavamian, K. S. Long, B. J. Williams, K. J. Borkowski, S. P. Reynolds, and R. Sankrit. Spitzer Space Telescope Observations of Kepler's Supernova Remnant: A Detailed Look at the Circumstellar Dust Component. *ApJ*, 662:998–1013, June 2007. doi: 10.1086/518414.

S. I. Blinnikov, R. Eastman, O. S. Bartunov, V. A. Popolitov, and S. E. Woosley. A Comparative Modeling of Supernova 1993J. *ApJ*, 496:454, March 1998. doi: 10.1086/305375.

M. F. Bode and A. Evans. Infrared emission by dust grains near variable primary sources. III - Type II supernovae. *MNRAS*, 193:21P–24P, October 1980.

Franois Boulanger. Dust evolution in the star forming turbulent interstellar medium. *Proceedings of the International Astronomical Union*, 2 (Symposium S237):47–52, 2006. doi: 10.1017/S1743921307001202. URL `http://dx.doi.org/10.1017/S1743921307001202`.

C. M. Cantalupo, J. D. Borrill, A. H. Jaffe, T. S. Kisner, and R. Stompor. MADmap: A Massively Parallel Maximum Likelihood Cosmic Microwave Background Map-maker. *ApJS*, 187:212–227, March 2010. doi: 10.1088/0067-0049/187/1/212.

B. W. Carroll and D. A. Ostlie. *An introduction to modern astrophysics and cosmology.* July 2006.

G. Cassam-Chenaï, A. Decourchelle, J. Ballet, U. Hwang, J. P. Hughes, R. Petre, and et al. XMM-Newton observation of Kepler's supernova remnant. *A&A*, 414:545–558, February 2004. doi: 10.1051/0004-6361:20031551.

R. A. Chevalier. The scattered light echo of a supernova. *ApJ*, 308:225–231, September 1986. doi: 10.1086/164492.

E. Churchwell, B. L. Babler, M. R. Meade, B. A. Whitney, R. Benjamin, R. Indebetouw, C. Cyganowski, T. P. Robitaille, M. Povich, C. Watson, and S. Bracker. The Spitzer/GLIMPSE Surveys: A New View of the Milky Way. *PASP*, 121:213–230, March 2009. doi: 10.1086/597811.

J. R. Dawson, N. M. McClure-Griffiths, A. Kawamura, N. Mizuno, T. Onishi, A. Mizuno, and Y. Fukui. Supershells as Molecular Cloud Factories: Parsec Resolution Observations of H I and ^{12}CO(J = 1-0) in GSH 287+04-17 and GSH 277+00+36. *ApJ*, 728:127, February 2011. doi: 10.1088/0004-637X/728/2/127.

J. M. Dickey, E. E. Salpeter, and Y. Terzian. Temperature Distribution of Neutral Hydrogen at High Galactic Latitudes. *ApJ*, 211:L77, January 1977. doi: 10.1086/182345.

N. H. Dieter, W. J. Welch, and M. C. H. Wright. H2O masers and H II regions in W49 at 23 GHz. *ApJ*, 230:768–770, June 1979. doi: 10.1086/157135.

D. Docenko and R. A. Sunyaev. Fine-structure infrared lines from the Cassiopeia A knots. *A&A*, 509:A59, January 2010. doi: 10.1051/0004-6361/200810366.

J. Dorschner, C. Friedemann, J. Guertler, and W. W. Duley. Laboratory spectra of protosilicates and the interstellar silicate absorption bands. *Ap&SS*, 68:159–174, March 1980. doi: 10.1007/BF00641652.

J. Dorschner, B. Begemann, T. Henning, C. Jaeger, and H. Mutschke. Steps toward interstellar silicate mineralogy. II. Study of Mg-Fe-silicate glasses of variable composition. *A&A*, 300:503, August 1995a.

J. Dorschner, B. Begemann, T. Henning, C. Jaeger, and H. Mutschke. Steps toward interstellar silicate mineralogy. II. Study of Mg-Fe-silicate glasses of variable composition. *A&A*, 300:503, August 1995b.

B. Draine. On the Interpretation of the λ 2175 Å Feature. In L. J. Allamandola and A. G. G. M. Tielens, editors, *Interstellar Dust*, volume 135 of *IAU Symposium*, page 313, 1989.

B. T. Draine. Interstellar Dust Grains. *ARA&A*, 41:241–289, 2003. doi: 10.1146/annurev.astro.41.011802.094840.

B. T. Draine. On the Submillimeter Opacity of Protoplanetary Disks. *ApJ*, 636:1114–1120, January 2006. doi: 10.1086/498130.

B. T. Draine. Interstellar Dust Models and Evolutionary Implications. In T. Henning, E. Grün, & J. Steinacker, editor, *Cosmic Dust - Near and Far*, volume 414 of *Astronomical Society of the Pacific Conference Series*, page 453, December 2009.

B. T. Draine and H. M. Lee. Optical properties of interstellar graphite and silicate grains. *ApJ*, 285:89–108, October 1984. doi: 10.1086/162480.

B. T. Draine and A. Li. Infrared Emission from Interstellar Dust. IV. The Silicate-Graphite-PAH Model in the Post-Spitzer Era. *ApJ*, 657:810–837, March 2007. doi: 10.1086/511055.

B. T. Draine and E. E. Salpeter. Destruction mechanisms for interstellar dust. *ApJ*, 231:438–455, July 1979. doi: 10.1086/157206.

L. Dunne, S. Eales, R. Ivison, H. Morgan, and M. Edmunds. Type II supernovae as a significant source of interstellar dust. *Nature*, 424:285–287, July 2003. doi: 10.1038/nature01792.

E. Dwek. The infrared echo of a type II supernova with a circumstellar dust shell - Applications to SN 1979c and SN 1980k. *ApJ*, 274:175–183, November 1983. doi: 10.1086/161435.

E. Dwek. The infrared echo of Type II supernovae with circumstellar dust shells. II - A probe into the presupernova evolution of the progenitor star. *ApJ*, 297:719–723, October 1985. doi: 10.1086/163571.

E. Dwek, R. G. Arendt, D. J. Fixsen, T. J. Sodroski, N. Odegard, J. L. Weiland, W. T. Reach, M. G. Hauser, T. Kelsall, S. H. Moseley, R. F. Silverberg, R. A. Shafer, J. Ballester, D. Bazell, and R. Isaacman. Detection and Characterization of Cold Interstellar Dust and Polycyclic Aromatic Hydrocarbon Emission, from COBE Observations. *ApJ*, 475:565, February 1997. doi: 10.1086/303568.

E. Dwek, F. Galliano, and A. P. Jones. The Evolution of Dust in the Early Universe with Applications to the Galaxy SDSS J1148+5251. *ApJ*, 662:927–939, June 2007. doi: 10.1086/518430.

J. A. Ennis, L. Rudnick, W. T. Reach, J. D. Smith, J. Rho, T. DeLaney, H. Gomez, and T. Kozasa. Spitzer IRAC Images and Sample Spectra of Cassiopeia A's Explosion. *ApJ*, 652:376–386, November 2006. doi: 10.1086/508142.

T. Erben, M. Schirmer, J. P. Dietrich, O. Cordes, L. Haberzettl, M. Hetterscheidt, H. Hildebrandt, O. Schmithuesen, P. Schneider, P. Simon, E. Deul, R. N. Hook, N. Kaiser, M. Radovich, C. Benoist, M. Nonino, L. F. Olsen, I. Prandoni, R. Wichmann, S. Zaggia, D. Bomans, R. J. Dettmar, and J. M. Miralles. GaBoDS: The Garching-Bonn Deep Survey. IV. Methods for the image reduction of multi-chip cameras demonstrated on data from the ESO Wide-Field Imager. *Astronomische Nachrichten*, 326:432–464, July 2005. doi: 10.1002/asna.200510396.

K. A. Eriksen, D. Arnett, D. W. McCarthy, and P. Young. The Reddening Toward Cassiopeia A's Supernova: Constraining the ^{56}Ni Yield. *ApJ*, 697:29–36, May 2009. doi: 10.1088/0004-637X/697/1/29.

H. I. Ewen and E. M. Purcell. Observation of a Line in the Galactic Radio Spectrum: Radiation from Galactic Hydrogen at 1,420 Mc./sec. *Nature*, 168:356, September 1951. doi: 10.1038/168356a0.

R. A. Fesen, M. C. Hammell, J. Morse, R. A. Chevalier, K. J. Borkowski, M. A. Dopita, C. L. Gerardy, S. S. Lawrence, J. C. Raymond, and S. van den Bergh. The Expansion Asymmetry and Age of the Cassiopeia A Supernova Remnant. *ApJ*, 645:283–292, July 2006. doi: 10.1086/504254.

G. B. Field, D. W. Goldsmith, and H. J. Habing. Cosmic-Ray Heating of the Interstellar Gas. *ApJ*, 155:L149, March 1969. doi: 10.1086/180324.

C. L. Gerardy and R. A. Fesen. Near-Infrared Spectroscopy of the Cassiopeia A and Kepler Supernova Remnants. *AJ*, 121:2781–2791, May 2001. doi: 10.1086/320393.

H. L. Gomez, C. J. R. Clark, T. Nozawa, O. Krause, E. L. Gomez, M. Matsuura, M. J. Barlow, M.-A. Besel, L. Dunne, W. K. Gear, P. Hargrave, T. Henning, R. J. Ivison, B. Sibthorpe, B. M. Swinyard, and R. Wesson. Dust in historical Galactic Type Ia supernova remnants with Herschel. *MNRAS*, 420:3557–3573, March 2012. doi: 10.1111/j.1365-2966.2011.20272.x.

K. D. Gordon, G. H. Rieke, C. W. Engelbracht, J. Muzerolle, J. A. Stansberry, K. A. Misselt, J. E. Morrison, J. Cadien, E. T. Young, H. Dole, D. M. Kelly, A. Alonso-Herrero, E. Egami, K. Y. L. Su, C. Papovich, P. S. Smith, D. C. Hines, M. J. Rieke, M. Blaylock, P. G. Pérez-González, E. Le Floc'h, J. L. Hinz, W. B. Latter, T. Hesselroth, D. T. Frayer, A. Noriega-Crespo, F. J. Masci, D. L. Padgett, M. P. Smylie, and N. M. Haegel. Reduction Algorithms for the Multiband Imaging Photometer for Spitzer. *PASP*, 117:503–525, May 2005. doi: 10.1086/429309.

E. V. Gotthelf, B. Koralesky, L. Rudnick, T. W. Jones, U. Hwang, and R. Petre. Chandra Detection of the Forward and Reverse Shocks in Cassiopeia A. *ApJ*, 552: L39–L43, May 2001. doi: 10.1086/320250.

R. J. Gould and E. E. Salpeter. The Interstellar Abundance of the Hydrogen Molecule. I. Basic Processes. *ApJ*, 138:393, August 1963. doi: 10.1086/147654.

M. J. Griffin, A. Abergel, A. Abreu, P. A. R. Ade, P. André, J.-L. Augueres, T. Babbedge, Y. Bae, T. Baillie, J.-P. Baluteau, M. J. Barlow, G. Bendo, D. Benielli, J. J. Bock, P. Bonhomme, D. Brisbin, C. Brockley-Blatt, M. Caldwell, C. Cara, N. Castro-Rodriguez, R. Cerulli, P. Chanial, S. Chen, E. Clark, D. L. Clements, L. Clerc, J. Coker, D. Communal, L. Conversi, P. Cox, D. Crumb, C. Cunningham, F. Daly, G. R. Davis, P. de Antoni, J. Delderfield, N. Devin, A. di Giorgio, I. Didschuns, K. Dohlen, M. Donati, A. Dowell, C. D. Dowell, L. Duband, L. Dumaye, R. J. Emery, M. Ferlet, D. Ferrand, J. Fontignie, M. Fox, A. Franceschini, M. Frerking, T. Fulton, J. Garcia, R. Gastaud, W. K. Gear, J. Glenn, A. Goizel, D. K.

Griffin, T. Grundy, S. Guest, L. Guillemet, P. C. Hargrave, M. Harwit, P. Hastings, E. Hatziminaoglou, M. Herman, B. Hinde, V. Hristov, M. Huang, P. Imhof, K. J. Isaak, U. Israelsson, R. J. Ivison, D. Jennings, B. Kiernan, K. J. King, A. E. Lange, W. Latter, G. Laurent, P. Laurent, S. J. Leeks, E. Lellouch, L. Levenson, B. Li, J. Li, J. Lilienthal, T. Lim, S. J. Liu, N. Lu, S. Madden, G. Mainetti, P. Marliani, D. McKay, K. Mercier, S. Molinari, H. Morris, H. Moseley, J. Mulder, M. Mur, D. A. Naylor, H. Nguyen, B. O'Halloran, S. Oliver, G. Olofsson, H.-G. Olofsson, R. Orfei, M. J. Page, I. Pain, P. Panuzzo, A. Papageorgiou, G. Parks, P. Parr-Burman, A. Pearce, C. Pearson, I. Pérez-Fournon, F. Pinsard, G. Pisano, J. Podosek, M. Pohlen, E. T. Polehampton, D. Pouliquen, D. Rigopoulou, D. Rizzo, I. G. Roseboom, H. Roussel, M. Rowan-Robinson, B. Rownd, P. Saraceno, M. Sauvage, R. Savage, G. Savini, E. Sawyer, C. Scharmberg, D. Schmitt, N. Schneider, B. Schulz, A. Schwartz, R. Shafer, D. L. Shupe, B. Sibthorpe, S. Sidher, A. Smith, A. J. Smith, D. Smith, L. Spencer, B. Stobie, R. Sudiwala, K. Sukhatme, C. Surace, J. A. Stevens, B. M. Swinyard, M. Trichas, T. Tourette, H. Triou, S. Tseng, C. Tucker, A. Turner, M. Vaccari, I. Valtchanov, L. Vigroux, E. Virique, G. Voellmer, H. Walker, R. Ward, T. Waskett, M. Weilert, R. Wesson, G. J. White, N. Whitehouse, C. D. Wilson, B. Winter, A. L. Woodcraft, G. S. Wright, C. K. Xu, A. Zavagno, M. Zemcov, L. Zhang, and E. Zonca. The Herschel-SPIRE instrument and its in-flight performance. *A&A*, 518:L3, July 2010. doi: 10.1051/0004-6361/201014519.

M. A. T. Groenewegen, C. Waelkens, M. J. Barlow, F. Kerschbaum, P. Garcia-Lario, J. Cernicharo, J. A. D. L. Blommaert, J. Bouwman, M. Cohen, N. Cox, L. Decin, K. Exter, W. K. Gear, H. L. Gomez, P. C. Hargrave, T. Henning, D. Hutsemékers, R. J. Ivison, A. Jorissen, O. Krause, D. Ladjal, S. J. Leeks, T. L. Lim, M. Matsuura, Y. Nazé, G. Olofsson, R. Ottensamer, E. Polehampton, T. Posch, G. Rauw, P. Royer, B. Sibthorpe, B. M. Swinyard, T. Ueta, C. Vamvatira-Nakou, B. Vandenbussche, G. C. van de Steene, S. van Eck, P. A. M. van Hoof, H. van Winckel, E. Verdugo, and R. Wesson. MESS (Mass-loss of Evolved StarS), a Herschel key program. *A&A*, 526:A162, February 2011. doi: 10.1051/0004-6361/201015829.

T. Güver and F. Özel. The relation between optical extinction and hydrogen column density in the Galaxy. *MNRAS*, 400:2050–2053, December 2009. doi: 10.1111/j.1365-2966.2009.15598.x.

J. Hartmann. Investigations on the spectrum and orbit of delta Orionis. *ApJ*, 19: 268–286, May 1904. doi: 10.1086/141112.

L. Hartmann, J. Ballesteros-Paredes, and E. A. Bergin. Rapid Formation of Molecular Clouds and Stars in the Solar Neighborhood. *ApJ*, 562:852–868, December 2001. doi: 10.1086/323863.

C. Heiles. H I shells and supershells. *ApJ*, 229:533–537, April 1979. doi: 10.1086/156986.

C. Heiles and T. H. Troland. The Millennium Arecibo 21 Centimeter Absorption-Line Survey. II. Properties of the Warm and Cold Neutral Media. *ApJ*, 586:1067–1093, April 2003. doi: 10.1086/367828.

C. Heiles and T. H. Troland. The Millennium Arecibo 21 Centimeter Absorption-Line Survey. IV. Statistics of Magnetic Field, Column Density, and Turbulence. *ApJ*, 624: 773–793, May 2005. doi: 10.1086/428896.

P. Hennebelle and E. Audit. On the structure of the turbulent interstellar atomic hydrogen. I. Physical characteristics. Influence and nature of turbulence in a thermally bistable flow. *A&A*, 465:431–443, April 2007. doi: 10.1051/0004-6361:20066139.

P. Hennebelle and R. Teyssier. Magnetic processes in a collapsing dense core. II. Fragmentation. Is there a fragmentation crisis? *A&A*, 477:25–34, January 2008. doi: 10.1051/0004-6361:20078310.

T. L. Herter, J. D. Adams, J. M. De Buizer, G. E. Gull, J. Schoenwald, C. P. Henderson, L. D. Keller, T. Nikola, G. Stacey, and W. D. Vacca. First Science Observations with SOFIA/FORCAST: The FORCAST Mid-infrared Camera. *ApJ*, 749:L18, April 2012. doi: 10.1088/2041-8205/749/2/L18.

J. J. Hester. The Crab Nebula: An Astrophysical Chimera. *ARA&A*, 46:127–155, September 2008. doi: 10.1146/annurev.astro.45.051806.110608.

S. J. U. Higdon, D. Devost, J. L. Higdon, B. R. Brandl, J. R. Houck, P. Hall, D. Barry, V. Charmandaris, J. D. T. Smith, G. C. Sloan, and J. Green. The SMART Data Analysis Package for the Infrared Spectrograph on the Spitzer Space Telescope. *PASP*, 116:975–984, October 2004. doi: 10.1086/425083.

R. H. Hildebrand. The Determination of Cloud Masses and Dust Characteristics from Submillimetre Thermal Emission. *QJRAS*, 24:267, September 1983.

J. M. Hill, R. F. Green, and J. H. Slagle. The Large Binocular Telescope. In *Society of Photo-Optical Instrumentation Engineers (SPIE) Conference Series*, volume 6267 of *Society of Photo-Optical Instrumentation Engineers (SPIE) Conference Series*, July 2006. doi: 10.1117/12.669832.

D. C. Hines, G. H. Rieke, K. D. Gordon, J. Rho, K. A. Misselt, C. E. Woodward, M. W. Werner, O. Krause, W. B. Latter, C. W. Engelbracht, E. Egami, D. M. Kelly, J. Muzerolle, J. A. Stansberry, K. Y. L. Su, J. E. Morrison, E. T. Young, A. Noriega-Crespo, D. L. Padgett, R. D. Gehrz, E. Polomski, J. W. Beeman, and E. E. Haller. Imaging of the Supernova Remnant Cassiopeia A with the Multiband Imaging Photometer for Spitzer (MIPS). *ApJS*, 154:290–295, September 2004. doi: 10.1086/422583.

L. M. Hobbs, D. G. York, J. A. Thorburn, T. P. Snow, M. Bishof, S. D. Friedman, B. J. McCall, T. Oka, B. Rachford, P. Sonnentrucker, and D. E. Welty. Studies of the Diffuse Interstellar Bands. III. HD 183143. *ApJ*, 705:32–45, November 2009. doi: 10.1088/0004-637X/705/1/32.

P. Hoppe and E. Zinner. Presolar dust grains from meteorites and their stellar sources. *J. Geophys. Res.*, 105:10371–10386, May 2000. doi: 10.1029/1999JA900194.

P. Hoppe, W. Fujiya, and E. Zinner. Sulfur Molecule Chemistry in Supernova Ejecta Recorded by Silicon Carbide Stardust. *ApJ*, 745:L26, February 2012. doi: 10.1088/2041-8205/745/2/L26.

J. R. Houck, T. L. Roellig, J. van Cleve, W. J. Forrest, T. Herter, C. R. Lawrence, K. Matthews, H. J. Reitsema, B. T. Soifer, D. M. Watson, D. Weedman, M. Huisjen, J. Troeltzsch, D. J. Barry, J. Bernard-Salas, C. E. Blacken, B. R. Brandl, V. Charmandaris, D. Devost, G. E. Gull, P. Hall, C. P. Henderson, S. J. U. Higdon, B. E. Pirger, J. Schoenwald, G. C. Sloan, K. I. Uchida, P. N. Appleton, L. Armus, M. J. Burgdorf, S. B. Fajardo-Acosta, C. J. Grillmair, J. G. Ingalls, P. W. Morris, and H. I. Teplitz. The Infrared Spectrograph (IRS) on the Spitzer Space Telescope. *ApJS*, 154: 18–24, September 2004. doi: 10.1086/423134.

W. Huggins and W. A. Miller. On the Spectra of Some of the Nebulae. By William Huggins, F.R.A.S. A Supplement to the Paper ”On the Spectra of Some of the Fixed Stars William Huggins F.R.A.S., and W. A. Miller, M.D., LL.D., Treas. and V.P.P.S.”. *Royal Society of London Philosophical Transactions Series I*, 154:437–444, 1864.

Z. Ivezic, J. A. Tyson, E. Acosta, R. Allsman, S. F. Anderson, J. Andrew, R. Angel, T. Axelrod, J. D. Barr, A. C. Becker, J. Becla, C. Beldica, R. D. Blandford, J. S. Bloom, K. Borne, W. N. Brandt, M. E. Brown, J. S. Bullock, D. L. Burke, S. Chandrasekharan, S. Chesley, C. F. Claver, A. Connolly, K. H. Cook, A. Cooray, K. R. Covey, C. Cribbs, R. Cutri, G. Daues, F. Delgado, H. Ferguson, E. Gawiser, J. C. Geary, P. Gee, M. Geha, R. R. Gibson, D. K. Gilmore, W. J. Gressler, C. Hogan, M. E. Huffer, S. H. Jacoby, B. Jain, J. G. Jernigan, R. L. Jones, M. Juric, S. M. Kahn, J. S. Kalirai, J. P. Kantor, R. Kessler, D. Kirkby, L. Knox, V. L. Krabbendam, S. Krughoff, S. Kulkarni, R. Lambert, D. Levine, M. Liang, K. Lim, R. H. Lupton, P. Marshall, S. Marshall, M. May, M. Miller, D. J. Mills, D. G. Monet, D. R. Neill, M. Nordby, P. O'Connor, J. Oliver, S. S. Olivier, K. Olsen, R. E. Owen, J. R. Peterson, C. E. Petry, F. Pierfederici, S. Pietrowicz, R. Pike, P. A. Pinto, R. Plante, V. Radeka, A. Rasmussen, S. T. Ridgway, W. Rosing, A. Saha, T. L. Schalk, R. H. Schindler, D. P. Schneider, G. Schumacher, J. Sebag, L. G. Seppala, I. Shipsey, N. Silvestri, J. A. Smith, R. C. Smith, M. A. Strauss, C. W. Stubbs, D. Sweeney, A. Szalay, J. J. Thaler, D. Vanden Berk, L. Walkowicz, M. Warner, B. Willman, D. Wittman, S. C. Wolff, W. M. Wood-Vasey, P. Yoachim, H. Zhan, and for the LSST Collaboration. LSST: from Science Drivers to Reference Design and Anticipated Data Products. *ArXiv e-prints*, May 2008.

C. Jäger, H. Mutschke, T. Henning, and F. Huisken. Analogs of Cosmic Dust. In T. Henning, E. Grün, and J. Steinacker, editors, *Cosmic Dust - Near and Far*, volume 414 of *Astronomical Society of the Pacific Conference Series*, page 319, December 2009a.

C. Jäger, H. Mutschke, T. Henning, and F. Huisken. Analogs of Cosmic Dust. In T. Henning, E. Grün, & J. Steinacker, editor, *Cosmic Dust - Near and Far*, volume 414 of *Astronomical Society of the Pacific Conference Series*, page 319, December 2009b.

T. H. Jarrett, M. Cohen, F. Masci, E. Wright, D. Stern, D. Benford, A. Blain, S. Carey, R. M. Cutri, P. Eisenhardt, C. Lonsdale, A. Mainzer, K. Marsh, D. Padgett, S. Petty, M. Ressler, M. Skrutskie, S. Stanford, J. Surace, C. W. Tsai, S. Wheelock, and D. L. Yan. The Spitzer-WISE Survey of the Ecliptic Poles. *ApJ*, 735:112, July 2011. doi: 10.1088/0004-637X/735/2/112.

N. Kaiser, H. Aussel, B. E. Burke, H. Boesgaard, K. Chambers, M. R. Chun, J. N. Heasley, K.-W. Hodapp, B. Hunt, R. Jedicke, D. Jewitt, R. Kudritzki, G. A. Luppino, M. Maberry, E. Magnier, D. G. Monet, P. M. Onaka, A. J. Pickles, P. H. H. Rhoads, T. Simon, A. Szalay, I. Szapudi, D. J. Tholen, J. L. Tonry, M. Waterson, and J. Wick. Pan-STARRS: A Large Synoptic Survey Telescope Array. In J. A. Tyson and S. Wolff, editors, *Society of Photo-Optical Instrumentation Engineers (SPIE) Conference Series*, volume 4836 of *Society of Photo-Optical Instrumentation Engineers (SPIE) Conference Series*, pages 154–164, December 2002. doi: 10.1117/12.457365.

T. Kelsall, J. L. Weiland, B. A. Franz, W. T. Reach, R. G. Arendt, E. Dwek, H. T. Freudenreich, M. G. Hauser, S. H. Moseley, N. P. Odegard, R. F. Silverberg, and E. L. Wright. The COBE Diffuse Infrared Background Experiment Search for the Cosmic Infrared Background. II. Model of the Interplanetary Dust Cloud. *ApJ*, 508: 44–73, November 1998. doi: 10.1086/306380.

Y. Kim, G. H. Rieke, O. Krause, K. Misselt, R. Indebetouw, and K. E. Johnson. Structure of the Interstellar Medium around Cas A. *ApJ*, 678:287–296, May 2008. doi: 10.1086/533426.

R. Kippenhahn and A. Weigert. *Stellar Structure and Evolution.* 1994.

R. S. Klessen, F. Heitsch, and M.-M. Mac Low. Gravitational Collapse in Turbulent Molecular Clouds. I. Gasdynamical Turbulence. *ApJ*, 535:887–906, June 2000. doi: 10.1086/308891.

T. Kozasa, H. Hasegawa, and K. Nomoto. Formation of dust grains in the ejecta of SN 1987A. II. *A&A*, 249:474–482, September 1991.

T. Kozasa, T. Nozawa, N. Tominaga, H. Umeda, K. Maeda, and K. Nomoto. Dust in Supernovae: Formation and Evolution. In T. Henning, E. Grün, & J. Steinacker, editor, *Cosmic Dust - Near and Far*, volume 414 of *Astronomical Society of the Pacific Conference Series*, page 43, December 2009.

O. Krause, S. M. Birkmann, G. H. Rieke, D. Lemke, U. Klaas, D. C. Hines, and K. D. Gordon. No cold dust within the supernova remnant Cassiopeia A. *Nature*, 432: 596–598, December 2004. doi: 10.1038/nature03110.

O. Krause, G. H. Rieke, S. M. Birkmann, E. Le Floc'h, K. D. Gordon, E. Egami, J. Bieging, J. P. Hughes, E. T. Young, J. L. Hinz, S. P. Quanz, and D. C. Hines. Infrared Echoes near the Supernova Remnant Cassiopeia A. *Science*, 308:1604–1606, June 2005. doi: 10.1126/science.1112035.

O. Krause, S. M. Birkmann, T. Usuda, T. Hattori, M. Goto, G. H. Rieke, and K. A. Misselt. The Cassiopeia A Supernova Was of Type IIb. *Science*, 320:1195–, May 2008a. doi: 10.1126/science.1155788.

O. Krause, M. Tanaka, T. Usuda, T. Hattori, M. Goto, S. Birkmann, and K. Nomoto. Tycho Brahe's 1572 supernova as a standard typeIa as revealed by its light-echo spectrum. *Nature*, 456:617–619, December 2008b. doi: 10.1038/nature07608.

P. Kroupa. The Initial Mass Function of Stars: Evidence for Uniformity in Variable Systems. *Science*, 295:82–91, January 2002. doi: 10.1126/science.1067524.

M. Lakicevic, J. T. van Loon, T. Stanke, C. De Breuck, and F. Patat. Zooming in on Supernova 1987A at sub-mm wavelengths. *ArXiv e-prints*, March 2012.

V. Lebouteiller, J. Bernard-Salas, G. C. Sloan, and D. J. Barry. Advanced Optimal Extraction for the Spitzer/IRS. *PASP*, 122:231–240, February 2010. doi: 10.1086/650426.

A. Li and B. T. Draine. Infrared Emission from Interstellar Dust. II. The Diffuse Interstellar Medium. *ApJ*, 554:778–802, June 2001. doi: 10.1086/323147.

J.-F. Liu, J. N. Bregman, and P. Seitzer. A Scattered Light Echo around SN 1993J in M81. *ApJ*, 582:919–923, January 2003. doi: 10.1086/344719.

F. J. Lu, Q. D. Wang, M. Y. Ge, J. L. Qu, X. J. Yang, S. J. Zheng, and Y. Chen. The Single-degenerate Binary Origin of Tycho's Supernova as Traced by the Stripped Envelope of the Companion. *ApJ*, 732:11, May 2011. doi: 10.1088/0004-637X/732/1/11.

M.-M. Mac Low and R. S. Klessen. Control of star formation by supersonic turbulence. *Reviews of Modern Physics*, 76:125–194, January 2004. doi: 10.1103/RevModPhys.76.125.

A. Mainzer, J. Bauer, T. Grav, J. Masiero, R. M. Cutri, J. Dailey, P. Eisenhardt, R. S. McMillan, E. Wright, R. Walker, R. Jedicke, T. Spahr, D. Tholen, R. Alles, R. Beck, H. Brandenburg, T. Conrow, T. Evans, J. Fowler, T. Jarrett, K. Marsh, F. Masci, H. McCallon, S. Wheelock, M. Wittman, P. Wyatt, E. DeBaun, G. Elliott, D. Elsbury, T. Gautier, IV, S. Gomillion, D. Leisawitz, C. Maleszewski, M. Micheli, and A. Wilkins. Preliminary Results from NEOWISE: An Enhancement to the Wide-field Infrared Survey Explorer for Solar System Science. *ApJ*, 731:53, April 2011. doi: 10.1088/0004-637X/731/1/53.

J. S. Mathis, W. Rumpl, and K. H. Nordsieck. The size distribution of interstellar grains. *ApJ*, 217:425–433, October 1977. doi: 10.1086/155591.

M. Matsuura, E. Dwek, M. Meixner, M. Otsuka, B. Babler, M. J. Barlow, J. Roman-Duval, C. Engelbracht, K. Sandstrom, M. Lakićević, J. T. van Loon, G. Sonneborn, G. C. Clayton, K. S. Long, P. Lundqvist, T. Nozawa, K. D. Gordon, S. Hony, P. Panuzzo, K. Okumura, K. A. Misselt, E. Montiel, and M. Sauvage. Herschel Detects a Massive Dust Reservoir in Supernova 1987A. *Science*, 333:1258–, September 2011. doi: 10.1126/science.1205983.

R. McCray and M. Kafatos. Supershells and propagating star formation. *ApJ*, 317: 190–196, June 1987. doi: 10.1086/165267.

C. F. McKee and J. P. Ostriker. A theory of the interstellar medium - Three components regulated by supernova explosions in an inhomogeneous substrate. *ApJ*, 218:148–169, November 1977. doi: 10.1086/155667.

E. R. Micelotta, A. P. Jones, and A. G. G. M. Tielens. Polycyclic aromatic hydrocarbon processing in interstellar shocks. *A&A*, 510:A36, February 2010. doi: 10.1051/0004-6361/200911682.

M.-A. Miville-Deschênes and G. Lagache. IRIS: A New Generation of IRAS Maps. *ApJS*, 157:302–323, April 2005. doi: 10.1086/427938.

D. G. Monet, S. E. Levine, B. Canzian, H. D. Ables, A. R. Bird, C. C. Dahn, H. H. Guetter, H. C. Harris, A. A. Henden, S. K. Leggett, H. F. Levison, C. B. Luginbuhl, J. Martini, A. K. B. Monet, J. A. Munn, J. R. Pier, A. R. Rhodes, B. Riepe, S. Sell, R. C. Stone, F. J. Vrba, R. L. Walker, G. Westerhout, R. J. Brucato, I. N. Reid, W. Schoening, M. Hartley, M. A. Read, and S. B. Tritton. The USNO-B Catalog. *AJ*, 125:984–993, February 2003. doi: 10.1086/345888.

H. L. Morgan and M. G. Edmunds. Dust formation in early galaxies. *MNRAS*, 343: 427–442, August 2003. doi: 10.1046/j.1365-8711.2003.06681.x.

H. L. Morgan, L. Dunne, S. A. Eales, R. J. Ivison, and M. G. Edmunds. Cold Dust in Kepler's Supernova Remnant. *ApJ*, 597:L33–L36, November 2003. doi: 10.1086/379639.

H. Murakami, H. Baba, P. Barthel, D. L. Clements, M. Cohen, Y. Doi, K. Enya, E. Figueredo, N. Fujishiro, H. Fujiwara, M. Fujiwara, P. Garcia-Lario, T. Goto, S. Hasegawa, Y. Hibi, T. Hirao, N. Hiromoto, S. S. Hong, K. Imai, M. Ishigaki, M. Ishiguro, D. Ishihara, Y. Ita, W.-S. Jeong, K. S. Jeong, H. Kaneda, H. Kataza, M. Kawada, T. Kawai, A. Kawamura, M. F. Kessler, D. Kester, T. Kii, D. C. Kim, W. Kim, H. Kobayashi, B. C. Koo, S. M. Kwon, H. M. Lee, R. Lorente, S. Makiuti, H. Matsuhara, T. Matsumoto, H. Matsuo, S. Matsuura, T. G. Müller, N. Murakami, H. Nagata, T. Nakagawa, T. Naoi, M. Narita, M. Noda, S. H. Oh, A. Ohnishi, Y. Ohyama, Y. Okada, H. Okuda, S. Oliver, T. Onaka, T. Ootsubo, S. Oyabu, S. Pak, Y.-S. Park, C. P. Pearson, M. Rowan-Robinson, T. Saito, I. Sakon, A. Salama, S. Sato, R. S. Savage, S. Serjeant, H. Shibai, M. Shirahata, J. Sohn, T. Suzuki, T. Takagi, H. Takahashi, T. Tanabé, T. T. Takeuchi, S. Takita, M. Thomson, K. Uemizu, M. Ueno, F. Usui, E. Verdugo, T. Wada, L. Wang, T. Watabe, H. Watarai, G. J. White, I. Yamamura, C. Yamauchi, and A. Yasuda. The Infrared Astronomical Mission AKARI. *PASJ*, 59:369, October 2007.

G. Neugebauer, H. J. Habing, R. van Duinen, H. H. Aumann, B. Baud, C. A. Beichman, D. A. Beintema, N. Boggess, P. E. Clegg, T. de Jong, J. P. Emerson, T. N. Gautier, F. C. Gillett, S. Harris, M. G. Hauser, J. R. Houck, R. E. Jennings, F. J. Low, P. L. Marsden, G. Miley, F. M. Olnon, S. R. Pottasch, E. Raimond, M. Rowan-Robinson, B. T. Soifer, R. G. Walker, P. R. Wesselius, and E. Young. The Infrared Astronomical Satellite (IRAS) mission. *ApJ*, 278:L1–L6, March 1984. doi: 10.1086/184209.

M. Nonino, E. Bertin, L. da Costa, E. Deul, T. Erben, L. Olsen, I. Prandoni, M. Scodeggio, A. Wicenec, R. Wichmann, C. Benoist, W. Freudling, M. D. Guarnieri, I. Hook, R. Hook, R. Mendez, S. Savaglio, D. Silva, and R. Slijkhuis. ESO Imaging Survey. I. Description of the survey, data reduction and reliability of the data. *A&AS*, 137: 51–74, May 1999. doi: 10.1051/aas:1999473.

T. Nozawa, T. Kozasa, N. Tominaga, K. Maeda, H. Umeda, K. Nomoto, and O. Krause. Formation and Evolution of Dust in Type IIb Supernovae with Application to the Cassiopeia A Supernova Remnant. *ApJ*, 713:356–373, April 2010. doi: 10.1088/0004-637X/713/1/356.

T. Nozawa, K. Maeda, T. Kozasa, M. Tanaka, K. Nomoto, and H. Umeda. Formation of Dust in the Ejecta of Type Ia Supernovae. *ApJ*, 736:45, July 2011. doi: 10.1088/0004-637X/736/1/45.

T. Onaka, H. Matsuhara, T. Wada, N. Fujishiro, H. Fujiwara, M. Ishigaki, D. Ishihara, Y. Ita, H. Kataza, W. Kim, T. Matsumoto, H. Murakami, Y. Ohyama, S. Oyabu, I. Sakon, T. Tanabé, T. Takagi, K. Uemizu, M. Ueno, F. Usui, H. Watarai, M. Cohen, K. Enya, T. Ootsubo, C. P. Pearson, N. Takeyama, T. Yamamuro, and Y. Ikeda. The Infrared Camera (IRC) for AKARI – Design and Imaging Performance. *PASJ*, 59: 401, October 2007.

V. Ossenkopf and T. Henning. Dust opacities for protostellar cores. *A&A*, 291:943–959, November 1994.

S. Ott. The Herschel Data Processing System HIPE and Pipelines Up and Running Since the Start of the Mission. In Y. Mizumoto, K.-I. Morita, & M. Ohishi, editor, *Astronomical Data Analysis Software and Systems XIX*, volume 434 of *Astronomical Society of the Pacific Conference Series*, page 139, December 2010.

N. Panagia and K. W. Weiler. The absolute magnitude and the type classification of SN 1181 equals 3 C 58. *A&A*, 82:389–391, February 1980.

G. L. Pilbratt, J. R. Riedinger, T. Passvogel, G. Crone, D. Doyle, U. Gageur, A. M. Heras, C. Jewell, L. Metcalfe, S. Ott, and M. Schmidt. Herschel Space Observatory. An ESA facility for far-infrared and submillimetre astronomy. *A&A*, 518:L1, July 2010. doi: 10.1051/0004-6361/201014759.

J. S. Plaskett and J. A. Pearce. Determination of the K-term, the solar motion, and the galactic rotation from the radial velocities of 849 O to B7 stars. In *Publications of the American Astronomical Society*, volume 7 of *Publications of the American Astronomical Society*, pages 225–226, 1933.

A. Poglitsch, C. Waelkens, N. Geis, H. Feuchtgruber, B. Vandenbussche, L. Rodriguez, O. Krause, E. Renotte, C. van Hoof, P. Saraceno, J. Cepa, F. Kerschbaum, P. Agnèse, B. Ali, B. Altieri, P. Andreani, J.-L. Augueres, Z. Balog, L. Barl, O. H. Bauer, N. Belbachir, M. Benedettini, N. Billot, O. Boulade, H. Bischof, J. Blommaert, E. Callut, C. Cara, R. Cerulli, D. Cesarsky, A. Contursi, Y. Creten, W. De Meester, V. Doublier, E. Doumayrou, L. Duband, K. Exter, R. Genzel, J.-M. Gillis, U. Grözinger,

T. Henning, J. Herreros, R. Huygen, M. Inguscio, G. Jakob, C. Jamar, C. Jean, J. de Jong, R. Katterloher, C. Kiss, U. Klaas, D. Lemke, D. Lutz, S. Madden, B. Marquet, J. Martignac, A. Mazy, P. Merken, F. Montfort, L. Morbidelli, T. Müller, M. Nielbock, K. Okumura, R. Orfei, R. Ottensamer, S. Pezzuto, P. Popesso, J. Putzeys, S. Regibo, V. Reveret, P. Royer, M. Sauvage, J. Schreiber, J. Stegmaier, D. Schmitt, J. Schubert, E. Sturm, M. Thiel, G. Tofani, R. Vavrek, M. Wetzstein, E. Wieprecht, and E. Wiezorrek. The Photodetector Array Camera and Spectrometer (PACS) on the Herschel Space Observatory. *A&A*, 518:L2, July 2010. doi: 10.1051/0004-6361/201014535.

R. S. Priddey, K. G. Isaak, R. G. McMahon, E. I. Robson, and C. P. Pearson. Quasars as probes of the submillimetre cosmos at z 5 - I. Preliminary SCUBA photometry. *MNRAS*, 344:L74–L78, October 2003. doi: 10.1046/j.1365-8711.2003.07076.x.

J. L. Racusin, S. Park, S. Zhekov, D. N. Burrows, G. P. Garmire, and R. McCray. X-ray Evolution of SNR 1987A: The Radial Expansion. *ApJ*, 703:1752–1759, October 2009. doi: 10.1088/0004-637X/703/2/1752.

J. E. Reed, J. J. Hester, A. C. Fabian, and P. F. Winkler. The Three-dimensional Structure of the Cassiopeia A Supernova Remnant. I. The Spherical Shell. *ApJ*, 440: 706, February 1995. doi: 10.1086/175308.

D. E. Reichart and A. W. Stephens. The Fading of Supernova Remnant Cassiopeia A from 38 MHZ to 16.5 GHZ from 1949 to 1999 with New Observations at 1405 MHZ. *ApJ*, 537:904–908, July 2000. doi: 10.1086/309073.

A. Rest, D. L. Welch, N. B. Suntzeff, L. Oaster, H. Lanning, K. Olsen, R. C. Smith, A. C. Becker, M. Bergmann, P. Challis, A. Clocchiatti, K. H. Cook, G. Damke, A. Garg, M. E. Huber, T. Matheson, D. Minniti, J. L. Prieto, and W. M. Wood-Vasey. Scattered-Light Echoes from the Historical Galactic Supernovae Cassiopeia A and Tycho (SN 1572). *ApJ*, 681:L81–L84, July 2008. doi: 10.1086/590427.

A. Rest, R. J. Foley, B. Sinnott, D. L. Welch, C. Badenes, A. V. Filippenko, M. Bergmann, W. A. Bhatti, S. Blondin, P. Challis, G. Damke, H. Finley, M. E. Huber, D. Kasen, R. P. Kirshner, T. Matheson, P. Mazzali, D. Minniti, R. Nakajima, G. Narayan, K. Olsen, D. Sauer, R. C. Smith, and N. B. Suntzeff. Direct Confirmation of the Asymmetry of the Cas A Supernova with Light Echoes. *ApJ*, 732:3, May 2011. doi: 10.1088/0004-637X/732/1/3.

R. J. Reynolds, S. L. Tufte, L. M. Haffner, K. Jaehnig, and J. W. Percival. The Wisconsin H-alpha Mapper (WHAM): A brief review of performance characteristics and early scientific results. *PASP*, 15:14–18, April 1998.

S. P. Reynolds, K. J. Borkowski, D. A. Green, U. Hwang, I. Harrus, and R. Petre. The Youngest Galactic Supernova Remnant: G1.9+0.3. *ApJ*, 680:L41–L44, June 2008. doi: 10.1086/589570.

J. Rho, T. Kozasa, W. T. Reach, J. D. Smith, L. Rudnick, T. DeLaney, J. A. Ennis, H. Gomez, and A. Tappe. Freshly Formed Dust in the Cassiopeia A Supernova

Remnant as Revealed by the Spitzer Space Telescope. *ApJ*, 673:271–282, January 2008. doi: 10.1086/523835.

M. W. Richmond, R. R. Treffers, A. V. Filippenko, Y. Paik, B. Leibundgut, E. Schulman, and C. V. Cox. UBVRI photometry of SN 1993J in M81: The first 120 days. *AJ*, 107:1022–1040, March 1994. doi: 10.1086/116915.

G. H. Rieke and M. J. Lebofsky. The interstellar extinction law from 1 to 13 microns. *ApJ*, 288:618–621, January 1985. doi: 10.1086/162827.

G. H. Rieke, E. T. Young, C. W. Engelbracht, D. M. Kelly, F. J. Low, E. E. Haller, J. W. Beeman, K. D. Gordon, J. A. Stansberry, K. A. Misselt, J. Cadien, J. E. Morrison, G. Rivlis, W. B. Latter, A. Noriega-Crespo, D. L. Padgett, K. R. Stapelfeldt, D. C. Hines, E. Egami, J. Muzerolle, A. Alonso-Herrero, M. Blaylock, H. Dole, J. L. Hinz, E. Le Floc'h, C. Papovich, P. G. Pérez-González, P. S. Smith, K. Y. L. Su, L. Bennett, D. T. Frayer, D. Henderson, N. Lu, F. Masci, M. Pesenson, L. Rebull, J. Rho, J. Keene, S. Stolovy, S. Wachter, W. Wheaton, M. W. Werner, and P. L. Richards. The Multiband Imaging Photometer for Spitzer (MIPS). *ApJS*, 154:25–29, September 2004. doi: 10.1086/422717.

R. Sankrit, W. P. Blair, T. Delaney, L. Rudnick, I. M. Harrus, and J. A. Ennis. HST/ACS imaging of a Balmer-dominated shock in Keplers supernova remnant. *Advances in Space Research*, 35:1027–1030, 2005. doi: 10.1016/j.asr.2004.11.018.

B. Sibthorpe, P. A. R. Ade, J. J. Bock, E. L. Chapin, M. J. Devlin, S. Dicker, M. Griffin, J. O. Gundersen, M. Halpern, P. C. Hargrave, D. H. Hughes, W.-S. Jeong, H. Kaneda, J. Klein, B.-C. Koo, H.-G. Lee, G. Marsden, P. G. Martin, P. Mauskopf, D.-S. Moon, C. B. Netterfield, L. Olmi, E. Pascale, G. Patanchon, M. Rex, A. Roy, D. Scott, C. Semisch, M. D. P. Truch, C. Tucker, G. S. Tucker, M. P. Viero, and D. V. Wiebe. AKARI and BLAST Observations of the Cassiopeia A Supernova Remnant and Surrounding Interstellar Medium. *ApJ*, 719:1553–1564, August 2010. doi: 10.1088/0004-637X/719/2/1553.

J. Stebbins, C. M. Huffer, and A. E. Whitford. The Mean Coefficient of Selective Absorption in the Galaxy. *ApJ*, 92:193, September 1940. doi: 10.1086/144211.

F. G. W. Struve. *Etudes d'Astronomie Stellaire : Sur la voie lactee et sur la distance des etoiles fixes*. 1847.

B. E. K. Sugerman. Observability of Scattered-Light Echoes around Variable Stars and Cataclysmic Events. *AJ*, 126:1939–1959, October 2003. doi: 10.1086/378358.

B. E. K. Sugerman. An Introduction to Scattered-Light Echoes. In R. L. M. Corradi and U. Munari, editors, *The Nature of V838 Mon and its Light Echo*, volume 363 of *Astronomical Society of the Pacific Conference Series*, page 121, April 2007.

B. E. K. Sugerman, A. P. S. Crotts, W. E. Kunkel, S. R. Heathcote, and S. S. Lawrence. The Three-dimensional Circumstellar Environment of SN 1987A. *ApJS*, 159:60–99, July 2005. doi: 10.1086/430408.

B. E. K. Sugerman, B. Ercolano, M. J. Barlow, A. G. G. M. Tielens, G. C. Clayton, A. A. Zijlstra, M. Meixner, A. Speck, T. M. Gledhill, N. Panagia, M. Cohen, K. D. Gordon, M. Meyer, J. Fabbri, J. E. Bowey, D. L. Welch, M. W. Regan, and R. C. Kennicutt. Massive-Star Supernovae as Major Dust Factories. *Science*, 313:196–200, July 2006. doi: 10.1126/science.1128131.

B. M. Swinyard, P. Ade, J.-P. Baluteau, H. Aussel, M. J. Barlow, G. J. Bendo, D. Benielli, J. Bock, D. Brisbin, A. Conley, L. Conversi, A. Dowell, D. Dowell, M. Ferlet, T. Fulton, J. Glenn, A. Glauser, D. Griffin, M. Griffin, S. Guest, P. Imhof, K. Isaak, S. Jones, K. King, S. Leeks, L. Levenson, T. L. Lim, N. Lu, G. Makiwa, D. Naylor, H. Nguyen, S. Oliver, P. Panuzzo, A. Papageorgiou, C. Pearson, M. Pohlen, E. Polehampton, D. Pouliquen, D. Rigopoulou, S. Ronayette, H. Roussel, A. Rykala, G. Savini, B. Schulz, A. Schwartz, D. Shupe, B. Sibthorpe, S. Sidher, A. J. Smith, L. Spencer, M. Trichas, H. Triou, I. Valtchanov, R. Wesson, A. Woodcraft, C. K. Xu, M. Zemcov, and L. Zhang. In-flight calibration of the Herschel-SPIRE instrument. *A&A*, 518:L4, July 2010. doi: 10.1051/0004-6361/201014605.

A. G. G. M. Tielens. *The Physics and Chemistry of the Interstellar Medium*. September 2005.

P. Todini and A. Ferrara. Dust formation in primordial Type II supernovae. *MNRAS*, 325:726–736, August 2001. doi: 10.1046/j.1365-8711.2001.04486.x.

N. Tominaga, T. Morokuma, S. I. Blinnikov, P. Baklanov, E. I. Sorokina, and K. Nomoto. Shock Breakout in Type II Plateau Supernovae: Prospects for High-Redshift Supernova Surveys. *ApJS*, 193:20, March 2011. doi: 10.1088/0067-0049/193/1/20.

R. J. Trumpler. Absorption of Light in the Galactic System. *PASP*, 42:214, August 1930. doi: 10.1086/124039.

R. J. Tuffs, C. C. Popescu, and H. J. Völk. Far-infrared mapping of Cassiopeia A with ISOPHOT. In A. Wilson, editor, *ESA Special Publication*, volume 577 of *ESA Special Publication*, pages 427–428, January 2005.

S. van den Bergh. Light ECHOS from Ancient Supernovae. *PASP*, 77:269, August 1965. doi: 10.1086/128214.

F. P. A. Vogt, M.-A. Besel, O. Krause, and C. P. Dullemond. Probing Interstellar Dust with Infrared Echoes from the Cas A Supernova. *ApJ*, 750:155, May 2012. doi: 10.1088/0004-637X/750/2/155.

P. A. Whitelock, R. M. Catchpole, J. W. Menzies, M. W. Feast, S. E. Woosley, D. Allen, F. van Wyk, F. Marang, C. D. Laney, H. Winkler, K. Sekiguchi, L. A. Balona, B. S. Carter, J. H. Spencer Jones, J. D. Laing, T. L. Evans, A. P. Fairall, D. A. H. Buckley, I. S. Glass, M. V. Penston, L. N. da Costa, S. A. Bell, C. Hellier, M. Shara, and A. F. J. Moffat. Spectroscopic and photometric observations of SN1987A. VI - Days 617 to 792. *MNRAS*, 240:7P–24P, September 1989.

D. C. B. Whittet, editor. *Dust in the galactic environment*, 2003.

R. Willingale, J. A. M. Bleeker, K. J. van der Heyden, J. S. Kaastra, and J. Vink. X-ray spectral imaging and Doppler mapping of Cassiopeia A. *A&A*, 381:1039–1048, January 2002. doi: 10.1051/0004-6361:20011614.

T. L. Wilson and W. Batrla. An alternate estimate of the mass of dust in Cassiopeia A. *A&A*, 430:561–566, February 2005. doi: 10.1051/0004-6361:20041220.

M. Wolf. Über die Nebel der Nova Persei (Ch. 1226). *Astronomische Nachrichten*, 157: 161, December 1901. doi: 10.1002/asna.19011570911.

E. L. Wright, P. R. M. Eisenhardt, A. K. Mainzer, M. E. Ressler, R. M. Cutri, T. Jarrett, J. D. Kirkpatrick, D. Padgett, R. S. McMillan, M. Skrutskie, S. A. Stanford, M. Cohen, R. G. Walker, J. C. Mather, D. Leisawitz, T. N. Gautier, III, I. McLean, D. Benford, C. J. Lonsdale, A. Blain, B. Mendez, W. R. Irace, V. Duval, F. Liu, D. Royer, I. Heinrichsen, J. Howard, M. Shannon, M. Kendall, A. L. Walsh, M. Larsen, J. G. Cardon, S. Schick, M. Schwalm, M. Abid, B. Fabinsky, L. Naes, and C.-W. Tsai. The Wide-field Infrared Survey Explorer (WISE): Mission Description and Initial On-orbit Performance. *AJ*, 140:1868, December 2010. doi: 10.1088/0004-6256/140/6/1868.

M. Wright, J. Dickel, B. Koralesky, and L. Rudnick. The Supernova Remnant Cassiopeia A at Millimeter Wavelengths. *ApJ*, 518:284–297, June 1999. doi: 10.1086/307270.

D. G. York, J. Adelman, J. E. Anderson, Jr., S. F. Anderson, J. Annis, N. A. Bahcall, J. A. Bakken, R. Barkhouser, S. Bastian, E. Berman, W. N. Boroski, S. Bracker, C. Briegel, J. W. Briggs, J. Brinkmann, R. Brunner, S. Burles, L. Carey, M. A. Carr, F. J. Castander, B. Chen, P. L. Colestock, A. J. Connolly, J. H. Crocker, I. Csabai, P. C. Czarapata, J. E. Davis, M. Doi, T. Dombeck, D. Eisenstein, N. Ellman, B. R. Elms, M. L. Evans, X. Fan, G. R. Federwitz, L. Fiscelli, S. Friedman, J. A. Frieman, M. Fukugita, B. Gillespie, J. E. Gunn, V. K. Gurbani, E. de Haas, M. Haldeman, F. H. Harris, J. Hayes, T. M. Heckman, G. S. Hennessy, R. B. Hindsley, S. Holm, D. J. Holmgren, C.-h. Huang, C. Hull, D. Husby, S.-I. Ichikawa, T. Ichikawa, Ž. Ivezić, S. Kent, R. S. J. Kim, E. Kinney, M. Klaene, A. N. Kleinman, S. Kleinman, G. R. Knapp, J. Korienek, R. G. Kron, P. Z. Kunszt, D. Q. Lamb, B. Lee, R. F. Leger, S. Limmongkol, C. Lindenmeyer, D. C. Long, C. Loomis, J. Loveday, R. Lucinio, R. H. Lupton, B. MacKinnon, E. J. Mannery, P. M. Mantsch, B. Margon, P. McGehee, T. A. McKay, A. Meiksin, A. Merelli, D. G. Monet, J. A. Munn, V. K. Narayanan, T. Nash, E. Neilsen, R. Neswold, H. J. Newberg, R. C. Nichol, T. Nicinski, M. Nonino, N. Okada, S. Okamura, J. P. Ostriker, R. Owen, A. G. Pauls, J. Peoples, R. L. Peterson, D. Petravick, J. R. Pier, A. Pope, R. Pordes, A. Prosapio, R. Rechenmacher, T. R. Quinn, G. T. Richards, M. W. Richmond, C. H. Rivetta, C. M. Rockosi, K. Ruthmansdorfer, D. Sandford, D. J. Schlegel, D. P. Schneider, M. Sekiguchi, G. Sergey, K. Shimasaku, W. A. Siegmund, S. Smee, J. A. Smith, S. Snedden, R. Stone, C. Stoughton, M. A. Strauss, C. Stubbs, M. SubbaRao, A. S. Szalay, I. Szapudi, G. P. Szokoly, A. R. Thakar, C. Tremonti, D. L. Tucker, A. Uomoto, D. Vanden Berk, M. S. Vogeley, P. Waddell, S.-i. Wang, M. Watanabe, D. H. Weinberg, B. Yanny, N. Yasuda, and SDSS Collaboration. The Sloan

Digital Sky Survey: Technical Summary. *AJ*, 120:1579–1587, September 2000. doi: 10.1086/301513.

V. Zubko, E. Dwek, and R. G. Arendt. Interstellar Dust Models Consistent with Extinction, Emission, and Abundance Constraints. *ApJS*, 152:211–249, June 2004. doi: 10.1086/382351.

F. Zwicky. Types of Novae. *Reviews of Modern Physics*, 12:66–85, January 1940. doi: 10.1103/RevModPhys.12.66.

Erklärung:

Ich erkläre hiermit, dass ich diese Dissertation selbst verfasst und mich dabei keiner anderen als der von mir ausdrücklich bezeichneten Quellen und Hilfen bedient habe.

Heidelberg, den ____________________ ____________________
Unterschrift